Hybrid AC-High Voltage DC Grid

Stability and Controls

by

Jicheng Yu

A Dissertation Presented in Partial Fulfillment
of the Requirements for the Degree
Doctor of Philosophy

Approved November 2017 by the
Graduate Supervisory Committee:

George Karady, Co-Chair
Jiangchao Qin, Co-Chair
Raja Ayyanar
Keith Holbert
Qin Lei

ARIZONA STATE UNIVERSITY

December 2017

ABSTRACT

The growth of energy demands in recent years has been increasing faster than the expansion of transmission facility construction. This tendency cooperating with the continuous investing on the renewable energy resources drives the research, development, and construction of HVDC projects to create a more reliable, affordable, and environmentally friendly power grid.

Constructing the hybrid AC-HVDC grid is a significant move in the development of the HVDC techniques; the form of dc system is evolving from the point-to-point stand-alone dc links to the embedded HVDC system and the multi-terminal HVDC (MTDC) system. The MTDC is a solution for the renewable energy interconnections, and the MTDC grids can improve the power system reliability, flexibility in economic dispatches, and converter/cable utilizing efficiencies.

The dissertation reviews the HVDC technologies, discusses the stability issues regarding the ac and HVDC connections, proposes a novel power oscillation control strategy to improve system stability, and develops a nonlinear voltage droop control strategy for the MTDC grid.

To verify the effectiveness the proposed power oscillation control strategy, a long distance paralleled AC-HVDC transmission test system is employed. Based on the PSCAD/EMTDC platform simulation results, the proposed power oscillation control strategy can improve the system dynamic performance and attenuate the power oscillations effectively.

To validate the nonlinear voltage droop control strategy, three droop controls schemes are designed according to the proposed nonlinear voltage droop control design

procedures. These control schemes are tested in a hybrid AC-MTDC system. The hybrid AC-MTDC system, which is first proposed in this dissertation, consists of two ac grids, two wind farms and a five-terminal HVDC grid connecting them. Simulation studies are performed in the PSCAD/EMTDC platform. According to the simulation results, all the three design schemes have their unique salient features.

TABLE OF CONTENTS

Page

CHAPTER Page

CHAPTER Page

LIST OF TABLES

Table Page

Table Page

LIST OF FIGURES

Figure Page

Figure Page

Figure Page

Figure Page

CHAPTER 1

INTRODUCTION AND OUTLINE

The demands of a more reliable, affordable, and environmentally friendly power grid drive the increasing research and construction of the High Voltage Direct Current (HVDC) projects. Compared to alternating current (ac) networks, the HVDC system is superior in many aspects, such as long-distance bulk-power transmissions, offshore intermittent energy integration, weak/asynchronous ac network connections, more flexible topologies, and stronger capabilities to stabilize bus voltage and to control power flow. Therefore, embedding the HVDC systems into the present power grid requires the development of the HVDC and MTDC technology.

The first HVDC system for commercial installations can be dated back to the 1950s, rated at the 20 MW and the 100kV dc link between the Sweden mainland and the island of Gotland [1]. This project, constructed by Uno Lamm of Allmanna Svenka Elektriska Aktiebolaget of Sweden (ASEA, later merged into present-day ABB), marked the beginning of the modern era of the HVDC transmission system [2].

The system took advantage of mercury arc valves, which was a significant breakthrough at the time, nonetheless, the mercury valve requires an additional circuit to turn off the valve. Converters built with mercury arc valves use line-commutated converters (LCC).

With the invention of high-voltage and bulk-power thyristor in the early 1970s, the thyristor valve based HVDC converter stations have gradually superseded the mercury-based stations. The thyristor valves significantly improve the system reliability with reduced maintenance and full controllability. As a result, the HVDC station technology is

developed rapidly during the decade and several thyristor valves based HVDC transmission systems were constructed in the 1970s and 1980s [3]. From 1977, new HVDC projects only have been using solid-state components, such as thyristors, as the primary operating valve. Similar to mercury arc valves, thyristors valves require connection to an external control ac circuit to turn the valves on and off. The HVDC system using thyristor valves is also known as LCC-HVDC. Hitherto, the thyristor valve based HVDC becomes a mature, well-developed technology.

The recent breakthroughs in semiconductors are leading revolutionary changes in HVDC technology. The creation of high voltage fully controllable switches, transistors, such as an insulated-gate bipolar transistor (IGBT), injection-enhanced gate transistor (IEGT), and integrated gate-commutated thyristor (IGCT) prompt the development of voltage-sourced converter (VSC) based HVDC transmission system, making smaller HVDC systems economical. The first VSC based HVDC station uses pulse width modulation (PWM) IGBT converters, which was constructed as the experimental project as Hellsjön–Grängesberg Sweden in 1997 [4]. Since then, the VSC based HVDC systems are capturing a significant proportion of the HVDC market [5]. The manufacturer ABB Group names this concept as HVDC Light, while Siemens calls a similar concept HVDC PLUS (Power Link Universal System) and Alstom calls their product based on this technology HVDC MaxSine.

VSC-HVDC systems can significantly reduce harmonics and thus eliminate the filtering equipment. By comparison, the ac harmonic filter equipment of typical LCC stations consumes almost half of the converter station floor space.

More importantly, VSC-HVDC systems use transistors as their operating valves, and

LCC-HVDC systems use thyristors. Transistors can control the current through them fully on and off, but the thyristors can only turn themselves on but cannot switch them off freely, such that, the VSCs can fully control the active power flow and reverse the power flow directions without reversing the voltage polarities. This ability technically enables VSC-HVDC systems to extend their number of terminals, such that HVDC systems will evolve from the point-to-point system to the multi-terminal HVDC (MTDC) system. VSC systems are expected to replace most of the existing LCC systems, including the ultra high voltage dc power transmission applications [6].

The MTDC system further extends the range of HVDC applications, providing the possibility of meshed interconnections between regional power systems and various intermittent renewable energy resources, which potentially enhance both ac and dc system reliabilities, improve the flexibility in economic dispatches, and improve the converter/cable utilizing efficiencies [7].

There are several VSC technologies. The facilities built before 2012 use PWM technology, which has been used for an effectively ultra-high-voltage motor drive. The present facilities, including HVDC PLUS and HVDC MaxSine, are based on a new converter called Modular Multi-Level Converter (MMC) [8].

MMC is an advanced VSC topology and becomes the most attractive converter topology in the high power, and medium/high power applications, including the VSC, based MTDC systems. Compared to the two-level and other multi-level converter topologies, the MMC is superior in the following aspects: 1) modularity and scalability to any voltage level; 2) reduced voltage and dv/dt requirements of switches and capacitors; 3) high energy efficiency; 4) enhanced power quality in filter-free applications; 5) salient

fault-tolerance capability; and 6) advanced dc fault-blocking ability [8]. Consequently, the MMC is becoming the primary topology for MTDC systems.

The rest of this article is organized as follows:

Chapter 2 reviews the constructions of the HVDC systems, introduces the embedded HVDC system and discusses some issues regarding the ac and HVDC networks.

Chapter 3 introduces the existing hybrid AC-HVDC projects.

Chapter 4 proposes the coordinate control strategy for the embedded HVDC system to damp interarea power oscillations.

Chapter 5 develops a nonlinear voltage droop control strategy for the MTDC grid.

Chapter 6 summarizes the contributions of this dissertation and proposes future works.

CHAPTER 2

HVDC SYSTEMS: STATE OF THE ART

The HVDC system using thyristor valves is known as LCC is a mature, well-developed technology and the LCC-HVDC system dominates the application of HVDC in long-distance bulk-power transmission. The recent breakthrough in semiconductors is leading revolutionary changes in HVDC technology. The development of VSC technically enables the HVDC system to apply additional control strategies and extend the number of HVDC terminals.

In this chapter, the basic concepts of LCC and VSC are briefly introduced. Three major VSC construction topologies are described, including two-level converter, three-level converter and modular multilevel converter (MMC). Then, the HVDC system configurations are briefly described and, the concept of an embedded HVDC system is introduced. Two technical performance issues regarding the ac and MTDC systems are described at the end of this chapter.

2.1 Line-Commutated Converter

The line-commutated converter (LCC) utilizes thyristor valves as the primary operating devices. The thyristor valves can continue the current according to the control signal, but these valves are only able to open the circuit when the currents are zeros. The core module of the LCC is the three-phase full-wave bridge circuit, which is known as Graetz Bridge [9]. Graetz Bridge as shown in Figure 1 is the primary configuration for the LCC-HVDC converter. The Graetz Bridge can be used for transmitting power in two directions, and the converter stations can work in either rectifier mode or inverter mode.

However, the LCC based HVDC stations have several known weaknesses. The LCC-

HVDC produces temporary overvoltage (TOV) and low order harmonic resonance, especially when the HVDC is connected with a weak ac network [10]. The lower resonance frequency is, the higher risk will be produced. The occurrence of commutation failure forces the LCC-HVDC link trip [11]. Therefore, the LCC station always requires additional reactive power, which is more than half of the active power as designed. The reactive power is usually installed as large capacitor filters, which are costly and occupy large construction areas.

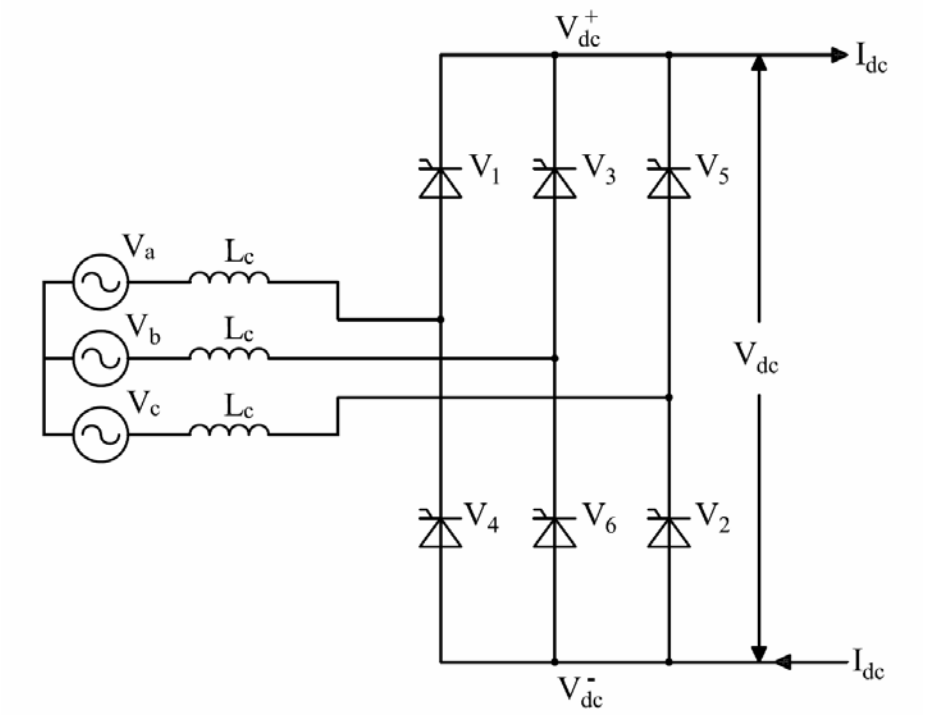

Figure 1. Graetz Bridge for LCC-HVDC system

The LCC-HVDC system is a mature technique and has become the dominant HVDCs in the application of long-distance bulk-power transmissions. As of 2012, the LCC-HVDC has been used on over 100 HVDC schemes, and several more are under construction or being planned [12] [13] [14].

2.2 Voltage-Sourced Converter

The voltage-sourced converter (VSC) based HVDC is the next-generation technology for the LCC-HVDC and would constitute the backbone of the future HVDC grids.

VSC utilizes transistors, such as IGBT, IEGT, and IGCT, as the operating valve. This kind of valve is a self-commutating switch, which can be turned on or off according to the control signal.

A VSC station can use pulse-width modulation (PWM) technology to produce its sinusoidal voltage waveform independent of the ac system. Therefore, the VSC stations can reduce the size of capacitor filters dramatically compared to the LCC stations.

More importantly, the VSC stations can control the active power and reverse the power flow direction without reversing the voltage polarities [15]. This ability technically enhances the system power flow controllability and enables the VSC-HVDC systems to extend their number of terminals.

Compared to the LCC-HVDC, VSC-HVDC has the following advantages [16] [17]:

1) Advanced power flow control capability, which allows a rapid switch of power flow direction by reverse the current direction but not the voltage polarity;
2) The capability of multi-terminal operations;
3) The avoidance of commutation failures due to disturbance in ac network;
4) Ability of independent control of active and reactive power flows to each terminal by the converters;
5) Possibilities of connecting VSC-HVDC system with a “weak” ac network;
6) No need for transformers to assist the commutation process of the converter’s entirely controlled semiconductors;

7) Faster dynamic response according to higher PWM than the fundamental switching frequency (phase-controlled) operation, which further results in reduced demand for filtering devices, and hence smaller filter size;
8) Capability of paralleled operation of dc network on regional ac grid; and
9) Reduced construction and commissioning time of an HVDC system.

Table 1 further summarizes the difference between the LCC-HVDC converter stations with the VSC-HVDC converter stations.

Numerous topologies have been proposed recently for a VSC station design: two-level converter, three-level converter and modular multi-level convert (MMC) [18].

TABLE 1. COMPARISON OF LCC-HVDC AND VSC-HVDC

Attribute	**LCC-HVDC**	**VSC-HVDC**
Converter technology	Thyristor valve, grid commutation	IGBT valve, self-commutation
Max converter rating at present	6400 MW, ±800kV	1200 MW, ±320kV
Relative size	4	1
Typical continuous operation time	36 months	24 months
Active power flow control	Continues ±0.1P_{rated} to ±P_{rated}; Takes time to change power flow directions.	Continuous 0 to ±P_{rated}
Reactive power demand	Reactive power equals 50% active power	No reactive power needed
Reactive power compensation & control	Discontinues control (switched shunt banks)	Continuous control (PWM build-in converter control)
Independent control of active & reactive power	No	Yes
Scheduled maintenance	Typically, < 1%	Typically, < 0.5%
Typical system losses	2.5 – 4.5%	4 – 6%
Multi-terminal configuration	Complex, limited to 3 terminals	Simple, no limitations

2.2.1 Two-level converter

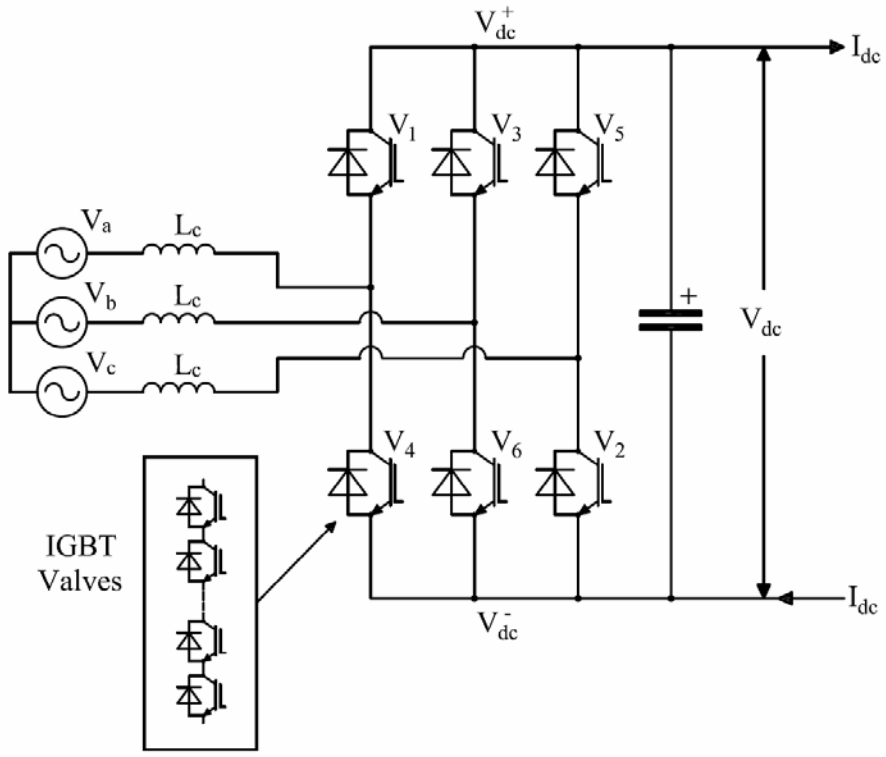

Figure 2. A two-level VSC topology

Figure 2 depicts a two-level grid connected VSC station topology. The bridge consists of six self-commutating valves, and each one includes a switching device and an anti-parallel free-wheeling diode. For a typical HVDC connection, two VSCs are interconnected with the dc side. In high voltage level applications, valves can be connected in series for a better operation.

2.2.2 Three-level converter

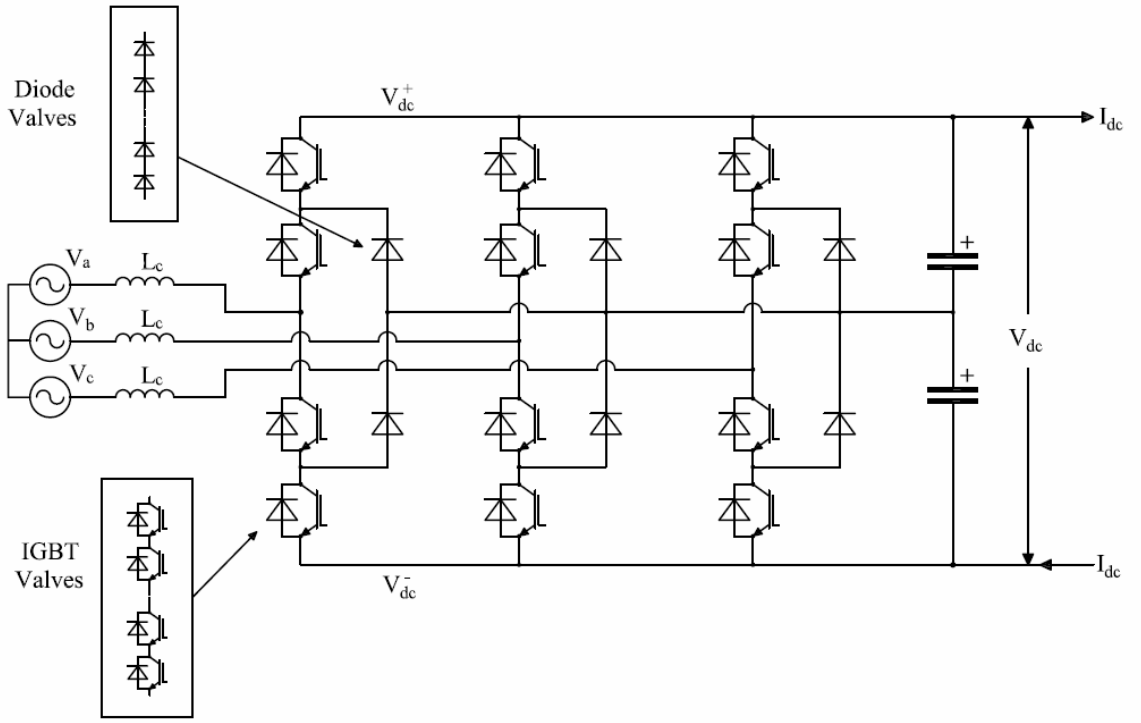

Figure 3. A three-level VSC topology

Figure 3 shows a three-level VSC station topology. The major components that changed from the two-level VSC topology are that two diode-clamped valves are installed in each phase. The two diode-clamped valve will clamp the switch voltage to half of the dc voltage. As a result, each phase of the VSC can turn to three different voltage levels. Consequently, the waveform produced by the three-level converter will be closer to the desired waveform when compared to the two-level converter. Moreover, the three-level topology will result in lower switching losses than the two-level topology [19].

2.2.3 Modular multilevel converter (MMC)

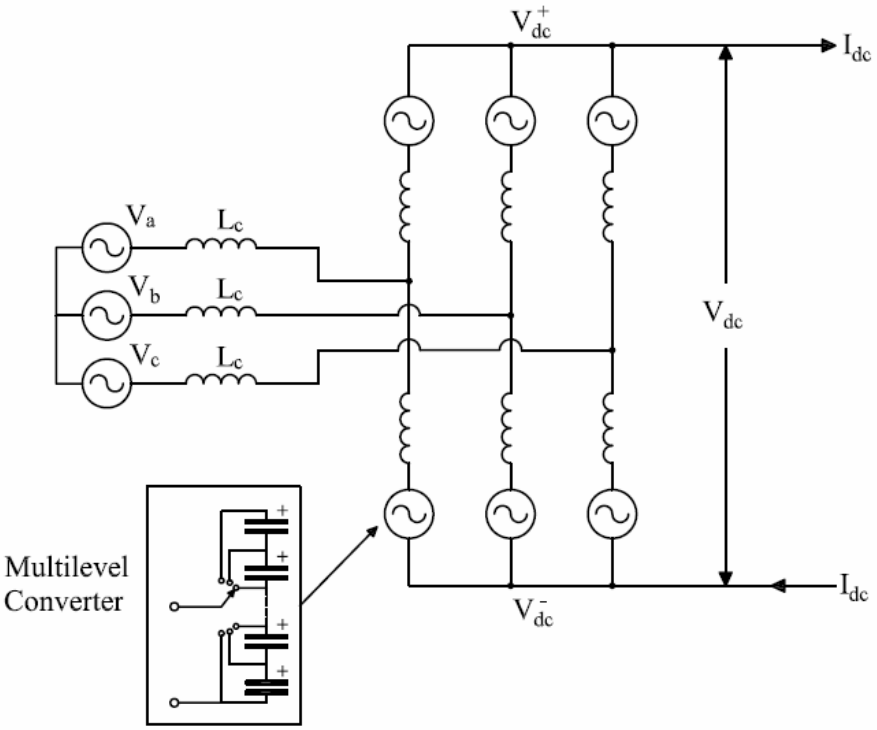

Figure 4. An MMC topology

Figure 4 illustrates an MMC topology. The MMC concept attracts significant interest for high-voltage converter applications [20]. The MMC has presented plenty of advantages.

In comparison with the two-level VSC and other multilevel converter topologies, the salient features of the MMC include: 1) its modularity and scalability to meet any voltage level requirements, 2) reduced voltage ratings and dv/dt stress of switches and capacitors, 3) high efficiency, 4) improved power quality for filter-free applications, 5) inherent fault-tolerance capability, and 6) fault-blocking capacity to improve fault interruption performance of the MMC-based HVDC systems. Therefore, the MMC has become the primary building block for VSC-HVDC systems. However, the MMC requires more switching components and more complicated controls than the two-level and three-level

converters [21].

Figure 5 depicts a schematic diagram of an MMC system. The MMC consists of two arms in each phase. Each arm has *N* series-connected, nominally identical, half-bridge submodules (SMs), and a series-connected inductor. The details of the operation of the MMC has been described in [22].

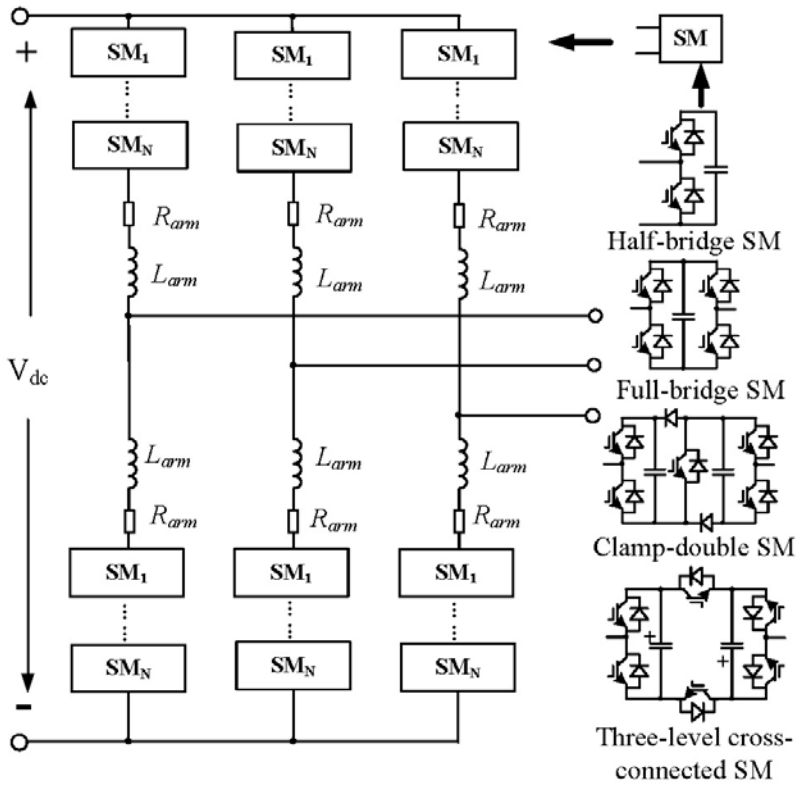

Figure 5 Schematic of an MMC with various submodules [21].

The MMC with HB SMs is the dominant topology for HVDC applications. However, in case of a dc-side short-circuit fault, the HB-MMC cannot block the fault currents feeding on ac grid. Various SMs have been investigated to improve the fault-blocking performance of the MMC, including the full-bridge, the unipolar-voltage full-bridge, the clamp-double, and the three-level/five-level cross-connected SMs [21] [23] [24].

2.3 Configurations of the HVDC System

The basic configurations of HVDC systems can be broadly categorized into the following aspects: back-to-back, monopolar, bipolar configuration, and multi-terminal configuration.

Figure 6 illustrates the three basic configurations. The choice of the configurations is alternative for each project according to the flexibility, stability, operation, and cost requirements [25].

Figure 6(a) depicts the back-to-back configuration. In this configuration, two converters are constructed at the same site. The converters are connected directly to each other, and the length of the direct current line will be kept as short as possible. The operation valves are connected in series. The dc voltage in the back-to-back configuration is selected as low as possible.

Figure 6(b) shows the monopolar configuration. In this configuration, the HVDC link connects to converter stations through a single conductor. The return conductor is connected to the ground, earth, or sea. Only a single conductor is performing at its operating voltage when the HVDC system operates as a monopolar configuration. In consideration of the reliability, the monopolar configuration is not allowed in the USA.

Figure 6(c) describes the bipolar configuration, which is the most popular configuration. In this configuration, a pair of conductors are employed, and each conductor will work at a high voltage but in opposite polarity. The bipolar scheme can be operated as two paralleled monopolar configuration HVDC, which allows the system to have continuous operations when one dc line is out. In North America, the bipolar configuration is obligatory for HVDC project designs for a higher safety operation.

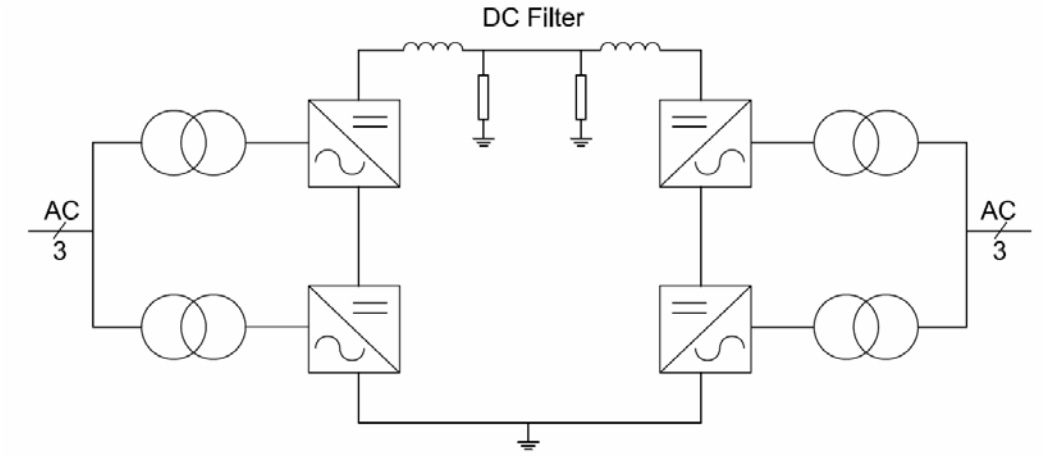

(a) Back-to-back configuration.

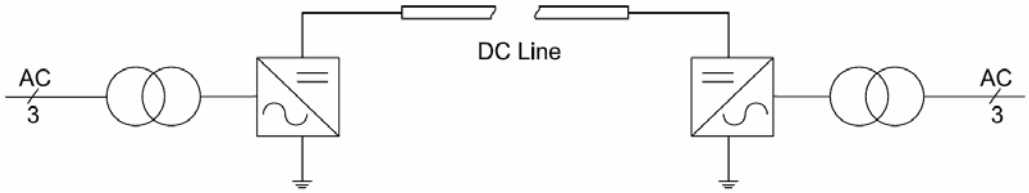

(b) Monopolar configuration.

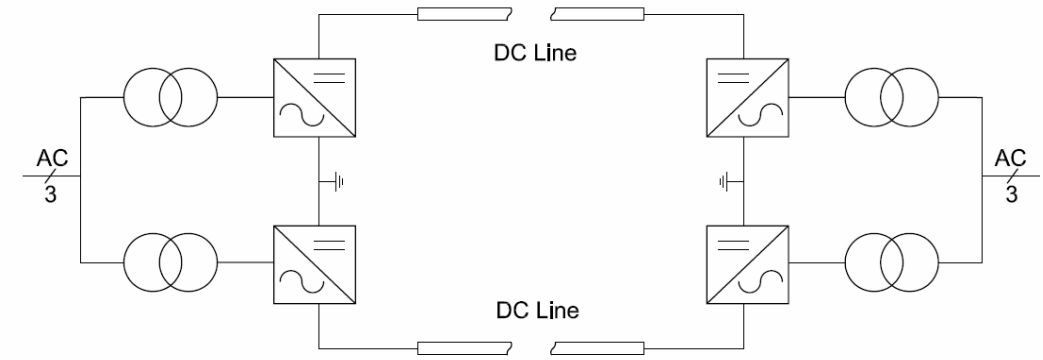

(c) Bipolar configuration.

Figure 6. The basic configuration topologies: (a) back-to-back (b) monopolar (c) bi-polar.

2.4 Embedded HVDC Systems

Based on how the HVDC system connects to the ac network, HVDC projects can be classified into three categories per their applications: HVDC interconnections, HVDC segmentations, and embedded HVDC systems [26].

The HVDC interconnections refer to the HVDC links that connect isolated ac systems. The objective of these projects is usually for long-distance power delivery [27], for example, the ±800kV Xiangjiaba-Shanghai project [28] and the ±500kV Inga-Shaba project [29].

The HVDC segmentations are utilized in decomposed large ac systems, where HVDC is responsible for energy transfers among segments These interties are commonly built in back-to-back configurations [26], such as the Oklaunion HVDC transmission link in Texas, USA, the Black Water project in New Mexico, USA, and the Higashi-Shimuzu project in Japan [30].

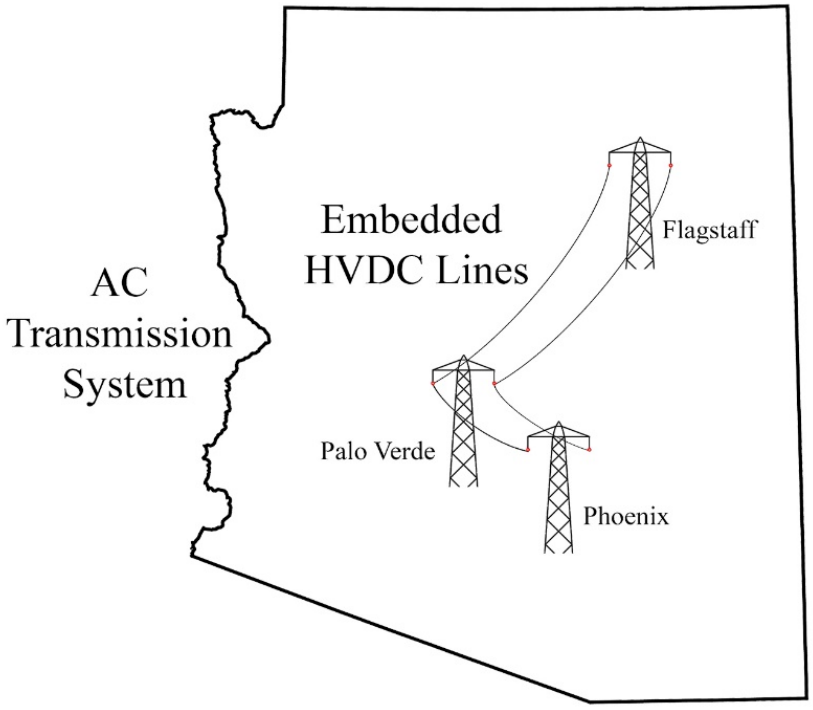

Figure 7 An embedded HVDC system example.

In an embedded HVDC system, at least two HVDC terminals are constructed within the same meshed ac system. Figure 7 describes a sample embedded HVDC system. As shown in the diagram, a three-terminal HVDC system is built within the ac transmission system. All the three dc buses are connected to the same meshed ac network. The system will not only transfer power through the HVDC, but will also offer additional control functions to improve system stability, for example, power oscillation damping, transient stability and fault recovery, and sub-synchronous damping enhancement [31] [32] [33] [34].

The International Council on Large Electric Systems, known as CIGRE, defines the embedded HVDC system as “an ac system consisting of HVDC links with at least two ends being physically connected within the synchronous ac network” [34].

2.5 Technical Performance Issues with AC and HVDC Systems.

2.5.1 Power oscillation damping

Electromechanical oscillations in the electrical system are generally categorized as intraplant mode oscillations, local plant mode oscillations, control mode oscillations, torsional mode oscillation between rotating plants and inter-area mode oscillations, [35].

The intraplant mode oscillations refer to the oscillations generated on the electric machines at same power generation site oscillating against each other at 2.0 to 3.0 Hz depending on the unit ratings and the reactance connecting them [36]. The intraplant mode oscillations manifest themselves within the generation plant compound. The intraplant mode oscillations typically will not affect the system outside of the generation facilities.

The local plant mode oscillations indicate the oscillation is swinging from one generator against the grid. The swing frequency usually located at 1.0 to 2.0 Hz. The damping and frequency vary with machine output and the impedance between the device terminal and the infinite bus voltage.

The control mode oscillations are associated with controllable equipment, such as generators, exciters, governors, HVDC converters, and static VAR compensators (SVCs). Transformer tap-changing controls can also interact complexly with nonlinear loads giving rise to voltage oscillations.

The torsional mode oscillations are related to turbine generator shaft systems, which have frequency range of 10 – 46 Hz. The torsional mode oscillations are excited when multi-stage turbine generators are connected to the grid system through a series compensated transmission line [37]. Torsional mode oscillations interact with the series connected capacitor at the natural frequency of the power grid. The resonance will appear

when the system natural frequency equals the difference of synchronous and torsional frequencies.

The interarea oscillation phenomenon is observed on a large scale of the grid. It happens when two coherent sets of generators swinging against each other at 1 Hz or less.

Low-frequency interarea power oscillations are a common phenomenon arising between groups of rotating power generators, commonly interconnected by weak and heavily loaded ac interties. Such oscillations can be excited by several reasons such as line-faults, switching of lines or a sudden change of generator output [35]. The typical oscillation frequency is approximately 0.3 Hz [36].

The interarea oscillation phenomenon involves many parts of the system with highly nonlinear dynamic behavior. The tie-line resistance dictates the damping characteristic of the inter-area mode.

Interarea oscillations are the primary reasons for many system separations and a few wide-scale blackouts [37]. The incidents with noticeable sequence are listed Table 2.

For effective damping of inter-area oscillations, the essential step is to determine or estimate the oscillation characteristics accurately from 1) linearized power system model; 2) waveforms obtained from time-domain simulations; 3) real-time signal measurements [38] [39]. However, low-frequency variations of power system states cannot be easily recognized due to the nonlinear, aperiodic, and stochastic behavior of power systems [40]. Moreover, power oscillation monitoring is a challenging task due to the differences in small-signal and large-signal oscillation characteristics and the excitation shortage of the oscillating modes during normal operation [41]. Therefore, analysis methods are challenging both in time and frequency domain, ranging from non-parametric or parametric

signal processing techniques to data-driven time-series models and statistical approaches. The most popular and up-to-date detection methods are provided below.

TABLE 2. INCIDENTS CONTRIBUTED BY INTERAREA OSCILLATIONS

Incidence power network	**Year(s) of Incident**
Detroit Edison (DE)-Ontario Hydro (OH)-Hydro Quebec (HQ)	1960s, 1985
Finland-Sweden-Norway-Denmark	1960s
Saskatchewan-Manitoba Hydro-Western Ontario	1966
Italy-Yugoslavia-Austria	1971-1974
Western Electric Coordinating Council (WECC)	1964, 1996
Mid-continent area power pool (MAPP)	1971, 1972
South East Australia	1975
Scotland-England	1978
Western Australia	1982, 1983
Taiwan	1985
Ghana-Ivory Coast	1985

The low-frequency inter-area power oscillation is a common phenomenon in the power system [9]. However, neither the damper windings of the synchronous machines nor the modern digital electro-hydro control systems without global signal measurement can effectively attenuate the inter-area oscillations [42]. Therefore, to attenuate the inter-area

power oscillation is essential for the power network and has been a challenge for a long time.

The VSC based embedded-HVDC system with additional control is expected to be a solution to attenuate the inter-area power oscillations. It is possible to modulate reference to the active power through the HVDC transmission system together with additional signals to maintain the system to stay in a healthy status.

2.5.2 Power flow sharing among multiple converters

a) Master-Slave Control

In the two terminal HVDC system, a typical control scheme will use one converter station to control the active power and the other station to control the dc link voltage. As a natural extension, in a multi-terminal dc network, a typical control scheme, master-slave control is to use only one converter to maintain the entire dc grid voltage while all other converters will be responsible for the active power set-point control for its local converter [43] [44] [45].

When the mismatch power is the same direction as the normal operation power, the dc voltage controlling converter will be easily overloaded. When mismatch power is opposing the direction as the normal operation power, the dc voltage controlling converter might have the power flow direction reversed. This will affect the surrounding ac systems.

The steady state operation characteristics of the MTDC grid can be represented on a two-dimensional plan applying the control variables in different axes. Using a five-terminal MTDC system, for example, the converter station #1 maintains the dc voltage and the converter #2, #3, #4 and #5 regulate the active power.

Figure 8 depicts a steady state operation of a five-terminal MTDC grid in a master-slave control scheme. The upper subplot shows the operating point under normal condition; the lower subplot shows the operating point following the outage of the converter station #5.

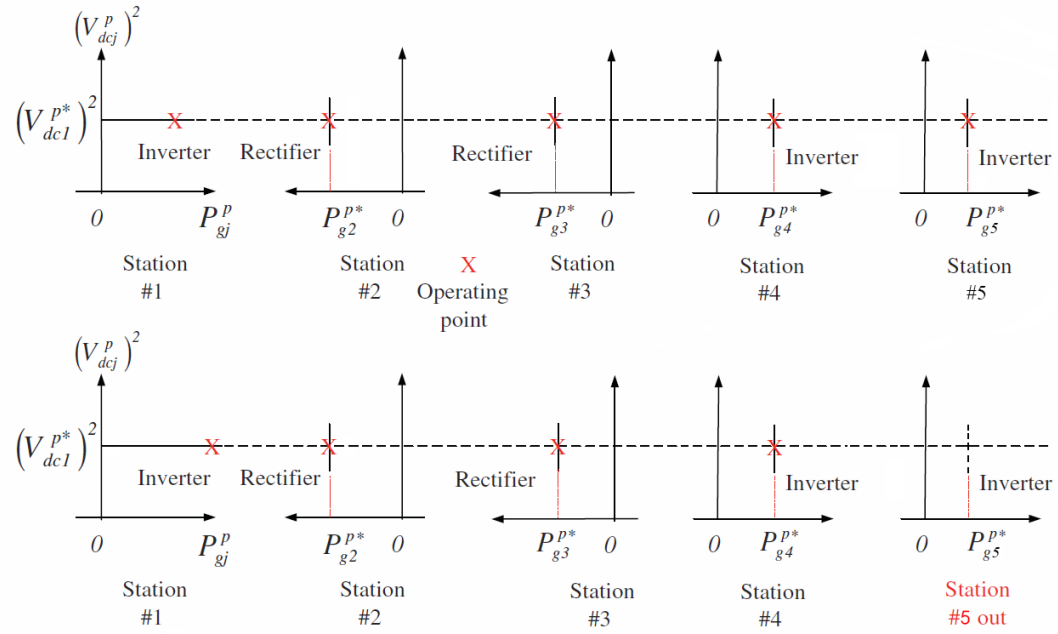

Figure 8 Steady-state operating characteristics of the positive pole converters in the five-terminal MTDC grid.

When the converter station #5 is lost, the operation point will be moved to as shown in the lower subplot that Station #1 will receive all the mismatch power. On this specific case, Station #1 will manage the sum of the power of Station #1 and #5 in the upper plot in Figure 8 the new power would easily exceed the original station power limit.

Besides, when the master control converter fails, the dc voltage control will be lost. Consequently, the dc grid will disassemble immediately.

b) Voltage Margin Control

Voltage margin control, regarded as an improved version of the master-slave control, can shift the voltage regulating task among the converters when power limitation exceeded.

Figure 9 shows the control characteristics of a point-to-point dc system with voltage margin control for the positive pole converter stations.

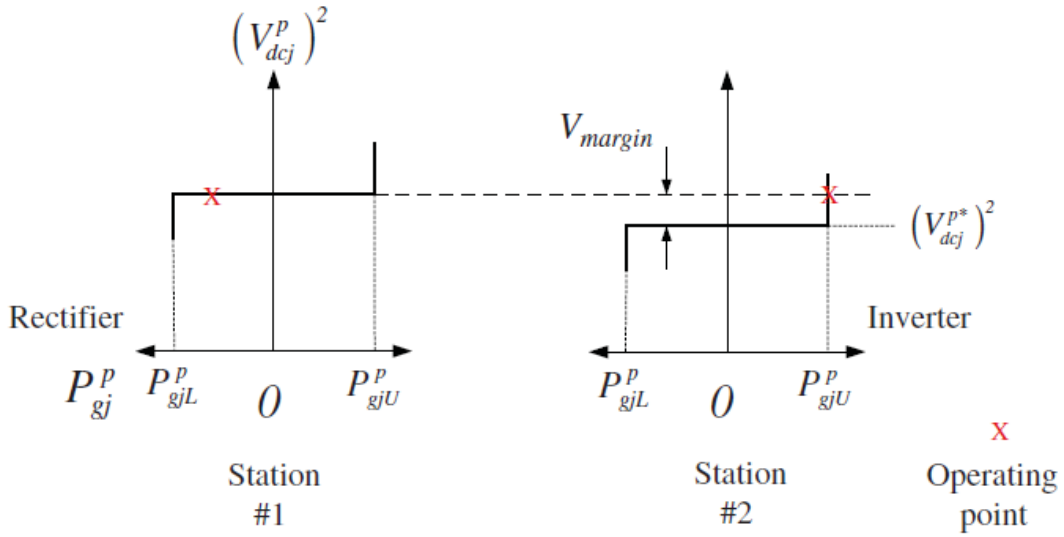

Figure 9 Control characteristics of a point-to-point DC system with voltage margin control for the positive pole converter stations.

For the inverter station operating under dc voltage control, if the power increases beyond P_{gjU}^{p} the dc voltage rises, and the rectifier will take over the voltage control.

However, this method still has only one converter to regulate the dc voltage and suffer from the dc oscillations produced when shifting the master converter. Besides, the dynamic response to this control is slow because the communication between the converters takes time [46].

c) Voltage Droop Control

In an MTDC grid, it is desirable that following an outage of one or more converters, all the remaining converters should share the resulting power imbalance in certain appropriate proportion. As a result, all converter stations should control the dc voltage rather than trying to follow their respective active power references strictly. Nonetheless, setting values of dc link voltage references at all the converter stations could be conflicting

unless they are modified properly depending on the reference and actual values of the active power and dc link voltage [47] [48]

In the voltage droop control, the converter regulating the converters will share the power based on the slope of their voltage droop characteristics [49]. The voltage droop control has a fast-dynamic response because the control does not require a communication among the dc terminals. The dc voltage droop control acts in a similar role as the frequency-droop control in the ac system. In a voltage droop control, at least two converters in the MTDC system will be responsible for regulating the dc voltage and balancing the power simultaneously.

However, all the existing voltage droop control strategies only employ a linear relationship between the voltage and power. Different converters in an MTDC system may have different droop control design requirements. At different operating points, they MTDC system may have different dynamic and operating system requirements.

It is possible to generate a nonlinear droop control relationship to fulfill the above-mentioned issues.

CHAPTER 3

HYBRID AC-HVDC PROJECTS

In the most recent decade, a few hybrid AC-HVDC projects are constructed and commissioned. This chapter introduces seven commissioned hybrid AC-HVDC projects in the world. The major characteristics of each project are described.

3.1 Caprivi Link (Namibia)

Southern African Power Pool (SAPP) is a project that an ac interconnected power system with three HVDCs.

The electricity generation in South Africa consists mainly of thermal power stations, while the Eastern Corridor (Zimbabwe and Zambia) contains mostly Hydro Power Systems. The Western Corridor (Namibia) has only minimal hydro and thermal generation. The Namibia project was completed in June 2010. The Cahora Bassa HVDC scheme has a parallel ac network path between the converter stations.

Figure 10 depicts the geographic location of terminal points for the Caprivi link interconnector. The Caprivi monopolar scheme (rated at 300 MW) connects the electricity networks of Namibia and Zambia. The Zambezi substation (330 kV) near Katima Mulilo in the Caprivi Strip connects to Gerus 400 kV substation near Otjiwarongo in the center of Namibia with 950 km of overhead line operating at 350 kV dc [50]. The scheme utilizes VSC station and is the first project to use VSC technology with the overhead lines.

The VSC-HVDC stations have proven to improve stability and assist with the prevention of blackouts when two fragile ac networks are interconnected and run in parallel with ac systems such as the SAPP in this project. It provides robust voltage support when the inherent voltage drops. It also caters to the diverse network conditions that are planned

eventual providing n-1 network security when the bi-pole is implemented.

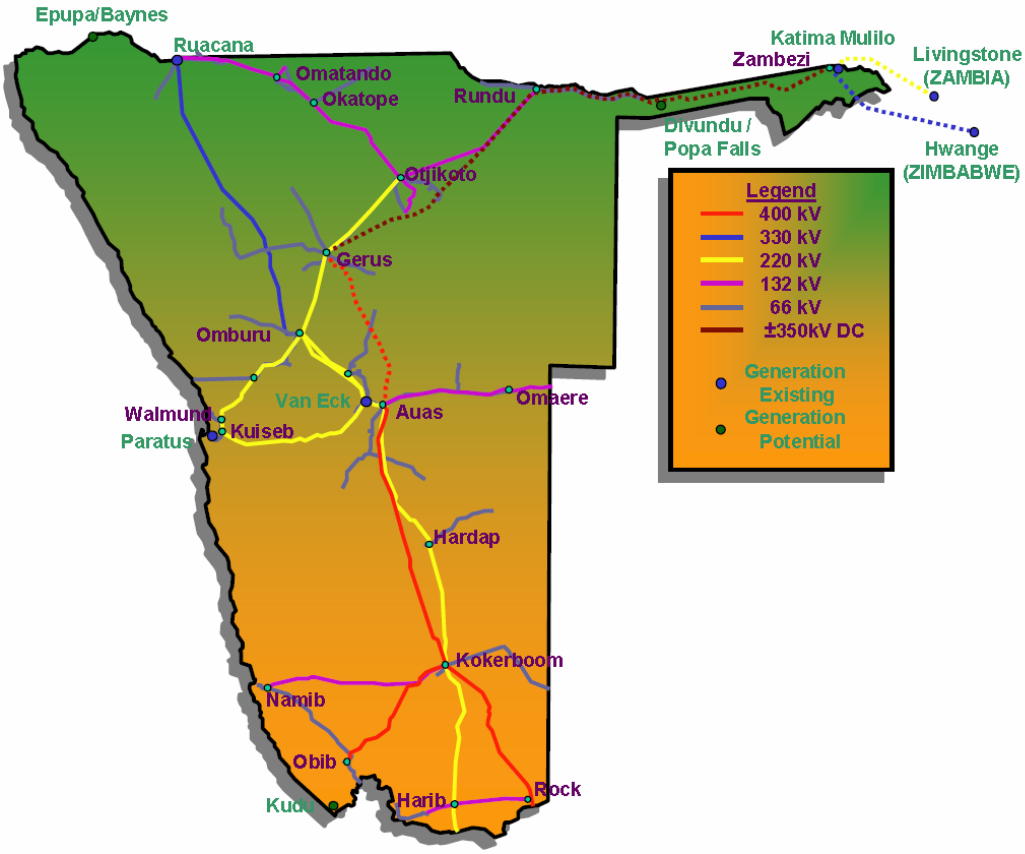

Figure 10. Geographic location of terminal points for the Caprivi Link Interconnector.

(A direct copy from [50].)

3.2 Kii Channel HVDC Project (Japan)

The electricity transmission system in Japan is the particular system because Japan is the only country that was divided into two regions with different primary rated operation frequencies. Eastern Japan, including Tokyo, Kawasaki, Sapporo, Yokohama, and Sendai, operates at 50 Hz; Western Japan, includes Okinawa, Osaka, Kyoto, Kobe, Nagoya, and Hiroshima, runs at 60 Hz. The frequency difference partitions Japan's national grid. Consequently, the power can only be transmitted between the two parts of the networks using frequency converters, or HVDC transmission lines [51].

The first HVDC project in Japan constructed in embedded HVDC topology is the Hokkaido-Honshu HVDC link connecting between Hokkaido island and Honshu island. Kii channel is the second HVDC project in Japan. The channel connected Honshu island and Shikoku island and was first commissioned in 2000 to transmit power generated by coal-fired thermal power plants which consisted of two units of 1050 MW and the other unit of 700 MW located in Shikoku island [52].

Figure 11 shows the configuration of Kii Channel HVDC which is a bipolar configuration. The Kii HVDC project utilizes LCC technology to transfer large power with a combination of the overhead transmission line and submarine cable. The project uses various new techniques in both main circuit and the control system. The first stage is rated at 1400 MW, 250 kV and 2800 A and the second stage is rated at 2800 MW, 500 kV and 2800 A. The Kii Channel HVDC project was planned, constructed and co-owned by Kansai Electric Power company (KANSAI), Shikoku Electric Power Company (SHIKOKU) and Electric Power Company [53]

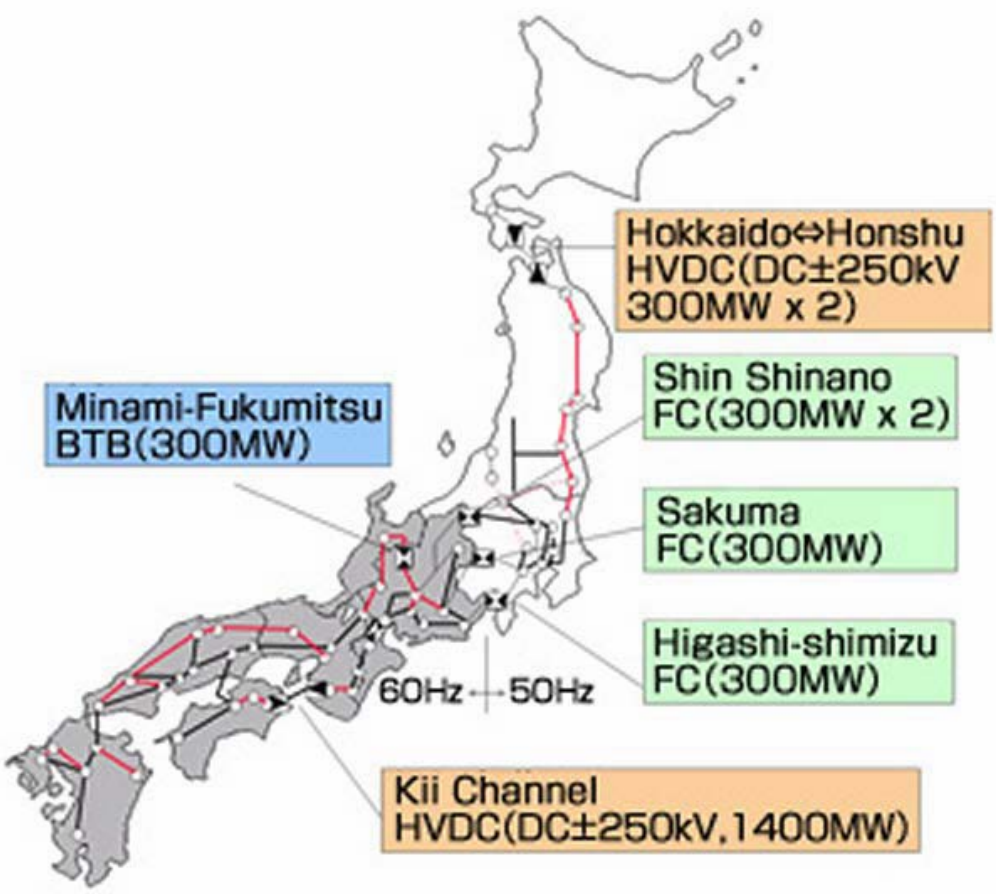

Figure 11. HVDC transmission system in Japan.

(A direct copy from [51].)

3.3 Kingsnorth HVDC Link (England)

The Kingsnorth HVDC transmission project was commissioned in 1972. The project was the first HVDC scheme constructed as embedded HVDC system within an existing ac network [54]. The project was also the first HVDC system to use entirely land cables for power transmission. Mercury arc valves were applied at the first stage using ARBJ/6 type and were the largest mercury arc valves both in voltage and current ratings) ever built by any manufacturer. The project was upgraded with air-cooled thyristor valves in 1981 and

was decommissioned in 1987.

The National Grid in the United Kingdom first originated in the 1930s with a transmission voltage of 132 kV to interconnect the hitherto independent regional electricity generating and supply companies. The 132 kV transmission lines were lightly loaded when the line was first commissioned because most electricity continued to be generated close to where it was being utilized. In the 1950s a higher transmission voltage of 275 kV was introduced to reinforce the gird, and in the early 1960s, the first parts of the 400-kV transmission network had been built. Since then, each of the three largest cities, London, Birmingham, and Manchester, was served by a 400-kV outer ring, with radial connections inwards to an inner ring at a lower voltage.

Accordingly, the Central Electricity Generating Board (CEGB), the then-nationalized electricity utility for England and Wales, placed an order in 1966 for a 640 MW underground cable HVDC link from the Kingsnorth power station to two sites in South and West London. The objective was to feed the receiving stations and support the nearby ac system without increasing the short-circuit level.

The Kingsnorth station was constructed in a bipolar configuration. Each pole is formed at a power transmission rating of 320 MW at 266 kV dc and consists of two series connected 6-pulse groups of mercury-arc valves. Both the Bedlington and Willesden stations were monopolar configuration rated at 320 MW and consisted of two 6-pulse groups. A neutral dc cable links the Willesden and Bedlington stations with changeover switchgear installed. This construction permitted power to be transmitted between these two stations in the event of the cable from Bedlington to Kingsnorth being out of service. The Kingsnorth link had a total length of 82 kilometers in an underground cable.

3.4 Fenno-Skan HVDC Link (Finland-Sweden)

In addition to synchronous ac tie-lines to Sweden and Norway, Finland is connected with neighboring transmission networks using five HVDC systems. Four of those, given in Table 3, can be considered to be a part of the Finnish transmission networks whereas Vyborg B2B LCC-HVDC, which connects the asynchronous Nordic and Russian transmission systems, is located in Russia nearby city, Vyborg.

TABLE 3. HVDC SYSTEMS IN FINLAND

Name	Embedded HVDC	In operation since	Length (km) and Type
Fenno - Skan	Yes	1989	200 (Submarine)
EstLink	No	2003	130 (Submarine)
Fenno - Skan2	Yes	2011	200 (Submarine) + 70 (OHL)
EstLink2	No	2014	130 (Submarine) + 30 (OHL) + 10 (Land Cable)

As illustrated in Figure 12, the Fenno-Skan HVDC connections are in parallel with ac transmission path with a length of order 2000 km, and they connect the South Finland and South Scandinavia.

Due to length of the transmission path between the South Finland, that is both the main area of generation and consumption, and South Scandinavia, ac power transfer from and to South Finland is actually limited by stability phenomena; under South to North power flow

conditions by damping of 0.3 Hz inter-area oscillations and under North to South conditions voltage stability [55].

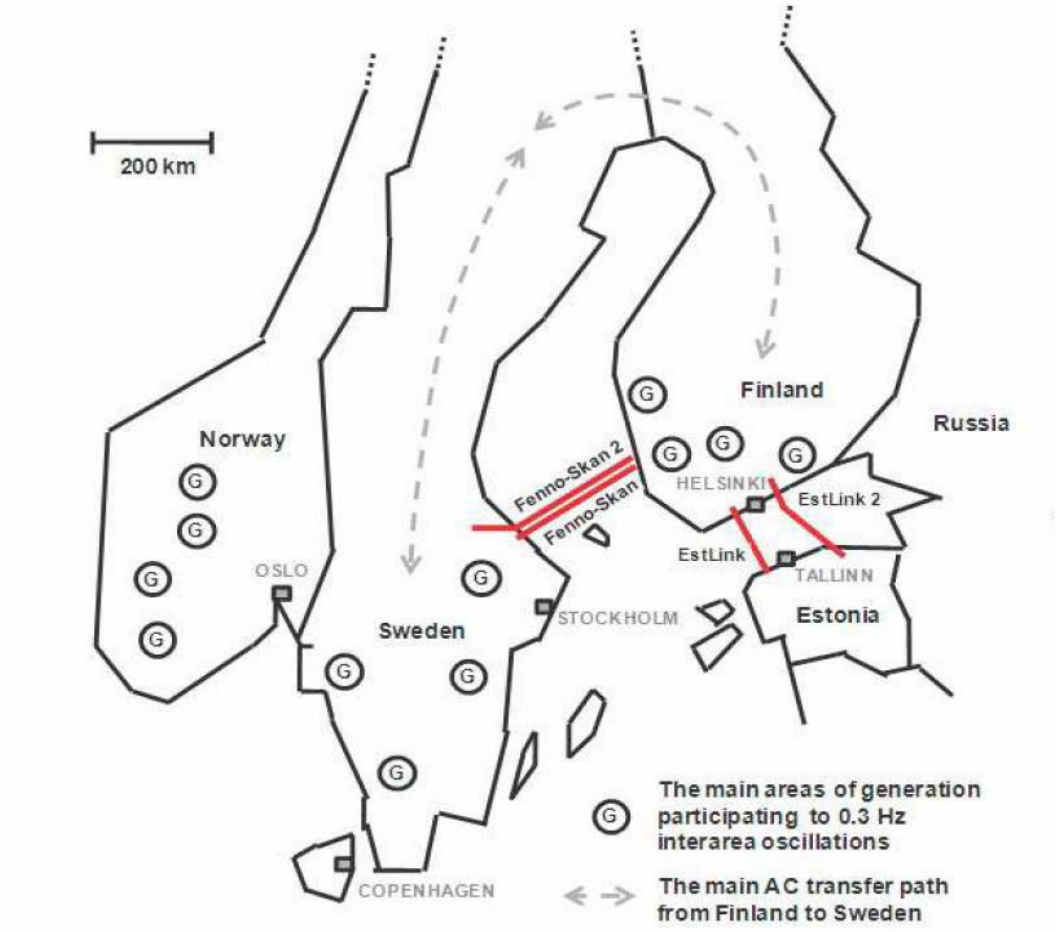

Figure 12. HVDC connections in Finland and their contribution in ac system.

(A direct copy from [55].)

Concerning interactions between the ac system and HVDC system, two additional concepts have been applied in operation of Fenno-Skan and will be applied in operation of Fenno-Skan2; the optimization of North to South power transfers and the sub-synchronous damping controls.

3.5 Guizhou – Guangdong I and II (China)

The Guizhou-Guangzhou (GG) I and II projects are constructed for long-distance bulk power transmission. The two HVDC projects are designed to operate at ± 500 kV, and the capacity of each project is 3000 MW, respectively. Both projects deliver power from Guizhou province located in the south-west China to Guangdong province located in south-mid China. The length of transmission lines is 980 km in GG I which was first commissioned in 2004 and 1200 km in GG II which was first commissioned in 2007 [56].

The project was constructed in a bipolar configuration. Each pole comprises twelve pulse converter bridges suspended from the ceiling. The thyristor valves are water-cooled and direct-light-triggered. Most of the dc devices are provided with composite housings to improve the performance of operation under different environmental conditions.

3.6 Nan'ao MTDC (China)

The Nan'ao MTDC project is the first MTDC system employing VSC technology [57]. The Nan'ao project aims to transfer the distributed offshore wind farms to the mainland by the MTDC system. The project was first commissioned in 2013.

Figure 13 shows the configurations of the Nan'ao MTDC project. The dc grid is rated at 160 kV. The Nan'ao project has two stages. During the first stage, three dc terminals are connected.

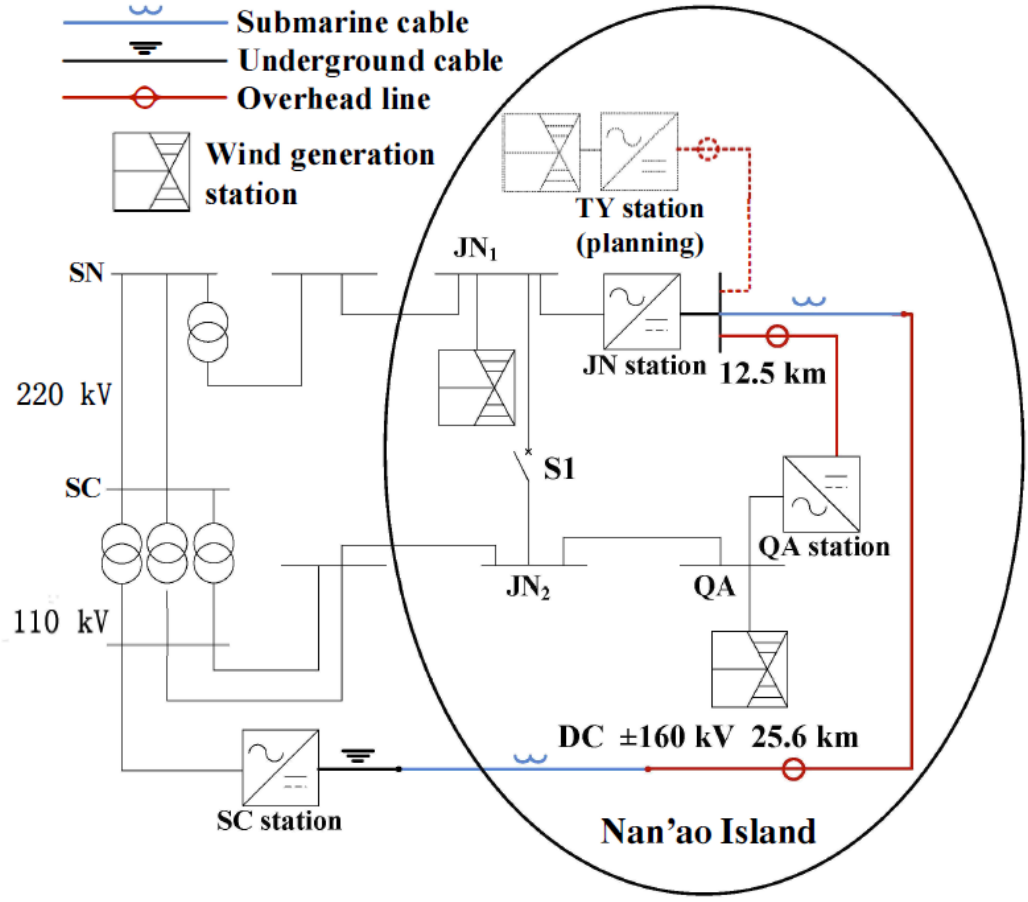

Figure 13. The configuration of Nao'ao project.

(A direct copy from [57].)

The terminals are Jinniu (JN) station rated at 100 MVA, which is located at Nan'ao Island; Qing'ao (QA) station rated at 50 MVA, which is located at Nan'ao Island; and Sucheng (SC) station rated at 200 MVA, which is located in mainland China. In the second stage, the Tayu (TY) offshore wind farm station is connected to the dc grid as the fourth terminal.

TABLE 4. KEY PARAMETERS OF NAO'AO MTDC STATIONS [65]

Parameters	SC Station	JN Station	QA Station
Transformer connection	Yn/D11	Yn/D11	Yn/D11
Rated power (MVA)	240	120	63
Primary voltage (kV)	110	110	110
Secondary voltage (kV)	166	166	166
Primary impedance (p.u.) [R,L]	[0.0025, 0.06]	[0.0025, 0.06]	[0.0025, 0.05]
Secondary impedance (p.u.) [R,L]	[0.0025, 0.06]	[0.0025, 0.06]	[0.0025, 0.05]
Grounding resistance (kΩ)	5	5	5
MMC capacity (MVA)	200	100	50
Number of SMs in an arm	147	220	220
Capacitor of a SM (mF)	5	2.5	1.4
Number of redundant SMs	14	20	20
Rated SM voltage (kV)	2.4	1.6	1.6

The conductors between JN and SC converter stations are hybrid of overhead lines and undersea cables, with a total length of 28.2 kilometers. The QA and JN converter stations are connected by 12.5-km overhead lines. The Nan'ao MTDC system is a hybrid ac-MTDC system, the primary parameters of the project are listed in Table 4.

3.7 Zhoushan MTDC (China)

The Zhoushan Island is located on the Hongzhou Bay, south-east coast of China. Zhoushan MTDC project consists of five terminals HVDC. The grid connection of the Zhoushan Project is shown in Figure 14.

The rated dc grid voltage is 200 kV. Five VSC-HVDC stations are constructed on individual islands: Zhoushan (S1), Daishan (S2), Qushan (S3), Yangshan (S4) and Sijiao (S5). The rated powers are 400 MW in S1, 300 MW in S2, 100 MW in S3, S4 and S5 [58]. Beside the VSC-HVDC station, there is an ac substation at each island to provide power to both dc grid and local load.

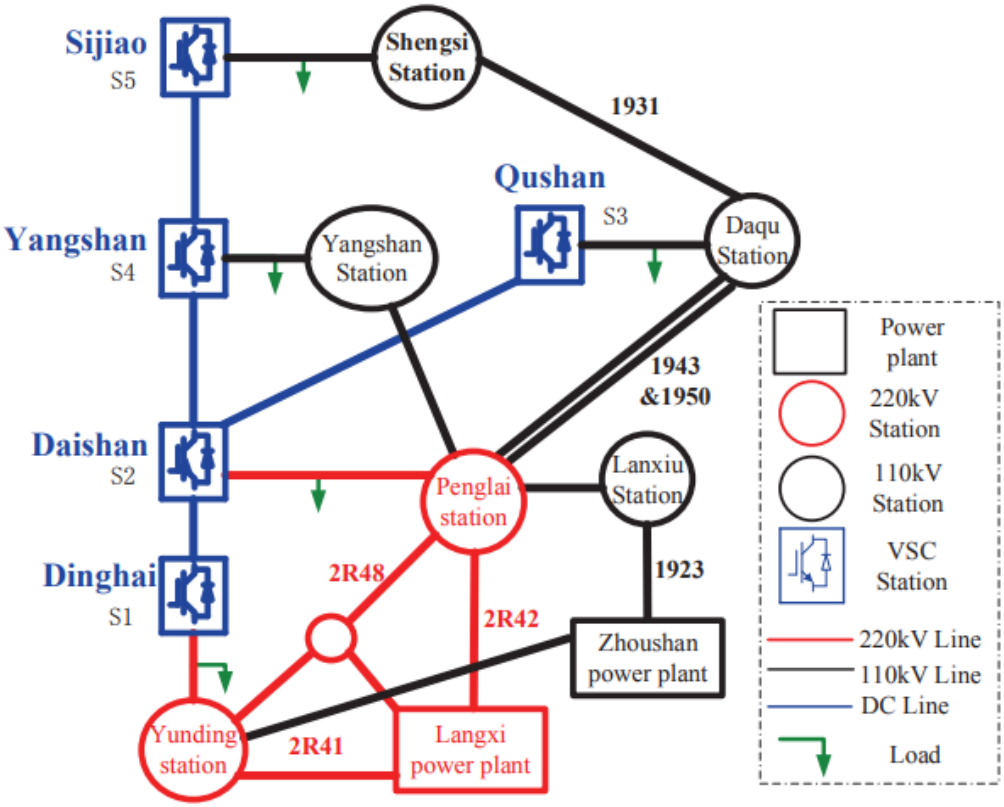

Figure 14. The configuration of Zhoushan project.

(A direct copy from [59].)

CHAPTER 4

POWER OSCILLATION CONTROL STRATEGY FOR EMBEDDED HVDC SYSTEMS

The low-frequency interarea power oscillation is a common phenomenon in the power system. However, neither the damper windings of the synchronous machines nor the modern digital electro-hydro control systems without global signal measurement can effectively attenuate the interarea oscillations, Therefore, to attenuate the interarea power oscillation is essential for the power network and has been challenged for a long time. The VSC based embedded-HVDC system with additional control is expected to be a solution to attenuate the inter-area power oscillations. It is possible to modulate reference to the active power through the HVDC transmission system together with additional signals to maintain the system to stay in a healthy status.

The conventional control for the VSC-HVDC system is briefly introduced in chapter 4.1, and the oscillation detection methods are summarized in chapter 4.2.

A novel power oscillation control scheme is proposed in chapter 4.3, and an updated version of the control: coordinate power oscillation control scheme is proposed in chapter 4.4.

The proposed control scheme is verified in chapter 4.5 by using a parallel AC-HVDC system. The simulation is performed on the PSCAD/EMTDC platform.

4.1 Conventional Control in the Stationary Frame

Each VSC-HVDC station is connected to the ac system via an equivalent impedance and a transformer. The impedance represents the reactor connecting between the VSC converter station and the ac network. A capacitor bank is connected to the dc side of each VSC station. One VSC station acts as an inverter, and the other VSC station works as the rectifier according to the active-power flow direction. Each VSC station has two control loops: one loop is used for reactive power control so that the ac voltage will be controlled; the other loop is used for active power control.

Compared to the LCC-HVDC system, the VSC-HVDC allows fully independent control of active and reactive power within the operation range of the station design. Each station can control its reactive power independent of the other station. To ensure the active power balance in the dc transmission system, the real power entering the HVDC must equal to the real power leaving it plus the losses along the dc transmission lines or cables. Therefore, to ensure this active power balance, a favorite control strategy design is to use one VSC station to control the dc voltage and the other VSC station is designated to control the active power flow through it.

The control strategy of the VSC-HVDC link in Figure 15 depicts the conventional d-q vector control cooperating with the proposed power oscillation control loop. The conventional control method is a nested-loop d-q vector control based on the linear PI control technology [60]. This conventional control method involves two control loops: one loop named outer loop, which controls the active power and ac voltage; the other loop called inner loop, which controls the d-q currents [61].

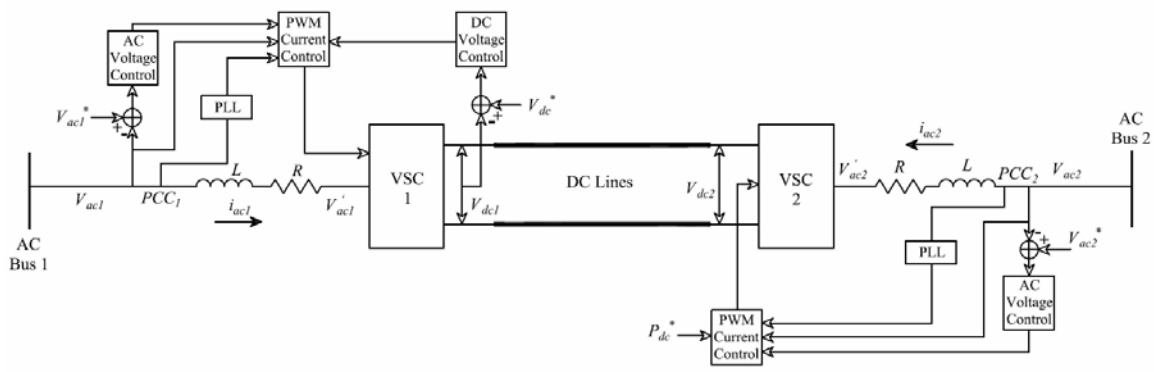

Figure 15. The configuration of a VSC-HVDC transmission system.

A transformation from the three-phase to the d-q phase is required for the conventional d-q vector control method. The three-phase ac voltages and currents are transformed into d-q phase via Park's transformation. Then, the outer control loop generates the d-q current references according to the control objectives. Finally, the inner current control loop regulates the d-q currents and generates the appropriate switching pulses for the rectifier and inverter [62]. Thus, the dc voltage of the rectifier and the ac power flowing out of the inverter can be controlled in the system depicted in Figure 15.

In embedded HVDC systems, the transmission between the two areas is the parallel operation of ac and HVDC. Except for the merit from HVDC alone, the HVDC transmission can also be possibly controlled to attenuate the power oscillation along the ac transmission lines. As depicted in Figure 15, both dc terminals are connected to the same ac system. The ac frequency difference between the two terminals should always remain within a small range to keep the system synchronized.

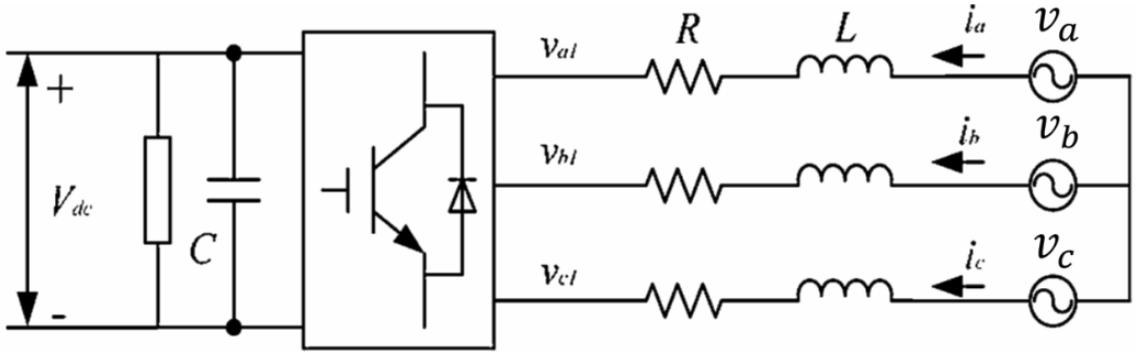

Figure 16. An equivalent System model of a VSC station.

Figure 16 depicts the equivalent system model of a VSC station connected to an ac system. A capacitor is connected in parallel across the dc side of the voltage source PWM converter; a shunt connected resistor is modeled in the dc bus. As shown in the diagram, the voltages v_{a1}, v_{b1} and v_{c1} denote three-phase line-to-neutral voltages injected by the PWM converter to the ac system. The vvoltages v_a, v_b and v_c represent the three-phase line-to-neutral voltages at the point of common coupling (PCC). The equivalent impedance between the between the VSC and the PCC is represented as a series connected resistance and inductance.

In the d-q vector control frame, the voltage balance equation at the interconnection of converter and ac system is:

$$\begin{bmatrix} v_d \\ v_q \end{bmatrix} = R \begin{bmatrix} i_d \\ i_q \end{bmatrix} + L \frac{d}{dt} \begin{bmatrix} i_d \\ i_q \end{bmatrix} + \omega_s L \begin{bmatrix} -i_q \\ i_d \end{bmatrix} + \begin{bmatrix} v_{d1} \\ v_{q1} \end{bmatrix} \quad (1)$$

Where, ω_s is the ac system angular frequency. v_d, v_q, v_{d1}, and v_{q1} represent the d and q components of the PCC voltages and the VSC output voltages, respectively. The currents i_d and i_q represent the d and q components of the current flowing between the ac system and the VSC.

Equation (1) can be expressed by a complex equation (2) using space vectors where

v_{dq}, i_{dq} and v_{dq1} are instantaneous space vectors of the PCC voltage, line current and VSC output voltage. Under the steady-state condition, the equation (2) can be represented as equation (3), where V_{dq}, V_{dq1} and I_{dq} stand for the steady-state space vectors of the PCC and VSC output voltages and line current

$$v_{dq} = R * i_{dq} + L\frac{d}{dt}i_{dq} + j\omega_s L * i_{dq} + v_{dq1} \quad (2)$$

$$V_{dq} = R * I_{dq} + j\omega_s L * I_{dq} + V_{dq1} \quad (3)$$

The instantaneous active and reactive powers from the ac system to the converter are proportional to the d-, q-axis currents respectively as shown by (4) and (5).

$$p_{ac}(t) = v_d i_d + v_q i_q = v_d i_d \quad (4)$$

$$q_{ac}(t) = v_q i_d - v_d i_q = -v_d i_q \quad (5)$$

Assuming the $V_{dq1} = V_{d1} + jV_{q1}$ and neglecting the resistance, the current flowing from the ac system to the VSC is:

$$I_{dq} = \frac{V_{dq1} - V_{dq}}{jX_L} = \frac{V_{d1} - V_d}{jX_L} + \frac{V_{q1}}{X_L} \quad (6)$$

in which, $X_L = j\omega_s L$ is the reactance of the converter transformer and reactor between the VSC and the PCC. The power transfer from ac system to VSC could be

$$P_{ac} + jQ_{ac} = V_{dq} I_{dq}^* = V_d I_{dq}^* \quad (7)$$

By solving (6) and (7),

$$P_{ac} = -\frac{V_d V_{q1}}{X_L} \quad (8)$$

$$Q_{ac} = \frac{V_d}{X_L}(V_d - V_{d1}) \quad (9)$$

The conventional VSC control of an HVDC light system has a nested-loop control structure including a slower outer and a faster inner current loop control loop that generates

d-axis and q-axis current references i_d^* and i_q^* to the current loop controller.

Now, the VSC is used for active-power control, the d axis current reference, according to (8), is：

$$i_d^* = \frac{P_{ac}^*}{V_d} \tag{10}$$

where, P_{ac}^* is the designated active power delivered from the ac to the dc system, and if the VSC is used for dc voltage control, the d-axis current reference is generated by a dc voltage loop controller.

For reactive-power control, the q-axis current reference, according to (9), is

$$i_d^* = \frac{-Q_{ac}^*}{V_d} \tag{11}$$

where, Q_{ac}^* is a desired reactive power of the ac system. For PCC voltage control, the q-axis current reference i_q^* is obtained based on the error signal between the PCC voltage set point and the actual PCC voltage to be controlled.

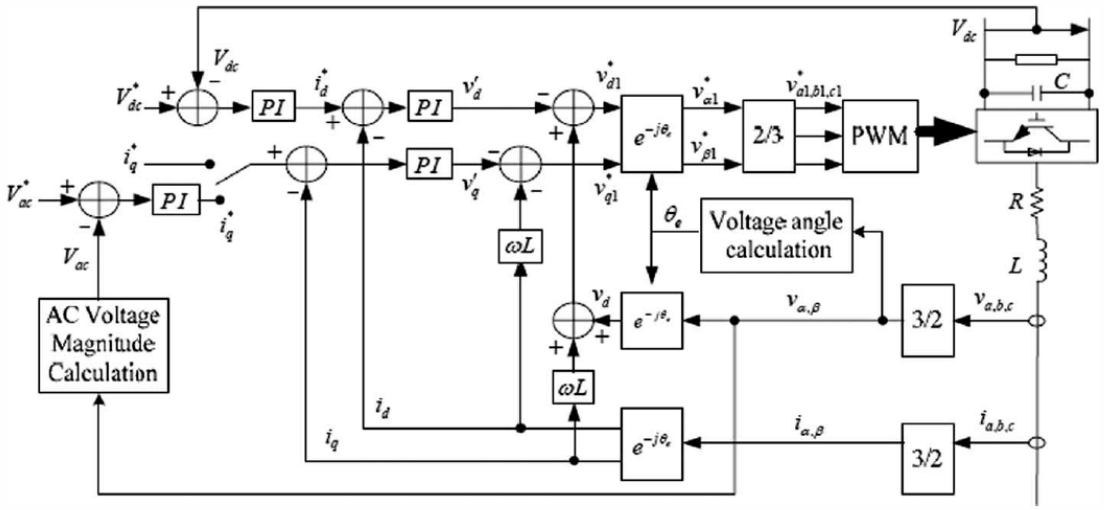

Figure 17 Conventional d-q vector control structure.

Figure 17 shows the overall traditional *d-q* vector control structure, where the voltage source converter is used for the dc voltage control. The two reference voltages, v_{d1}^{*} and v_{d1}^{*}, are used to generate a set of three-phase sinusoidal reference voltage, v_{a1}', v_{b1}', and v_{c1}' to control the PWM converter.

$$v_{d1}^{*} = -v_{d}' + \omega_s L_{i_q} + v_d \tag{12}$$

$$v_{q1}^{*} = -v_{q}' - \omega_s L_{i_d} \tag{13}$$

4.2 Oscillations Detection Methods

4.2.1 Modal analysis

Modal analysis, known as eigenvalue analysis, is a systematic technique for identifying oscillation modes [63] [64] [65] [66]. The modal analysis also makes linear controller design possible. Assume the linearized power system model around its operating point is given by Equation (14), where x, u, y, A, B, C, and D denotes state vector, input vector, output vector, and state-space matrices, respectively. Equation (14) can also be written in the frequency domain as in Equation (15) by applying Laplace transform where $\mathrm{x}(0)$, s and I are initial state vector, Laplace operator, and identity matrix, respectively. Then system eigenvalues, i.e., $\lambda = \lambda_1, \lambda_2, \dots, \lambda_n$, can be calculated by solving the characteristic equation $\det(A - \lambda I) = 0$.

$$\begin{cases} \Delta\dot{x} = A\Delta x + B\Delta u \\ \Delta y = C\Delta x + D\Delta u \end{cases} \tag{14}$$

$$\begin{cases} x(s) = (sI - A)^{-1}[x(0) + Bu(s)] \\ y(s) = C(sI - A)^{-1}[x(0) + Bu(s)] + Du(s) \end{cases} \tag{15}$$

The eigenvalues can be either positive/negative real or complex conjugates. A real value eigenvalue corresponds to a non-oscillatory mode, while a sophisticated conjugate pair, such as $\lambda = \sigma \pm j2\pi f$ describes an oscillatory mode, where σ and f are the damping factor and the oscillation frequency, respectively. The damping ratio ζ, given in equation (16), is a measure describing how the corresponding oscillation decays after a disturbance. A critical mode that should be damped by a compensator is the one whose damping ratio is less than 0.05, which is a generally accepted standard in inter-area oscillation studies [67] [68] [69]. Table 5 shows typical low-frequency electromechanical modes of a power system [70].

$$\xi = \frac{-\sigma}{\sqrt{\sigma^2+w^2}} \tag{16}$$

TABLE 5. LOW-FREQUENCY ELECTROMECHANICAL MODES

Mode number	Eigenvalue (p.u.)	Damping ratio (%)	Oscillation frequency (Hz)
1	$-0.111 \pm j2.576$	4.31	0.410
2	$-0.133 \pm j3.270$	4.06	0.520
3	$-0.167 \pm j3.963$	4.20	0.631
4	$-0.244 \pm j5.005$	4.86	0.797

When the more than one critical mode exists in the system, the damping controller should be designed according to the one that dominates system dynamics, by examining the controllability B and observability C matrices given in equation (17), where ϕ is the right eigenvector. Then, a scalar quantity, called residue R_i for mode- i, given in equation (18) can be introduced as the product of controllability and observability indices. R_i is a sensitivity indicator to a feedback between input and output. H is the gain of the damping controller which shifts λ_i to the left in complex plane by keeping it parallel to the real axis. In other words, the sum of the phase angles R_i and H should be equal to $180°$ [39] [40].

$$\begin{cases} B' = \phi^{-1}B \\ C' = C\Phi \end{cases} \tag{17}$$

$$\Delta\lambda_i = \Delta\sigma_i + j\Delta w_i = R_i H(\lambda_i) \tag{18}$$

4.2.2 Prony method

The Fourier transform can separate the major frequency components in the time domain and then identify each of them individually in the frequency domain by using output swing curves [71]. Damping parameters of the primary frequency components describing the stability of the large interconnected power systems can then be determined. The Prony method is an advanced version of Fourier transform that can be used to estimate the magnitude A_i, damping factor σ_i, frequency f_i, and the phase θ_i of the i-the component of a given discrete signal $y(k)$, as shown is equation (19) [72] [73]. k and L stands for sampling index and model order, respectively. By applying Euler rule to equation (19), and equation (20) is derived.

$$y(k) = \sum_{i=1}^{L} A_i e^{\sigma_i t} \cos(2\pi f_i t + \theta_t), k = 0,1,2,...,(N-1) \tag{19}$$

$$y(k) = \sum_{i=1}^{L} A_i e^{j\theta_i} e^{\lambda_i k}, k = 0,1,2,...,(N-1) \tag{20}$$

The Prony method can be summarized in three stages. In stage-1, a linear predicted model from observed data is obtained as given in equation (19) and solved for a_i. In stage-2, the roots of the characteristic equation of the linear predicted model, given in equation (20), are computed using least square estimates. In stage-3, the original linear equation set is solved for the magnitude and the phase. After estimating the eigenvalues, damping factor and the oscillation frequency are derived.

$$\mathrm{y[k]} = a_1 y[k-1] + a_2 y[k-1] + \cdots + a_L y[k-L] \tag{21}$$

$$\lambda^L - a_1\lambda^{L-1} - \cdots - a_{L-1}\lambda - a_L = (\lambda - \bar{\lambda}_1)(\lambda - \bar{\lambda}_2) \ldots (\lambda - \bar{\lambda}_L) \tag{22}$$

The main advantage of this method is that it does not require a linearized system model.

Subsequently, the method can be applied in real-time oscillation tracking applications utilizing synchronizing phasor measurement unit (PMU) [74] [75] [76] [77]. Recently an online Prony identification has been proposed to tune damping controller parameters according to the changes in swing frequencies [78]. Measurement or communication noise is the primary concern that negatively affects Prony performance. Alternative versions have been proposed to overcome such problems [80]. On the other hand, the Tufts–Kumaresan method is a new refinement for the Prony method that can estimate the target parameters accurately without implementing any recursive process requiring multiple runs [82].

4.2.3 Kalman filtering

The Kalman filtering method is by estimation, which enables electromechanical oscillatory modes in power systems using dynamic data, such as, currents, voltages and phase angle differences measured by PMU. The method can provide small prediction error in a relatively short execution time. Different from the Prony method, Kalman filtering techniques can cope with persistent measurement noise. On the other hand, the Prony method works well for detecting multi-modes under an unknown parameter set. At first, the output of the linearized model $y(k)$ to be estimated is written as in equation (23) in terms of time series with noise $e(k)$ where k is the sampling time. The prediction value of $y(k)$ up to $(k-1)$ can then be expressed as given in equation (24). One of the targets of the prediction problem is to find the coefficients a_i in equation (23) by minimizing equation (25) with least square estimates. The poles which give the information about the dynamics of the discrete system are the roots of equation (26).

$$y(k) = \sum_{i=1}^{n} a_i y(k-1) - e(k) \tag{23}$$

$$\hat{y}(k \mid k-1) = e(k) + y(k) \tag{24}$$

$$J = \min_{a_i} \sum e^T e = \min_{a_i} \sum (\hat{y}(k \mid k-1) - y(k))^2 \tag{25}$$

$$nz - a_1 z^{n-1} - \ldots - a_{n-1} z - a_n = 0 \tag{26}$$

4.2.4 Hilbert-Huang Transform

The Hilbert-Huang Transform (HHT) is one of the classic analysis methods for nonlinear and non-stationary systems to extract oscillation characteristics, such as magnitude, frequency, and the damping ratio of a measured signal. HHT is divided into two steps, namely Hilbert transform and empirical mode decomposition (EMD) proposed by Huang. The function of EMD is to disperse different frequencies in the signal. The instantaneous values of magnitude and frequency of the system response are calculated as a function of time, the data, later on, are used to calculate the damping ratio and the natural frequency of the signal. For a given time-domain signal $x(t)$, HHT is calculated using the indefinite integral given in Eq. (27), where PV is the Cauchy principal value. Later on, $xH(t)$ is represented as the imaginary part of a complex time-domain signal $z(t)$, given in Eq. (28). Finally, time-dependent magnitude and the phase angle of $z(t)$ is calculated as in Eq. (29) to estimate the quantities of $x(t)$ such as, magnitude, frequency, and damping ratio. HHT can cope with nonlinear non-stationary signals. The disadvantages of this transformation are the computation burden and noisy-biased signals. Moreover, stopping criteria, intermittency, and border effects are challenging problems of HHT.

$$x_H(t) = H[x(t)] = \frac{1}{\pi} PV \int_{-\infty}^{\infty} \frac{x(\tau) d\tau}{\tau - t} \tag{27}$$

$$z(t) = x(t) + j \cdot x_H(t) \tag{28}$$

$$\begin{cases} A(t) = \sqrt{\left(x(t)^2 + x_H(t)^2\right)} \\ \varphi(t) = \arctan\dfrac{x_H(t)}{x(t)} \end{cases} \tag{29}$$

4.2.5 System identification

System identification (SI) methods provide a system model which describes the power oscillatory behavior by mapping input and output data obtained from PMU measurements of synchronized voltage, current and frequency [81] [82]. SI is performed offline or online with sliding window techniques to derive a black box model of the system, as given in Eq. (30) where x, u, e, and y denote vectors of state, input, measurement noise, and output at sampling instant k, respectively, A_d, B_d, C_d and D_d are the state-space matrices of the discrete system. In regular updated intervals, this equivalent model is analyzed with modal analysis which provides information for oscillations [81]. The Tustin method transforms from discrete to continuous time domain to obtain eigenvalues, hence dominant oscillation modes. In literature, SI methods such as numerical algorithms for subspace state space system identification (N4SID) and stochastic subspace identification (SSI) exhibit satisfactory results in damping control applications [82] [83].

$$\begin{cases} x_{k+1} = A_d x(k) + B_d u(k) + K_d e(k) \\ y_k = C_d x(k) + D_d u(k) + e_k \end{cases} \tag{30}$$

4.3 Power Oscillation Control Scheme for Embedded HVDC System

In an embedded HVDC system, at least two HVDC terminals are connected within the same ac network. This feature allows the HVDC link to attenuate the power oscillation in the ac system.The additional power used for oscillation dampings can be calculated according to the optimal control method using the inputs: (i) Temporary frequency difference between the converter stations; (ii) Generator rotor speed difference; (iii) Power transmission between the two ac systems [86].

A new power oscillation control scheme for the embedded HVDC system is proposed in this chapter. The proposed control strategy is based on the operation of embedded HVDC systems, where the dc system utilizes VSC-HVDC technology.

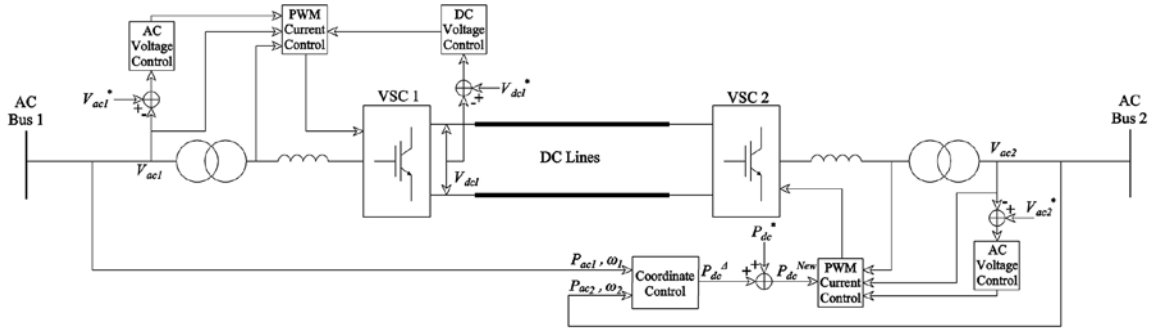

Figure 18. The configuration of a VSC-HVDC transmission system involving d-q vector control and oscillation control strategy.

A simplified embedded HVDC configuration is depicted in Figure 18. As shown in the diagram, each VSC station is connected to the ac system via an equivalent impedance and a transformer. The impedance represents the reactor connecting between the VSC station and the ac network. One VSC station acts as an inverter, and the other VSC station works as the rectifier according to active power flow direction. Each VSC station can independently control the active and reactive power by applying PWM controls to the

converters.

Because of the law of conservation of energy, the active power entering and leaving the HVDC system must be equal when neglecting the losses. The dc bus voltage is maintained by one converter, and the power is controlled by the other one.

The control strategy of the VSC-HVDC link in Figure 2 includes conventional control and proposed frequency control. The power control method is the conventional d-q vector control based PI control [61].

In order to implement this control topology, the direct-quadrature-zero transformation is required to convert the three-phase quantities into d-q reference frame via Park's transformation. Then, the outer control loop generates the d-q current references according to the control objectives. Finally, the inner current control loop regulates the d-q currents and generates the appropriate switching pulses for the rectifier and inverter. By applying the procedures above, this system can fully control the dc voltage at the rectifier station and control the power flow at the inverter station.

As depicted in Figure 18, the VSC-HVDC link operates in parallel with a long ac transmission line or network, the overall active power leaving bus 2 is the sum of the active power transmitted on ac and dc links:

$$P_2 = P_{2,ac} + P_{2,dc} \tag{31}$$

The instantaneous voltage at bus 1 and bus 2 can be written as:

$$v_1 = \sqrt{2}E_1 \sin\left(\omega_1 t + \theta_{1,0}\right) \tag{32}$$

$$v_2 = \sqrt{2}E_2 \sin\left(\omega_2 t + \theta_{2,0}\right) \tag{33}$$

Since the two buses are in the same ac system, the frequencies at the two terminals can

be represented as:

$$\omega_1 = \omega_0 + \omega_{1,\Delta} \tag{34}$$

$$\omega_2 = \omega_0 + \omega_{2,\Delta} \tag{35}$$

Then,

$$\omega_1 t + \theta_{1,0} = \omega_o t + (\omega_{1,\Delta} t + \theta_{1,0}) \tag{36}$$

$$\omega_2 t + \theta_{2,0} = \omega_o t + (\omega_{2,\Delta} t + \theta_{2,0}) \tag{37}$$

Denote, $\delta_1 = \omega_{1,\Delta} t + \theta_{1,0}$ and $\delta_2 = \omega_{2,\Delta} t + \theta_{2,0}$

This can be written as the equations of the instantaneous voltage at the terminals:

$$v_1 = \sqrt{2} E_1 \sin(\omega_o t + \delta_1) \tag{38}$$

$$v_2 = \sqrt{2} E_2 \sin(\omega_o t + \delta_2) \tag{39}$$

The difference of the phase angle is given by

$$\delta_1 - \delta_2 = \left(\omega_{1,\Delta}, t + \theta_{1,0}\right) - \left(\omega_{2,\Delta} t + \theta_{2,0}\right)$$

$$= \left(\omega_{1,\Delta} - \omega_{2,\Delta}\right) * t + \left(\theta_{1,0} - \theta_{2,0}\right)$$

$$= \left[\left(\omega_0 + \omega_{1,\Delta}\right) - \left(\omega_0 + \omega_{2,\Delta}\right)\right] * t + \left(\theta_{1,0} - \theta_{2,0}\right)$$

$$= (\omega_1 - \omega_2) * t + (\theta_{1,0} - \theta_{2,0}) \tag{40}$$

Assume, $\omega_\Delta = \omega_1 - \omega_2$, and $\theta_{\Delta,0} = \theta_{1,0} - \theta_{2,0}$

as a result

$$\delta_1 - \delta_2 = \omega_\Delta * \mathrm{t} + \theta_{\Delta,0} \tag{41}$$

The active power transferred by the ac line can be calculated as:

$$P_{2,ac} = \frac{E_1 E_2}{x_{12}} \sin(\delta_1 - \delta_2)$$

$$= \frac{E_1 E_2}{x_{12}} \sin\left(\omega_\Delta \, \mathrm{t} + \theta_{\Delta,0}\right) \tag{42}$$

Also, in the s domain:

$$\mathbf{P_{2,ac}(s)} = \frac{E_1E_2}{x_{12}} * \frac{s*sin\theta_{\Delta,0}+\omega_\Delta*\cos\theta_{\Delta,0}}{s^2+{\omega_\Delta}^2} \tag{43}$$

Since ω_Δ is a small value, ${\omega_\Delta}^2$ is negligible.

$$\mathbf{P_{2,ac}(s)} = \frac{E_1E_2}{x_{12}} sin\theta_{\Delta,0} * \frac{1}{s} + \frac{E_1E_2}{x_{12}} cos\theta_{\Delta,0} * \omega_\Delta * \frac{1}{s^2} \tag{44}$$

where, $\frac{E_1E_2}{x_{12}} sin\theta_{\Delta,0}$ and $\frac{E_1E_2}{x_{12}} cos\theta_{\Delta,0}$ are constant.

Denote $K_1 = \frac{E_1E_2}{x_{12}} sin\theta_{\Delta,0}$, and $K_2 = \frac{E_1E_2}{x_{12}} cos\theta_{\Delta,0}$

$$\mathbf{P_{2,ac}(s)} = K_1 * \frac{1}{s} + K_2 * \frac{1}{s^2} * \omega_\Delta \tag{45}$$

The inverse transform of the $\mathbf{P_{2,ac}(s)}$ in the time domain is

$$P_{2,ac} = K_1 + K_2 * \omega_\Delta * t \tag{46}$$

Denote,

$$P_{2,ac} = {P_{2,ac}}^* + {P_{2,ac}}^{osc} \tag{47}$$

$$P_{2,dc} = {P_{2,dc}}^* + {P_{2,dc}}^{damp} \tag{48}$$

Therefore, K_1 can be considered as the designated power flow and $K_2 * \omega_\Delta * t$ is the power oscillation along the ac transmission lines.

In s domain,

$$\mathbf{{P_{2,ac}}^{osc}(s)} = K_2 * \frac{1}{s^2} * \omega_\Delta \tag{49}$$

The overall power flow between the two terminals is the summation of the power transmission of ac and dc. It is possible to set up the dc transmission to balance the power oscillation in the ac system to attenuate the overall power oscillation between the two terminals.

Therefore,

$$P_2 = {P_{2,ac}}^* + {P_{2,ac}}^{osc} + {P_{2,dc}}^* + {P_{2,dc}}^{damp}$$

$$= {P_2}^* + {P_2}^{osc} \quad (50)$$

where,

$${P_2}^* = {P_{2,ac}}^* + {P_{2,dc}}^* \quad (51)$$

$${P_2}^{osc} = {P_{2,ac}}^{osc} + {P_{2,dc}}^{damp} \quad (52)$$

To attenuate the overall power oscillation is to minimize the ${P_2}^{osc}$ value.

In s domain,

$$\mathbf{P_2}^{\mathbf{osc}}(\boldsymbol{s}) = K_2 * \frac{1}{s^2} * \omega_\Delta + \mathbf{P_{2,dc}}^{\mathbf{damp}}(\boldsymbol{s}) \quad (53)$$

The ideal design of the damping signal to minimize the overall oscillation is

$$\mathbf{P_{dc_2}}^{\mathbf{damp}}(\boldsymbol{s}) = -K_2 * \frac{1}{s^2} * \omega_\Delta \quad (54)$$

The ac voltages are subject to system conditions and not always constant; therefore, the value of K_2 will not always be a constant in practical projects. In order to diminish these influences from system behavior uncertainty, a PI controller is introduced. The new damping signal is

$$\mathbf{P_{dc_2}}^{\mathbf{damp}}(\boldsymbol{s}) = K_3 * \frac{1}{s} * (1 + \frac{K_4}{s}) * \omega_\Delta \quad (55)$$

where, K_3 and K_4 are constant. K_3 can be considered as the gain in the control loop and $(1 + \frac{K_4}{s})$ can be considered as the PI control.

Therefore, in the proposed oscillation control topology, the new reference for the active dc power delivery control reference in real time domain will be ${P_{2,dc}}^{new} = {P_{2,dc}}^* + {P_{2,dc}}^{damp}$, the new reference will equal to the summation of the original designated dc power plus the damping power to compensate the power oscillation raised via the ac transmission

system.

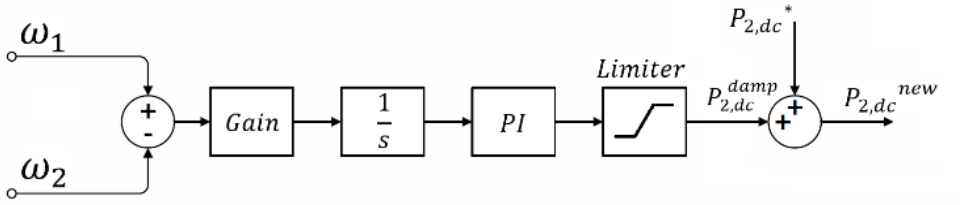

Figure 19. Control loop for the dc power reference.

Figure 19 describes the rectifier station dc power control loop of the proposed power oscillation-attenuating scheme. The active power control signal consists of a PI control and a limiter to maximize the use of installed capacity.

4.4 Coordinate Power Oscillation Control Scheme for the Embedded HVDC System

To further strengthen the system performance, a coordinate control is introduced. The proposed method includes a communication latency compensator and a power oscillation controller.

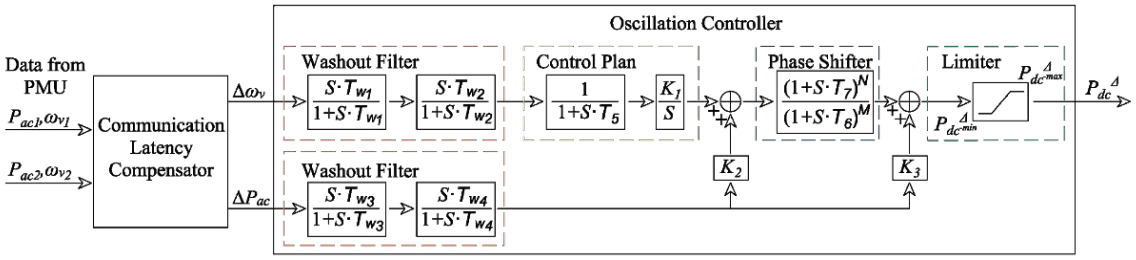

Figure 20. Control loop for the dc power reference.

4.4.1 Communication latency compensator (CLC)

The instantaneous power and frequency signals acquired from both terminals will be transferred to the control as input measures.

The time delays existing in the closed-loop are defined as a round-trip time (RTT) delay in the feedback loop as follows [87]:

$$t_r = t_{sc} + t_c + t_{ca} \tag{56}$$

where, t_r is the RTT delay, t_{sc} is the delay of the feedback channel, t_{ca} is the delay of the forward channel, and t_c is the processing time of the controller.

The length of typical HVDC lines in the application of embedded HVDC is from 70 to 300 kilometers, and the speed of light through the communication cable is roughly two-thirds of the speed of propagation in a vacuum. Therefore, it will generate approximately 10 to 50 μs signal latency for the delay of the forward channel.

A Communication Latency Compensator is introduced to overcome the signal delay as shown in Figure 20. A constant time is implemented to the signal from the remote end, i.e., the signal from bus 1 in Figure 18.

$$\begin{cases} \Delta\omega = \omega_2(t) - \omega_1(t + T^*) \\ \Delta P_{ac} = P_{ac2}(t) - P_{ac1}(t + T^*) \end{cases} \quad (57)$$

In equation (57), the T^* is a constant that can be either calculated by the distance divided by the transfer speed or by practical experiences.

4.4.2 Signal analyzer

The signal analyzer has two input measures: the frequency difference and the ac power difference between the terminal buses. The transfer function loop is depicted in Figure 20.

As shown in Figure 20, the signal of the frequency difference will pass through a washout filter, a control plan, a phase shifter and then a limiter. The signal of the power will transmit through a washout filter then works as a compensational signal. This is because the signal of the power is detected and acquired earlier and faster than the voltage frequency signal. The installation of the power difference loop will improve the overall system performance. The install of a limiter can constraint the overall size of the HVDC system.

The parameter explanation is illustrated in Table 6

TABLE 6. PARAMETERS IN THE SIGNAL ANALYZER LOOP

Parameter	Description	Units	Typical Range
T_{w1}	Wash-out time constant 1	Sec.	0.8 to 10
T_{w2}	Wash-out time constant 2	Sec.	0.8 to 10
T_{w3}	Wash-out time constant 3	Sec.	0.8 to 10
T_{w4}	Wash-out time constant 4	Sec.	0.8 to 10
T_5	Lag time constant	Sec.	0 or 0.02 to 2
T_6	Filter time constant	Sec.	0 or 0.02 to 2
T_7	Ramp-tracking time constant	Sec.	0 or 0.02 to 2
K_1	Gain	p.u./p.u.	0.2 to 20
K_2	Gain	p.u./p.u.	0.5 to 2
K_3	Gain	p.u./p.u.	0.1 to 5
M	Integer filter constant	Integer	1 to 8
N	Integer filter constant	Integer	1 to 8
$P^{\Delta}_{dc\text{-}max}$	Upper limit	p.u.	0.05 to 0.2
$P^{\Delta}_{dc\text{-}min}$	Lower limit	p.u.	-2 to -1

4.5 Paralleled AC-HVDC Test System

To analyze the transient stability and power oscillation behavior of the oscillation control strategy for embedded HVDC systems, it is necessary to have comprehensive modeling and analysis techniques for all components that may interact to produce transient behavior and oscillation phenomenon. Therefore, dynamic models are constructed for the simulation studies.

The system model applied to the dynamic performance study is the 230 kV, 60 Hz, IEEE six-bus four-machine system. The system has four synchronous machines and two dynamic loads. A schematic diagram of the system is described in Figure 21.

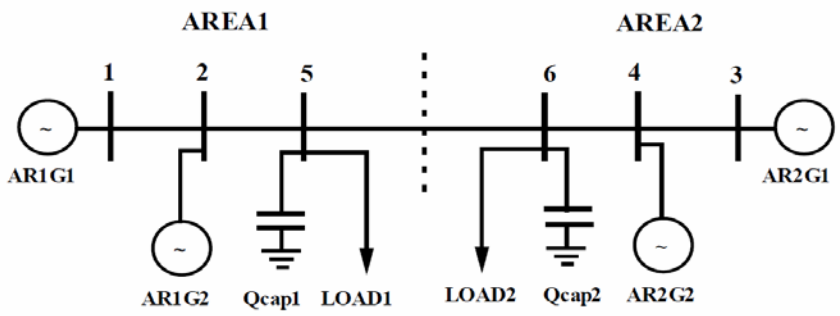

Figure 21. A schematic diagram of the 6-bus 4-machine system.

For steady state stability test, simulations are performed in DSA tools (PSAT, TSAT and SSAT) platform. The IEEE six-bus four-machine system data is shown in APPENDIX A and APPENDIX B. The one-line diagram of the system derived by PSAT is described in Figure 22. In the diagram, the system can be briefly categorized by two areas: buses 1, 2 and 5 are in area 1; buses 3,4 and 6 are in area 2. Each area has two generators and one load. Contingencies can be placed on any bus or any place on lines.

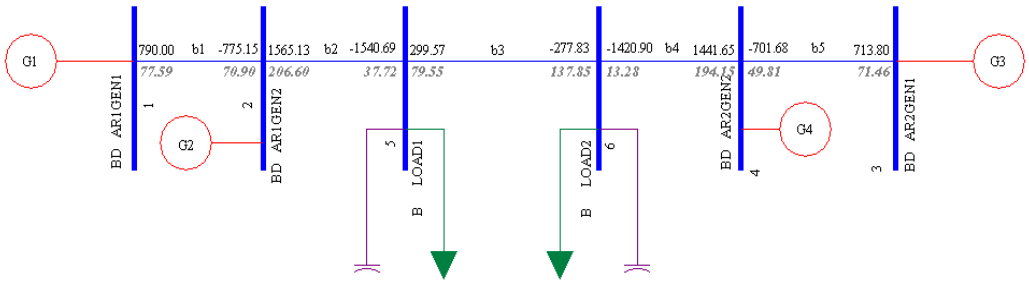

Figure 22. One-line diagram of 6-bus 4-machine system on PSAT.

4.5.1 Electric machines

In the system described in Figure 21 and Figure 22, the synchronous generators (Gen 1, 2, 3, and 4) are connected with buses 1, 2, 3, and 4 via a delta-wye connected transformer,

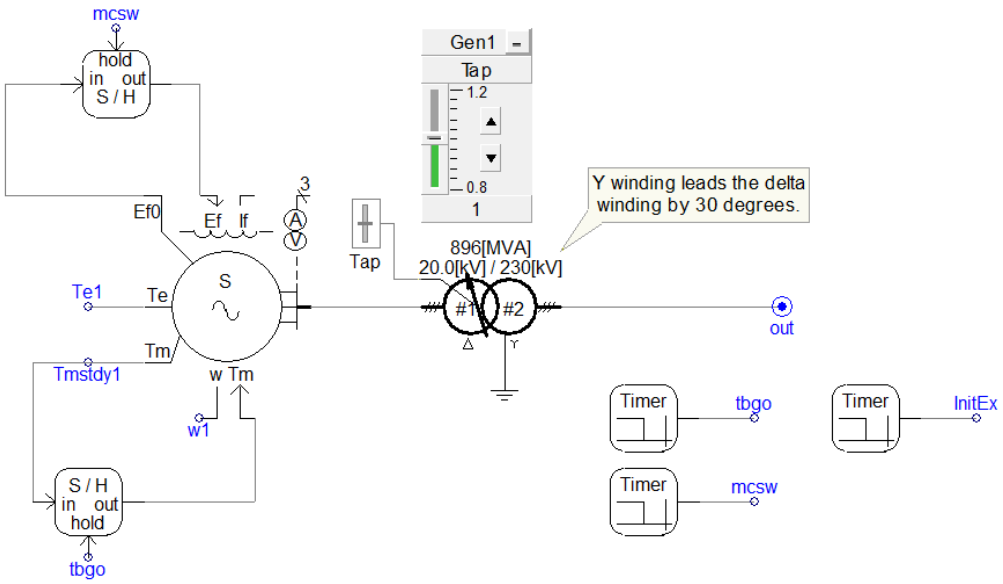

Figure 23. The generator and transformer connection diagram as in PSCAD.

and the delta winding delays Y winding by 30°. The parameters (units in p.u.) for the generators are listed in Table 7, which complies with IEEE standard fossil steam unit, F20, at rated 896 MVA 26 kV. Two-axis models describe the generator simulations. Therefore all values for sub-transient variables are approximately equal to zero.

Figure 23 is the screen capture from the PSCAD program describing the generator and transformer connection diagram.

TABLE 7. EQUIVALENT SYNCHRONOUS MACHINE CONSTANT PARAMETERS

Parameter	Value (p.u.)	Parameter	Value (p.u.)
R_a	0.0025	X_d	1.8
X_q	1.7	X_1	0.2
$X_d{}'$	0.3	$X_q{}'$	0.55
$T_{d0}{}'$	8.0	$T_{q0}{}'$	0.4
$X_d{}''$	0.25	$X_q{}''$	0.25
$T_{do}{}''$	0.03	$T_{qo}{}''$	0.05
H_1	6.5	H_2	6.5
H_3	6.175	H_4	6.175

4.5.2 Exciters

Each generator is equipped with an IEEE (1992/2005) AC3A exciter, which is a typical exciter designed for this kind of generators. The exciter variables are settled at the default values to have a common case study. The parameters of AC3A and the topology are shown in Figure 24. The diagram is a screen capture of TSAT.

4.5.3 Loads

Load 1 and load 2 shown in Figure 24 are three-phase constant power loads. The fixed load models utilize the load characteristics as a function of voltage magnitude and frequency, where the load real and reactive power are considered separately.

The fixed loads are connected in delta connection and rated at 60 Hz.

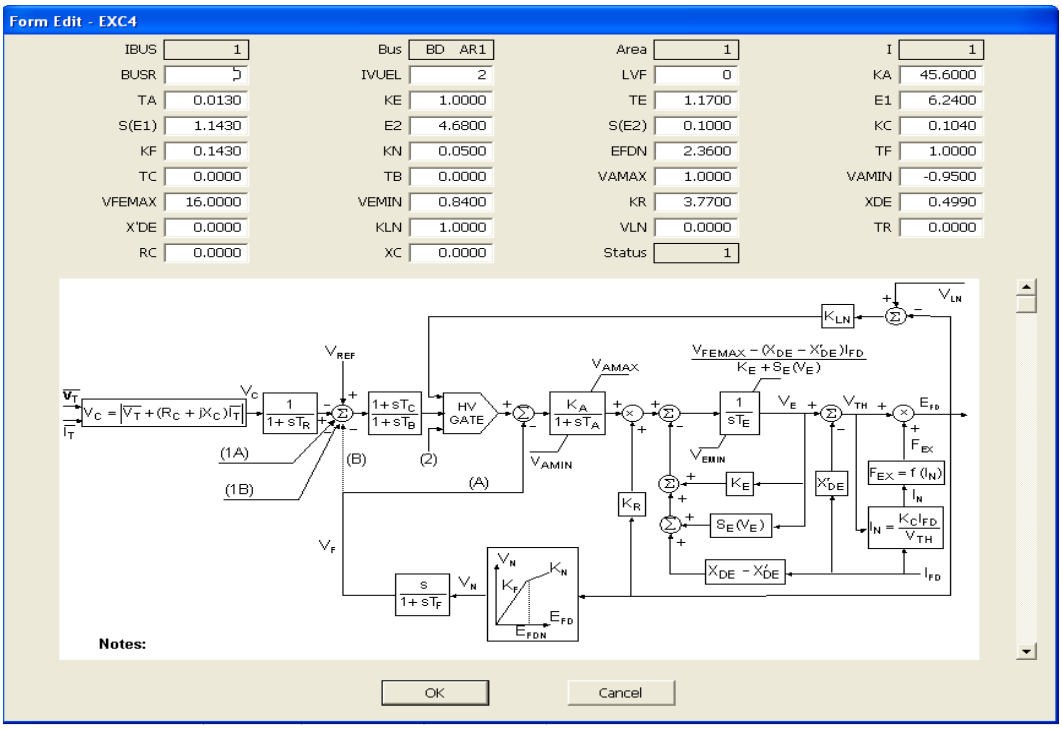

Figure 24. Topology and parameter of exciter AC3A.

The fixed load models comply with the load characteristic, which is a function of voltage magnitude and frequency. The load real and reactive power considered separately by using the expressions:

$$\mathrm{P} = \mathrm{P}_0 * \left(\frac{V}{V_0}\right)^{NP} * (1 + K_{PF} * dF), \tag{58}$$

$$\mathrm{Q} = \mathrm{Q}_0 * \left(\frac{V}{V_0}\right)^{NP} * \left(1 + K_{QF} * dF\right). \tag{59}$$

where,

P is the equivalent load active power.

P_0 is the rated active power at each phase.

V is the load voltage.

V_0 is the rated load voltage.

$NP = \frac{dP}{dV}$ is the voltage index for active power.

$K_{PF} = \frac{dP}{dF}$ is the frequency index for active power.

Q is the equivalent load for reactive power.

Q_0 is the rated reactive power, including the inductive, per each phase.

$NQ = \frac{dQ}{dV}$ is the voltage index for reactive power.

$K_{QF} = \frac{dQ}{dF}$ is the frequency index for reactive power.

The voltage index for active power NP is set to 1, the voltage index for reactive power NQ is set to 2, the frequency indexes for both active and reactive power are set to 0.

4.5.4 Transmission lines

The ac transmission lines are modeled in coupled PI sections. The parameters of the line data area comply with the power flow data in IEEE standard system, as shown in Table 8.

TABLE 8. TRANSMISSION LINE PARAMETERS

Bus Number		Length
From	To	[kilometer]
1	2	25.0
2	5	10.0
5	6	220.0
6	4	10.0
4	3	25.0

4.6 Simulation Studies

In order to study the proposed system dynamic performance, four scenarios are constructed as depicted in Figure 25 and Figure 26. Figure 25 is the system diagram of Scenario I; Figure 26 is the system diagram of Scenarios II, III and IV.

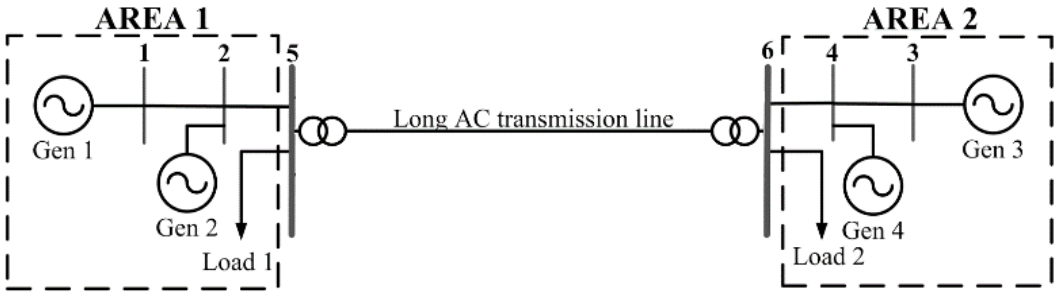

Figure 25. The topology of the test system – scenario I.

In Scenario I, the entire system only consists of ac transmission. The long ac transmission line connects the two areas as shown in this study.

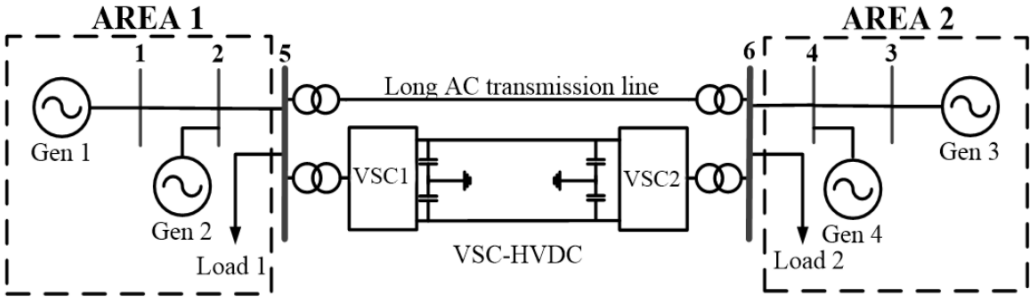

Figure 26. The topology of the test system – scenarios II, III and IV.

In Scenarios II, III and IV, paralleled ac and dc transmission systems connecting two ac areas, as shown in Figure 26. In all the three scenarios, the designated ac transmission line between the two areas is 350 MW. The design dc transmission capacities are 200 MW in Scenarios II and III, and 100 MW in Scenario IV.

The dc technology applied in Scenario II is the VSC-HVDC with conventional d-q

vector control; the dc technology applied in Scenarios III and IV are the VSC-HVDC with the proposed coordinate power oscillation control scheme.

The parameters of the coordinate power oscillation control employed for the simulation studies are shown in Table 9.

TABLE 9. PARAMETERS IN THE SIGNAL ANALYZER LOOP

Parameter	Description	Units	Value
T_{w1}	Wash-out time constant 1	Sec.	2
T_{w2}	Wash-out time constant 2	Sec.	2
T_{w3}	Wash-out time constant 3	Sec.	10
T_{w4}	Wash-out time constant 4	Sec.	10
T_5	Lag time constant	Sec.	0.02
T_6	Filter time constant	Sec.	0.02
T_7	Ramp-tracking time constant	Sec.	0.02
K_1	Gain	p.u./p.u.	1
K_2	Gain	p.u./p.u.	2
K_3	Gain	p.u./p.u.	2
M	Integer filter constant	Integer	6
N	Integer filter constant	Integer	2
$P_{dc\text{-}max}^{\Delta}$	Upper limit	p.u.	0.2
$P_{dc\text{-}min}^{\Delta}$	Lower limit	p.u.	-1

TABLE 10. CAPACITY AND TECHNOLOGY MODELLED IN EACH SCENARIO

	AC Line Capacity	DC Line Capacity	DC Technology
Scenario I	350 MW	0	N/A
Scenario II	350 MW	200 MW	VSC-HVDC with conventional d-q vector control.
Scenario III	350 MW	200 MW	VSC-HVDC with coordinate power oscillation control.
Scenario IV	350 MW	100 MW	VSC-HVDC with coordinate power oscillation control.

Table 10 summarizes the transmission capacities and the dc technology applied in each scenario. As shown in the table, the transmission capacity in scenario I is 350 MW ac; the transmission capacities in scenario II is 350 MW ac plus 200 MW VSC-HVDC with conventional d-q vector control; the transmission capacity in scenario III is 350 MW ac plus 200 MW VSC-HVDC with the proposed control method; the transmission capacity in scenario IV is 350 MW ac plus 100 MW VSC-HVDC with the proposed control method.

4.6.1 Transient stability test

The comparison of the system stabilities among the four scenarios is studied. In the transient stability test, the contingencies are applied to each bus and each line of the system. The line faults are placed at the midpoints of each line. All contingencies are three-phase line-to-ground faults. The transient stability test is performed in the PSCAD platform.

The critical clearing time (CCT) is the maximum period during which a disturbance can be applied without the system losing its stability. The objective of this calculation is to determine the characteristics of protections required by the power system.

By detecting the CCT, the maximum fault durations of each bus and each line are found to evaluate the system transient stability performance in pure ac transmission, embedded HVDC system and embedded HVDC system with the proposed control scheme. The system stability is evaluated according to the phase angle difference between the HVDC terminal buses. Only when the terminal phase angle difference is smaller than 180°, the ac system is within the safety margin.

TABLE 11. THE CRITICAL CLEARING TIME OF THE SCENARIOS

Type of Fault and Location		CCT (second)			
		Scenario I	Scenario II	Scenario III	Scenario IV
Bus Fault	Bus 1	0.12	0.55	0.98	0.70
	Bus 2	0.10	0.6	0.79	0.66
	Bus 3	0.19	0.42	0.5	0.45
	Bus 4	0.22	0.36	0.42	0.37
	Bus 5	0.12	0.38	0.48	0.44
	Bus 6	0.25	0.33	0.41	0.38
	Average	0.167	0.440	0.597	0.500
Line Fault	Bus 1 - Bus 2	0.11	0.56	1.01	0.77
	Bus 2 - Bus 5	0.09	0.47	0.60	0.51
	Bus 4 - Bus 6	0.22	0.34	0.41	0.38
	Bus 3 - Bus 4	0.19	0.42	0.48	0.42
	Average	0.153	0.448	0.625	0.520
Average		0.161	0.443	0.608	0.508

Table 11 shows the simulation results of the four scenarios. For the bus faults, the average CCTs for Scenarios I, II, III and IV are 0.167 s, 0.440 s, 0.597 s and 0.500 s. For the line faults, the average CCTs for Scenarios I, II, III and IV are 0.161 s, 0.443 s, 0.608 s and 0.508 s.

The conclusions can be drawn:

a) The paralleled AC-HVDC transmission system is more stable than the ac transmission alone. Because in Scenario I, the average CCT is the shortest among all four scenarios.

b) In the paralleled AC-HVDC transmission system, the HVDC installed with the proposed coordinate power oscillation control is more stable than the system with conventional d-q vector control. Compare Scenario III to Scenario II, the overall average CCT is increased from 0.443 s to 0.608 second, which is a 37.35% CCT longer.

c) In the paralleled AC-HVDC transmission system, when the HVDC is installed with the proposed power oscillation control scheme, the larger installation of the HVDC capacity will result in the better system stability. Compare Scenario IV to Scenario III; the CCT is shorter in every tested fault condition. The overall average CCT in Scenario IV is 0.508 second, and the overall average CCT in Scenario III is 0.608 second, which is a 16.45% difference.

4.6.2 AC power oscillation attenuation

According to the conclusion drawn in Section 4.5.3, the proposed coordinate power oscillation control strategy can improve the paralleled AC-HVDC transmission system dynamic performance. Therefore, the ac power oscillation is expected to be attenuated when the system is equipped with the proposed control. Two cases are tested to verify the system dynamic performance.

a) Case 1: The contingencies are the three-phase line to ground fault placed on bus 6 with 0.36-second duration for Scenario II and III.

Figure 27 and Figure 28 shows the simulation results.

Figure 27 describes the active power and the phase angle differences of the synchronous machines in Scenarios II and III.

Figure 27(a) illustrates the active power transmission between area 1 and area 2. As shown in the diagram, the dc power swings after the contingency, then stays constant after recovery. The ac power swings after the contingency, then loses the synchronization as shown in the diagram.

Figure 27(b) represents the active power transmission between the two areas. As shown in the diagram, the power transferring between the two regions oscillates, then returns stable after faults.

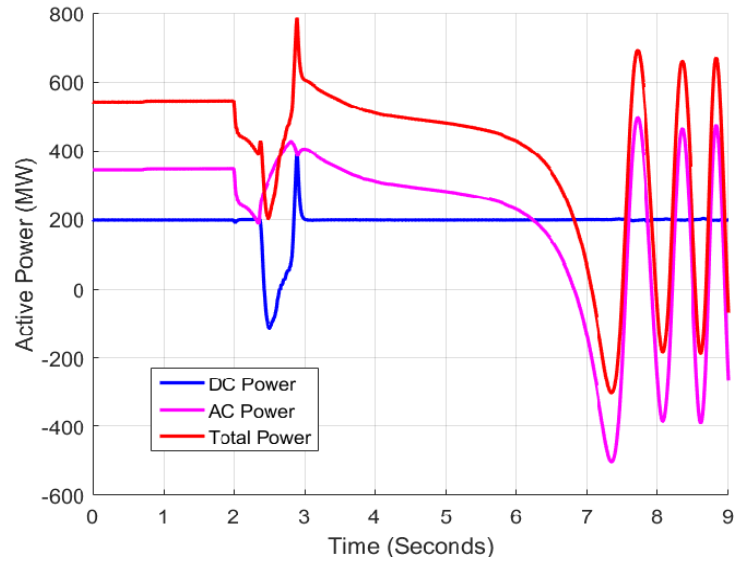

(a) Scenario II

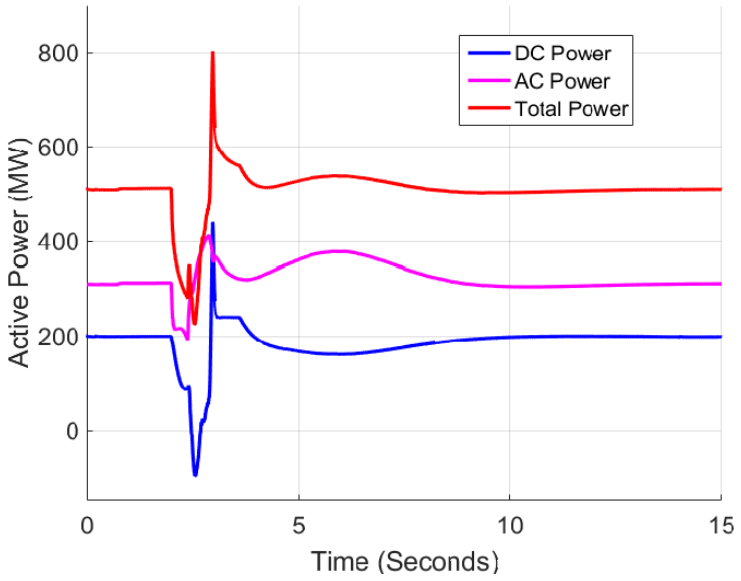

(b) Scenario III

Figure 27. DC, ac and total powers are entering area 2 when the fault happens at bus 6 with 0.36 s duration (a) Scenario II; (b) Scenario III.

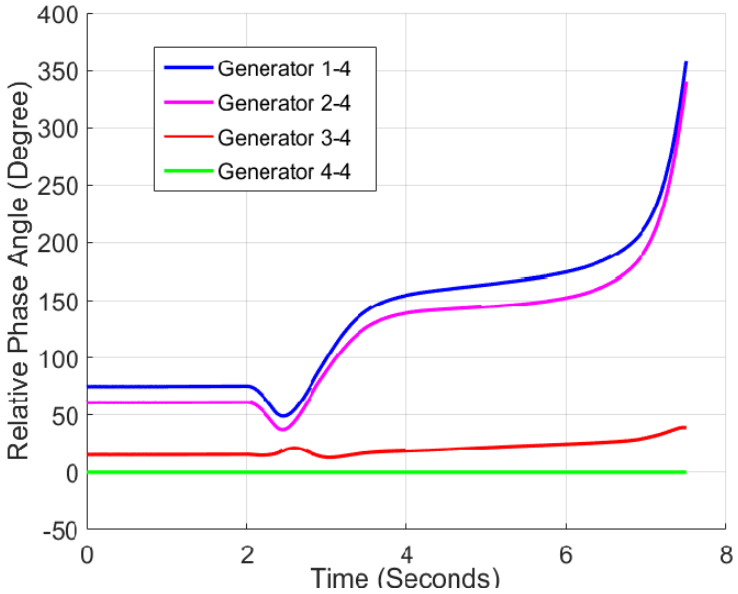

(a) Scenario II

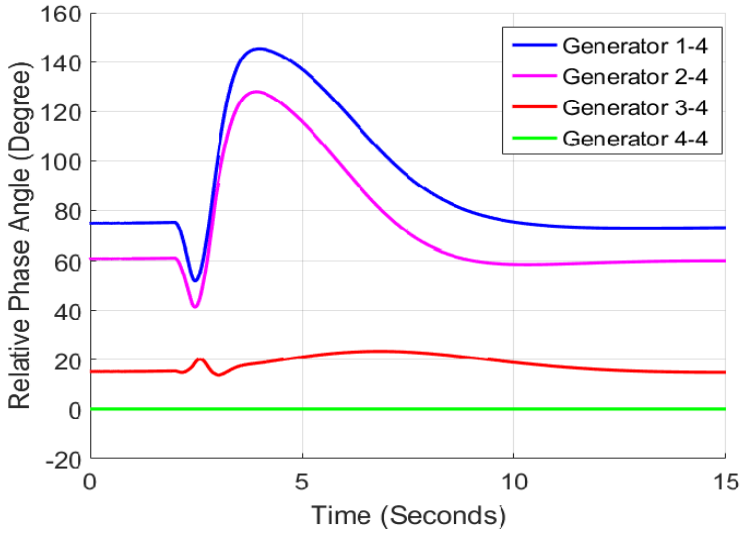

(b) Scenario III

Figure 28. Relative phase angle differences among generators when the fault happens at bus 6 with 0.36-second duration (a) Scenario II; (b) Scenario III.

Figure 28 describes the phase angle difference between each generator under the same contingency. In the plot, the phase angle of generator 4 is appointed as the phase angle

reference, whose angle is set as zero degrees.

Figure 28(a) illustrates the active power transmission between area 1 and area 2. As shown in the diagram, the dc power swings after the contingency then stays constant after the fault recoveries. The ac power loses synchronization as soon as the contingencies are placed. Therefore, the conclusion can be drawn that the system in Scenario II loses stability when a 0.36-second three-phase line to ground fault is applied at bus 6.

Figure 28(b) represents the active power transmission between area 1 and area 2. As depicted in the diagram, both the dc and ac power swings after the contingencies then remain stable after the fault is cleared. Therefore, the conclusion can be drawn that the system in Scenario III remains stable after a 0.36-second three-phase line to ground fault is applied at bus 6.

According to the simulation results, when test systems in Scenarios II and III are applied with the same contingency, the system in Scenario II loses synchronization after the contingency, but the system in Scenario III remains stable.

The conclusion can be drawn that the system in Scenario III is more stable than the system in Scenario II; the proposed control method for the embedded HVDC system can improve the system dynamic performance.

b) Case 2: The contingencies are the three-phase line to ground fault placed on bus 5 with 0.35-second duration for Scenarios III and IV.

In this case, the three-phase line to ground fault is placed on bus 5; the fault time duration is set to 0.35 second. The faults start at 1.0 second. The adjacent bus 2 is selected as the observation point to compare the voltage and frequencies between the two scenarios. The power flow through the paralleled ac transmission line is determined.

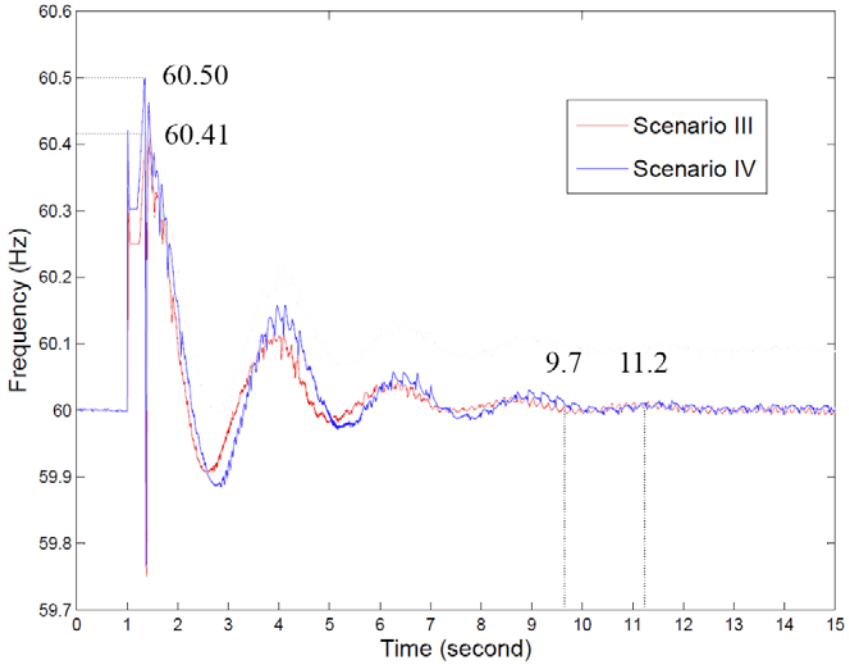

Figure 29. The frequencies measured at bus 2 in Scenarios III and IV.

Figure 29 shows the frequencies measured at bus 2 in Scenario III and Scenario IV. As shown in the diagram, Scenario III has a better frequency dynamic performance than Scenario IV. The highest frequency mismatches in Scenario III and IV are 60.41 Hz and 60.50 Hz. The frequency recovers at 9.7 s in Scenario III and recovers at 11.2 s in Scenario IV.

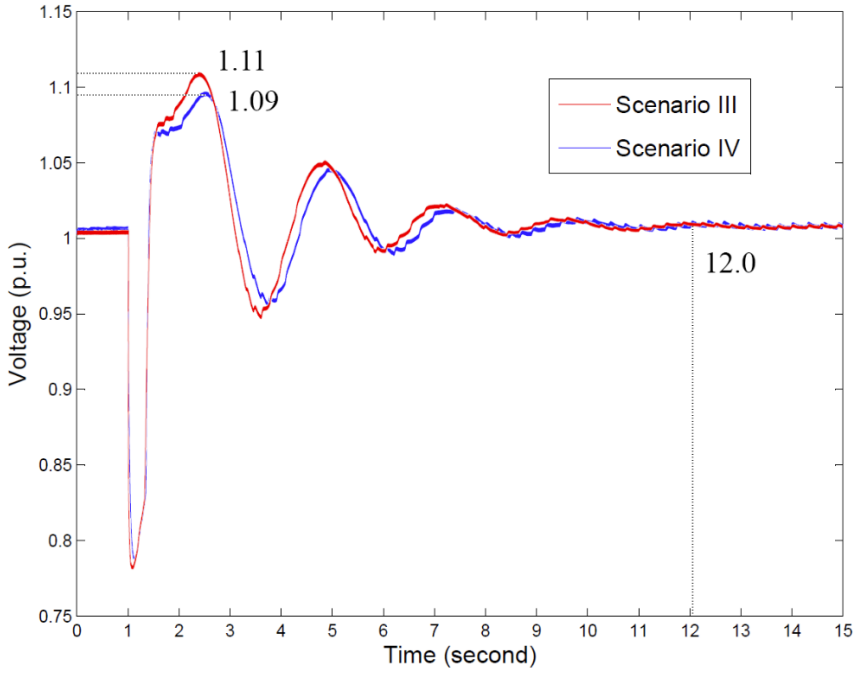

Figure 30. The voltages measured at bus 2 in Scenarios III and IV.

Figure 30 shows the voltages measured at bus 2 in Scenarios III and Scenario IV. As shown in the diagram, the voltage dynamic performances are similar. The voltage pulse magnitude after the fault is 1.11 p.u. in Scenario III, which is slightly larger than that in Scenario IV, 1.09 p.u. In both Scenarios III and IV, the voltages recover at around 12.0 second.

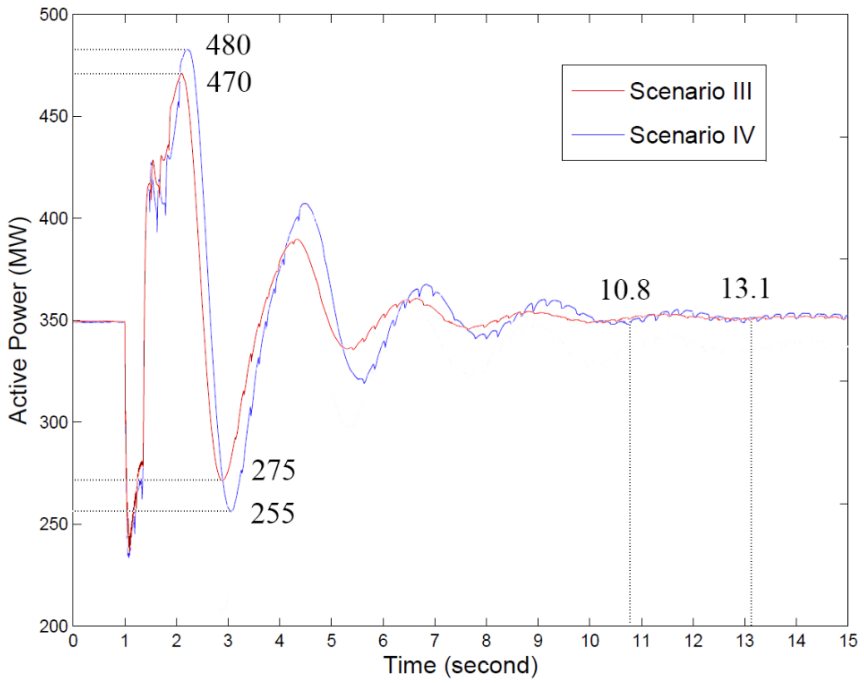

Figure 31. The active power flow through the parallel ac transmission line measured at bus 5 in Scenarios III and IV.

Figure 31 shows the active power flow through the parallel ac transmission line measured at bus 5 in Scenarios III and IV.

In Scenario III, the active power changes from 275 MW to 470 MW after the fault, and the power recovers at 10.8 s. In Scenario IV, the active power changes from 255 MW to 480 MW after the fault and the power recover at 13.1 s.

According to the simulation results, the conclusion can be drawn that in the paralleled AC-HVDC transmission system, when the HVDC is installed with the proposed power oscillation control scheme, a larger HVDC capacity installation will result in a better frequency and active power dynamic performance.

CHAPTER 5

NONLINEAR VOLTAGE DROOP CONTROL STRATEGY

In an MTDC grid, it is expected that at the condition of an outage of one or more converters, all the remaining converters should share the resulting power imbalance in certain appropriate proportions. Rather than regulate the converter dc voltage and power at a fixed value, the droop control scheme regulates the voltage and power within a certain margin. All the converters with the droop control strategy will adjust the dc voltage and share the power according to the droop control characteristics. All the existing voltage droop control characteristics employ linear relationships between the voltage and power, i.e., the droop control will have the same response to all system operating conditions. It is possible to determine a nonlinear voltage droop control strategy to accomplish specific system operation and dynamic response requirements.

In this chapter, a nonlinear voltage droop control strategy is proposed, and a common design procedure for the nonlinear droop control strategy is described. As an example, a quadratic droop control scheme is illustrated in Section 5.1.

To validate the principle, a hybrid AC-MTDC test system is employed. This test system, proposed in this article, consists of two ac grid, two wind farms and a five-terminal MTDC connecting them. The detailed system description is demonstrated in Section 5.2.

Three droop control schemes including the detailed design procedures and parameters are proposed in Section 5.3: a linear droop control scheme, a quadratic droop control scheme and a hybrid linear-nonlinear droop control scheme.

The simulation results are illustrated in Section 5.4. The comparison among the three control schemes are discussed, and the conclusions are drawn.

5.1 Nonlinear Voltage Droop Control Strategy Design Principles

The voltage droop control strategy is originated from the frequency droop control strategy in the ac grid, where a change in power demand level will result in a change of the frequency. The dc voltage controlling converter acts as the slack bus within the MTDC grid. The active power flows through this converter will be cumulative of the power transferred by other converters minus the losses within the dc system.

It is worthy to notice that the dc voltage at each terminal does not has the same voltage magnitude in the entire dc grid because the power flow between the dc terminals must obey the Kirchhoff's Voltage Law (KVL).

The dc voltages at each terminal will directly control their dc power according to the voltage droop characteristics. A conventional voltage droop control usually applies a proportional controller. The dc voltage droop control can be described as:

$$V_i - V_i^* = \beta_i (P_i - P_i^*) \tag{60}$$

β_i is the droop coefficient at the dc bus i. V_i^* and P_i^* are the references to control the converter voltage and power.

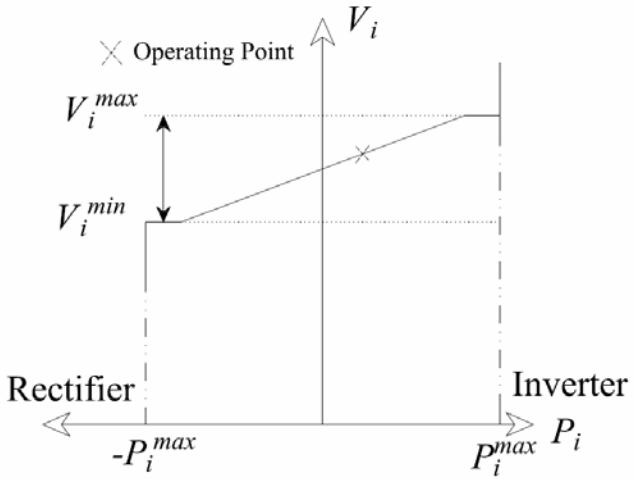

Figure 32. Droop control characteristics.

Figure 32 shows the droop control characteristic. In the diagram, V_i^{max} and V_i^{min} are the upper and lower limits of the dc power control, which should be within the constrains determined by the converter stations.

The voltage droop control strategy can be categorized as a procedure to use the voltage converter to set up the active power reference. A more generalized relationship can be proposed $(\mathrm{P_i} - \mathrm{P_i^*})$ is a function of $(\mathrm{V_i} - \mathrm{V_i^*})$, as

$$\mathrm{P_i} - \mathrm{P_i^*} = f_i(\mathrm{V_i} - \mathrm{V_i^*}) \tag{61}$$

Therefore, $(\mathrm{V_i} - \mathrm{V_i^*})$ can be determined by the reversed function,

$$(\mathrm{V_i} - \mathrm{V_i^*}) = f_i^{-1}\ (\mathrm{P_i} - \mathrm{P_i^*}) \tag{62}$$

The relationship between the power and voltage does not have to be limited to proportional. The relationship between the power and voltage can be nonlinear.

The design procedures are such:

i. Determine a system reference operating condition. At this operating condition, all the dc terminals are operating at their designed working conditions.

ii. Determine several steady-state operating conditions. These steady state conditions must be within the system power and voltage constraints.

iii. The droop control will be designed according to these steady state conditions and the reference operating point. The droop control can not only be a linear relationship but also be a nonlinear relationship. However, it is should be noticed that within the working margin, the sign of the slope of the proposed nonlinear relationship between voltage and power must be constant.

iv. Hard constraints must be applied to the droop control to ensure the converter is operating within the voltage and power limits.

For example, it is possible to determine a quadratic droop control relationship between the power and voltage,

$$P_i - P_i^* = \alpha_i (V_i - V_i^*)^2 + \beta_i (V_i - V_i^*) + \gamma_i \tag{63}$$

where, α_i, β_i and γ_i are the coefficients of this specific control, V_i^* and P_i^* are the references. It should be noticed that the positive or the negative of the coefficient α_i is determined by the comparison between V_i and V_i^*, or

$$\alpha_i = |\alpha_i| * sgn(V_i - V_i^*) \tag{64}$$

when V_i is greater than V_i^*, α_i is a positive number; when V_i is smaller than V_i^*, α_i is a negative number.

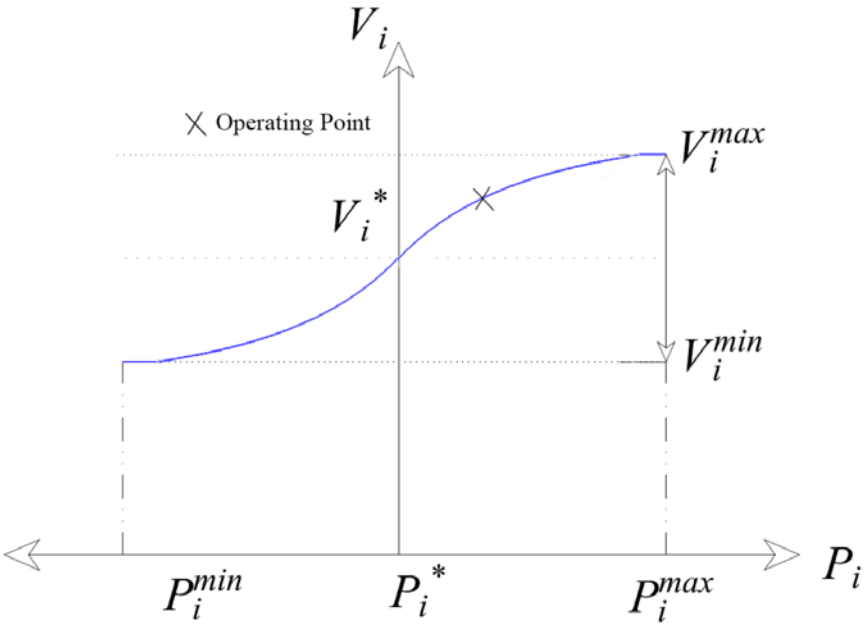

Figure 33. An example of a nonlinear droop control characteristic.

Figure 33 depicts the proposed quadratic droop control characteristic as described in equation (63). As shown in the diagram, a different operating point will map a different slope, which will determine the speed of the system response to the different operating condition.

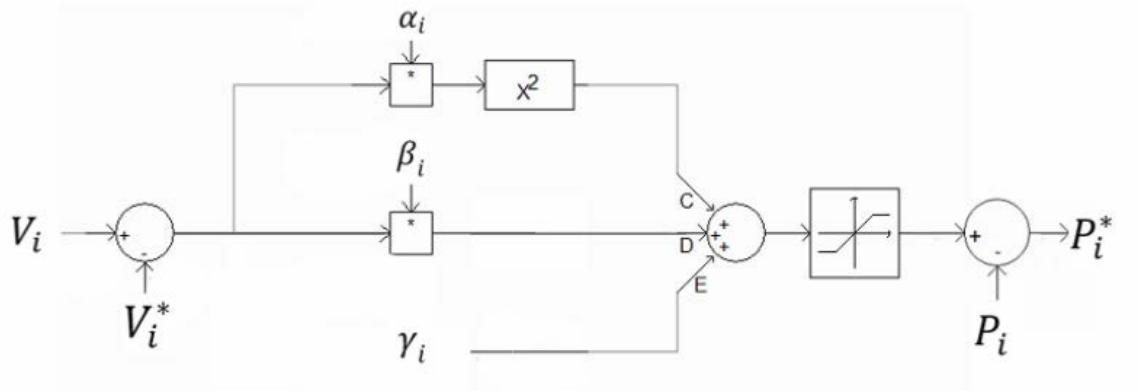

Figure 34. The block diagram of the controller.

Figure 34 depicts the block diagram of the proposed control. The terminal power marginal conditions for each converter can be used to determine the α_i, β_i and γ_i coefficients.

The coefficients of α_i, β_i and γ_i can be derived by several system steady state operating points. The converters at the same dc terminal should have the same droop control function and coefficients, as long as they share the power evenly.

For the converter at different dc terminals, the droop control functions and coefficients can be calculated according to the procedures described above.

5.2 Hybrid AC-MTDC Test System

The hybrid AC-MTDC test system consists of two major ac networks, two wind farms and a five-terminal dc network connecting them. Figure 35 depicts the system layouts.

AC Grid 1 is rated at 230 kV/60Hz, AC Grid 2 is rated at 345 kV/60Hz, and the DC Grid is rated at ±200 kV in bi-polar configurations. All converters utilize MMC structures.

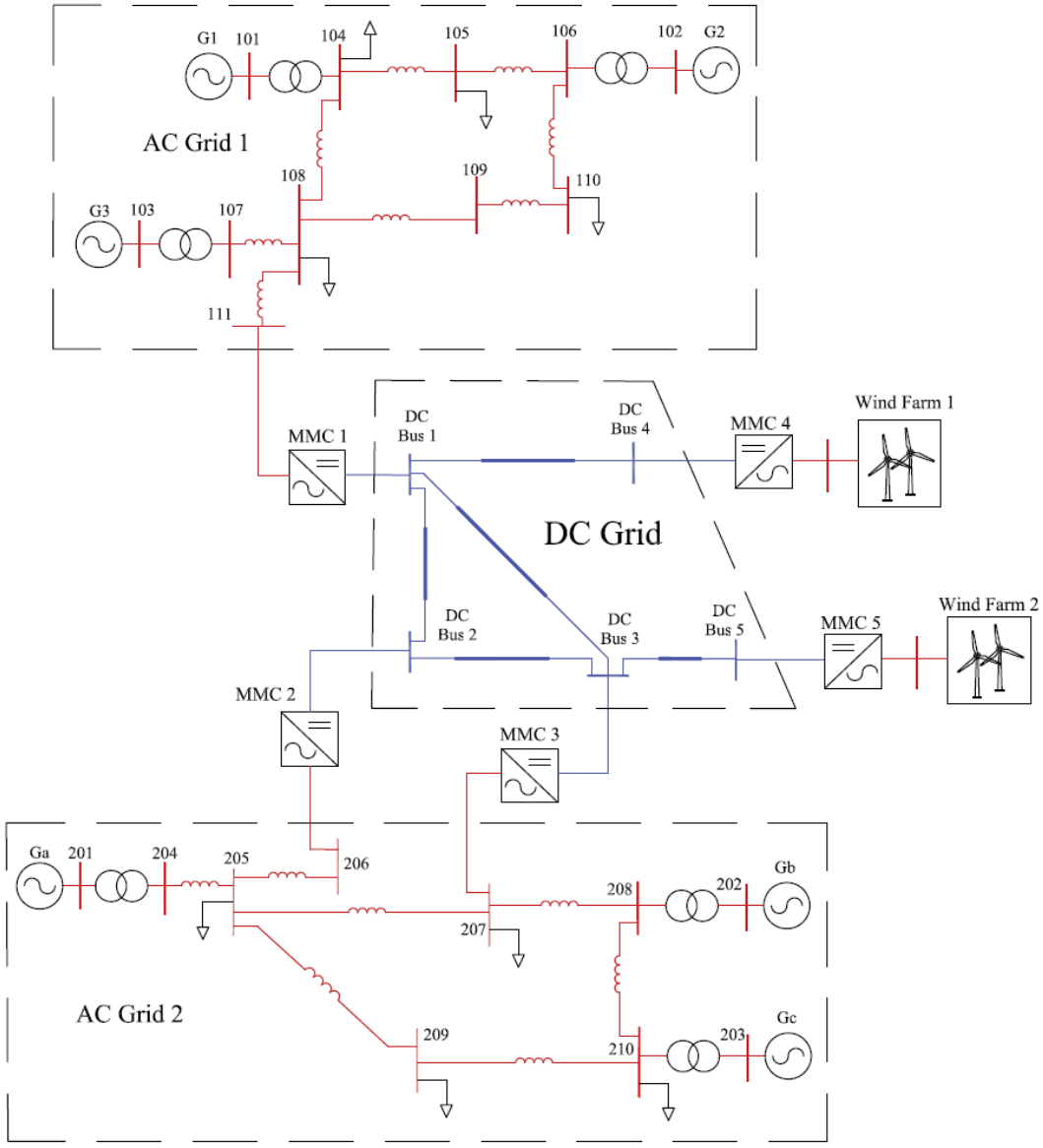

Figure 35 Topology of the five-terminal HVDC system.

AC Grid 1 is connecting the DC Grid via one dc terminal; ac Grid 2 is connecting the DC Grid via two dc terminals. Each wind farm connects to the DC Grid via one dc terminal.

5.2.1 AC Grid 1

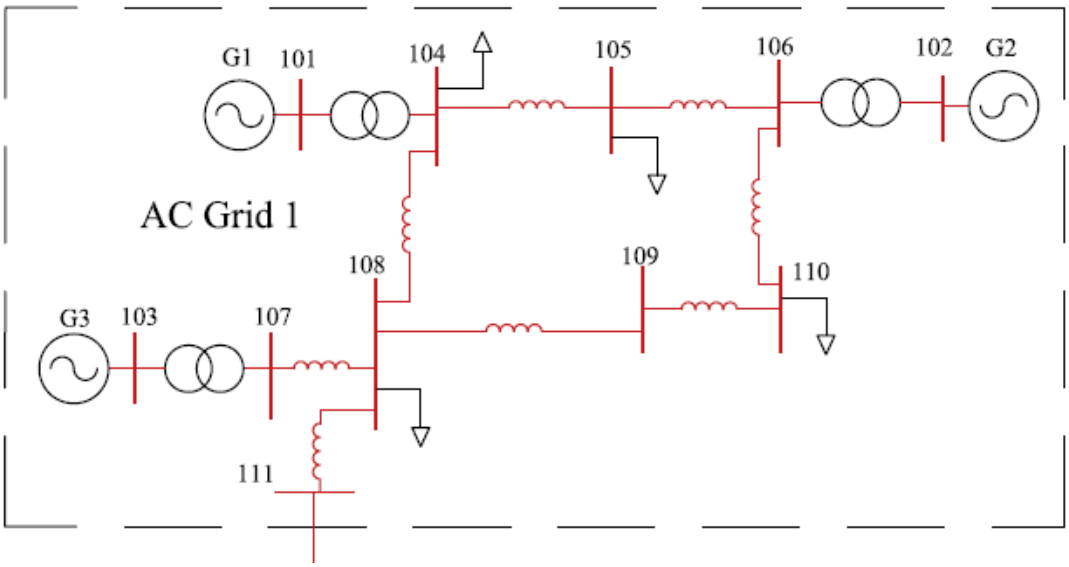

Figure 36 The topology of the ac Grid 1.

Figure 36 shows the topology of the AC Grid 1, rated at 230 kV/60Hz, consisting of three generators and four loads. The bus, generator, load, and transmission line status are described in Table 12, Table 13, Table 14, and Table 15, respectively.

TABLE 12. BUS STATUS IN THE AC GRID 1

Bus Number	Nom (kV)	PU	Voltage	Angle (Deg.)
101	16.5	1.032	17.028	2.98
102	18.00	1.021	18.378	5.6
103	13.8	1.007	13.897	0.0
104	230	1.027	234.2	-2.15
105	230	1.017	233.91	-4.63
106	230	1.033	237.59	2.18
107	230	1.000	230	-4.52
108	230	1.001	230.23	-12.8
109	230	1.006	231.38	-4.75
110	230	0.961	221.03	1.57

TABLE 13. GENERATOR STATUS IN THE AC GRID 1

Generator	Real Power (MW)	Reactive Power (Mvar)	Set Voltage (p.u.)
G1	400	0	1.025
G2	246.7	609.7	1.021
G3	688.9	550.2	1.007

TABLE 14. LOAD STATUS IN THE AC GRID 1

Load	Real Power (MW)	Reactive Power (Mvar)	Set Voltage (p.u.)
104	200	0	1.027
105	200	0	1.017
108	500	0	1.001
110	300	30	0.961

TABLE 15. AC TRANSMISSION LINE STATUS IN THE AC GRID 1

From Bus	To Bus	Length [m]	Resistance [p.u./m]	Inductive Reactance [p.u./m]	Capacitive Reactance [p.u.*m]
104	105	1.0E5	8.5E-8	5.76E-7	6.71E5
105	106	1.0E5	1.19E-7	1.01E-6	6.71E5
104	108	5.0E4	4.2E-6	2.29E-6	2.79E5
106	110	1.0E5	3.9E-7	1.74E-6	2.79E5
107	108	1.0E3	1.06E-7	5.75E-7	3.96E5
108	109	1.0E5	1.06E-7	5.75E-7	3.96E5
109	110	1.0E5	6.38E-8	3.45E-7	2.37E5
108	111	1.0E4	1.06E-7	5.75E-7	3.96E5

In AC Grid 1, the voltage is rated at 230 kV, 100 MVA, and 60 Hz. The zero-sequence resistor is one and half times the positive sequence resistor. The zero-sequence impedance is one and half times the positive sequence impedance. The zero-sequence traveling wave time constant is one and half times the positive-sequence traveling wave time constant.

In short:

Zero Seq. R / positive Seq. R = 1.5

Zero Seq. Z / positive Seq. Z = 1.5

Zero Seq. Trav. Time / positive Seq. Trav. Time = 1.5

5.2.2 AC Grid 2

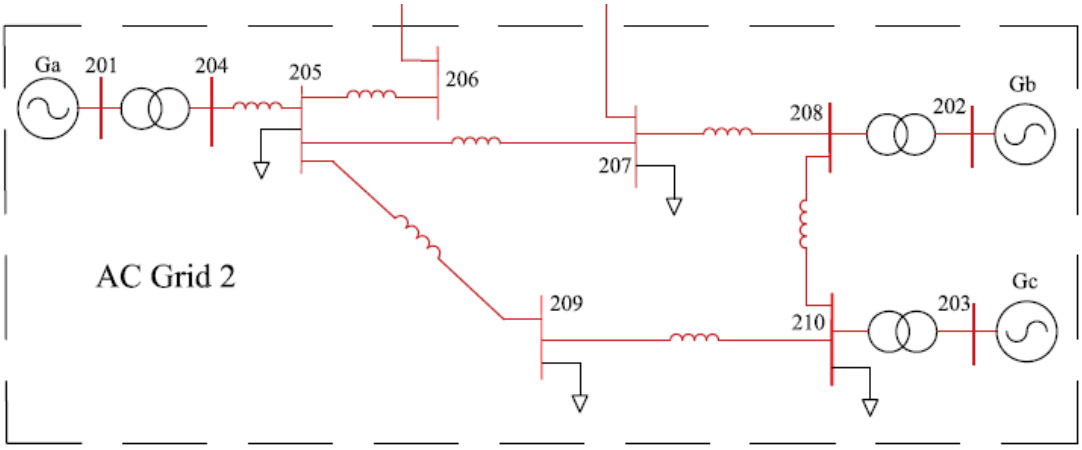

Figure 37 The topology of the ac Grid 2.

Figure 37 shows the transmission network of the ac Grid 1 rated at 230 kV/60Hz, consisting of three generators and four loads. The bus, generator, load, and transmission line status are described in Table 16, Table 17, Table 18, and Table 19, respectively.

TABLE 16. BUS STATUS IN THE AC GRID 2

Bus Number	Nom (kV)	PU	Voltage	Angle (Deg.)
201	16.5	1.04	17.16	0
202	18.00	1.025	18.45	8.97
203	13.8	1.025	14.145	20.45
204	345	1.005	346.725	-1.51
205	345	1.005	346.725	-1.53
206	345	1.001	345.345	-0.07
207	345	1.012	349.14	1.94
208	345	1.024	353.28	10.81
209	345	0.975	336.375	-13.49
210	345	0.994	342.93	-10.46

TABLE 17. GENERATOR STATUS IN THE AC GRID 2

Generator	MW	Mvar	Set Volt (p.u.)
Ga	326.07	122.25	1.04
Gb	300	59.95	1.025
Gc	300	26.4	1.025

TABLE 18. LOAD STATUS IN THE AC GRID 2

Load	MW	Mvar	Set Volt (p.u.)
205	150	0	1.005
207	50	0	1.024
209	400	0	0.975
210	300	0	0.994

TABLE 19. AC TRANSMISSION LINE STATUS IN THE AC GRID 2

From Bus	To Bus	Length [m]	Resistance [pu/m]	Inductive Reactance [pu/m]	Capacitive Reactance [pu*m]
204	205	1.0E3	8.5E-8	5.76E-7	6.71E5
205	206	1.0E3	8.5E-8	5.76E-7	6.71E5
205	207	1.0E5	8.5E-8	5.76E-7	6.71E5
207	208	1.0E5	1.19E-7	1.01E-6	6.71E5
205	209	1.0E5	1.6E-7	8.05E	6.54E5
209	210	1.0E5	5.0E-8	3.4E-7	1.14E6
208	210	1.35E5	3.9E-7	1.74E-6	2.79E5

In ac Grid 2, the voltage is rated at 345 kV, 100 MVA, and 60 Hz. The zero-sequence resistor is one and half times the positive sequence resistor. The zero-sequence impedance

is one and half times the positive sequence impedance. The zero-sequence traveling wave time constant is one and half times the positive-sequence traveling wave time constant.

In short:

Zero Seq. R / positive Seq. R = 1.5

Zero Seq. Z / positive Seq. Z = 1.5

Zero Seq. Trav. Time / positive Seq. Trav. Time = 1.5

5.2.3 DC Grid

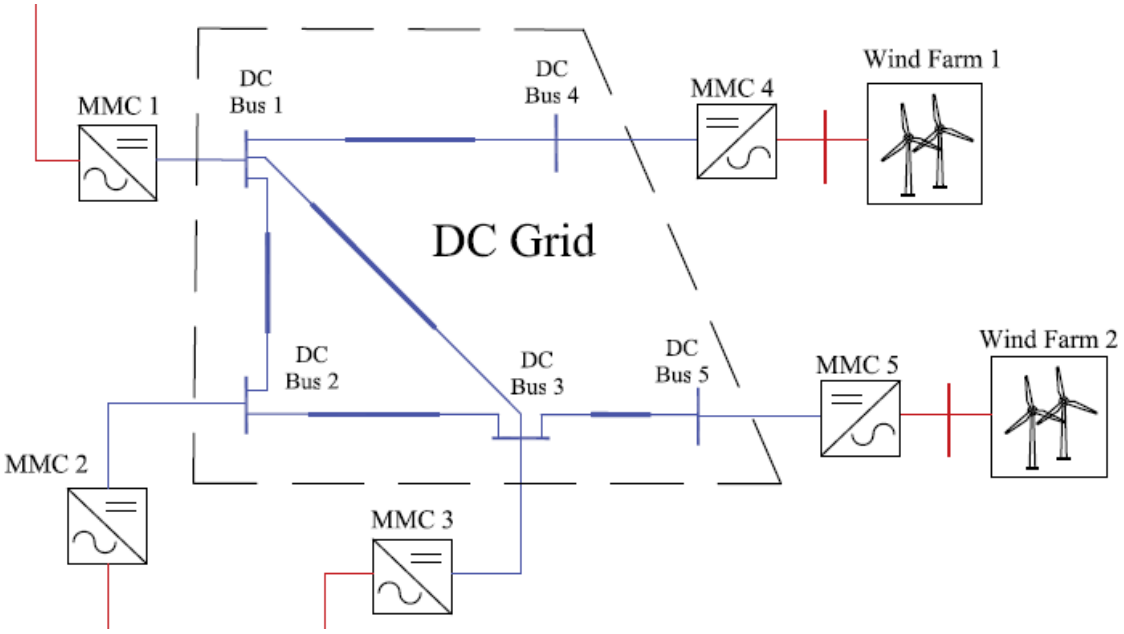

Figure 38 The topology of the dc benchmark model.

In dc benchmark model shown in Figure 38, the rated voltage is ±200 kV dc. The converters are modeled in bipolar configurations. The dc grid data are in accordance with CIGRE B4 MTDC grid test system layout.

Figure 39 depicts the configuration of the bipolar HVDC converter station as used in the benchmark model in this system. Each substation is connected to the ac network

through a delta-wye transformer, where the delta winding is attached to the dc side. Two ac circuit breakers and two dc circuit breakers are installed as shown in the diagram.

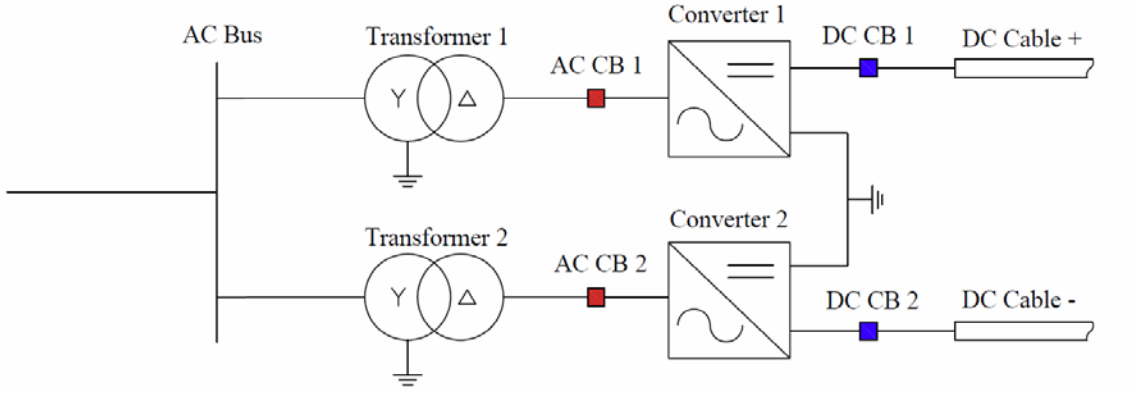

Figure 39 The configuration of the bipolar HVDC converter station as used in the benchmark model.

5.2.4 MMC model

The detailed switching model is time-consuming and infeasible to large-scale multi-terminal dc system simulation according to many semiconductor switches in the high voltage applications. In order to overcome this challenge, the configuration of an Equivalent Circuit Model (ECM) shown in Figure 40 is employed in this simulation [21].

The ECM model consists of two controllable switches, four diodes, and one controlled voltage source. In this simulation study, each MMC converter arm consists of 50 ECM submodules.

Under normal operating condition, the switching status of the proposed ECM is shown in Figure 40. The control switches S1 and S2 are on. All fault-blocking SMs in hybrid MMC can be regarded as HBSMs since they have the same dynamic behaviors. The

operational principles of the hybrid MMC are similar to the HB-MMC. The voltage source in the ECM represents the sum of inserted capacitor voltages.

Under dc-side short-circuit fault condition, all SMs are blocked and the control switches S1 and S2 are off, as shown in Figure 40 (c) and (d). When the arm current is negative, the HB-SMs are bypassed. When the arm current is positive, it charges the capacitors. For the fault-blocking SMs, the arm current always charges the capacitors regardless of the direction of the arm current.

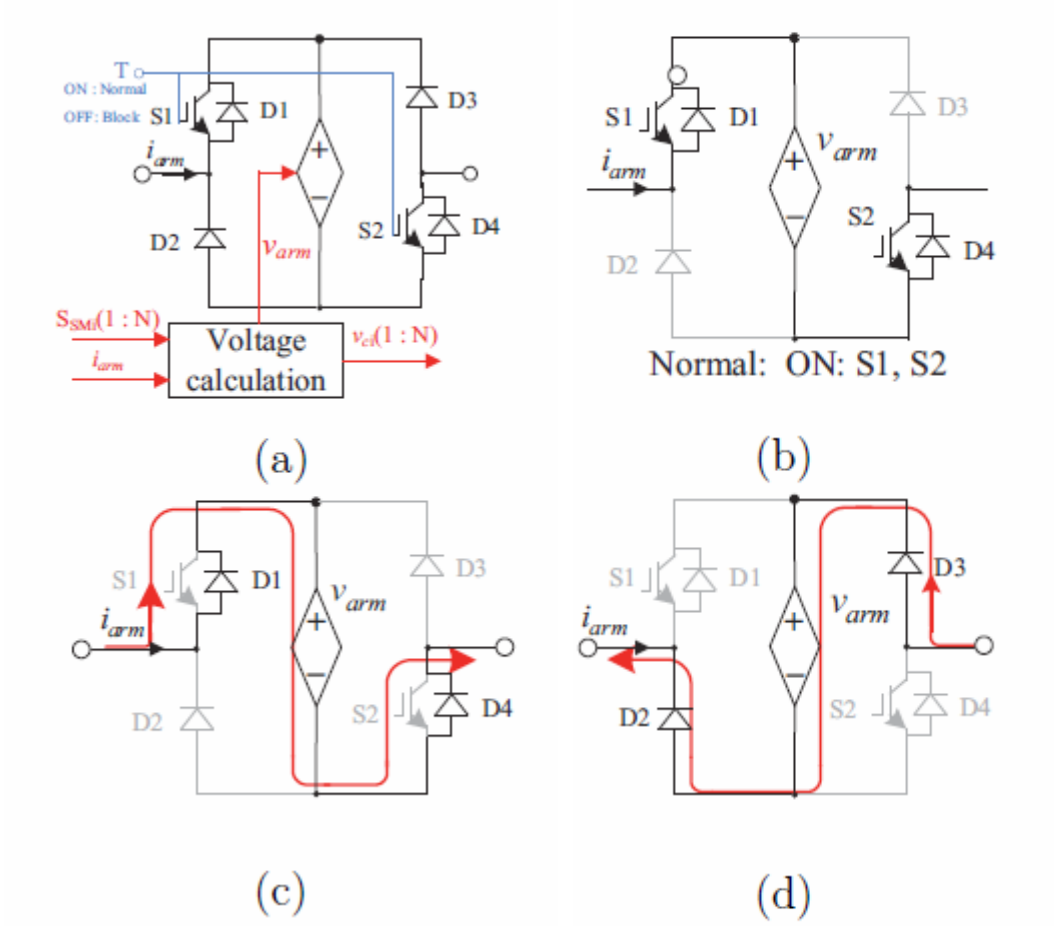

Figure 40 The arm branch of the proposed equivalent circuit model: (a) circuit diagram of ECM, (b) normal operation, (c) and (d) current path under blocking condition [21].

5.3 Droop Control Schemes

As described in Section 5.1, the developed droop control characteristic is not limited by proportional linear relationship.

A linear droop control scheme, a nonlinear scheme (quadratic droop control), and a hybrid linear-nonlinear droop control scheme are proposed, designed in this chapter. The detailed design procedures and parameters are demonstrated.

In the proposed five-terminal HVDC system, the dc terminal 1, 2 and 3 are connected to the ac gird. These three terminals will operate under the droop control characteristic. The dc terminal 4 and 5 are connected to the wind farms, the amount of power produced from these two farms are determined by the wind farms, which are intermittent renewable energy recourses. These two terminals produce uncertainties to the dc grids, and the worst case is an outage of these terminals.

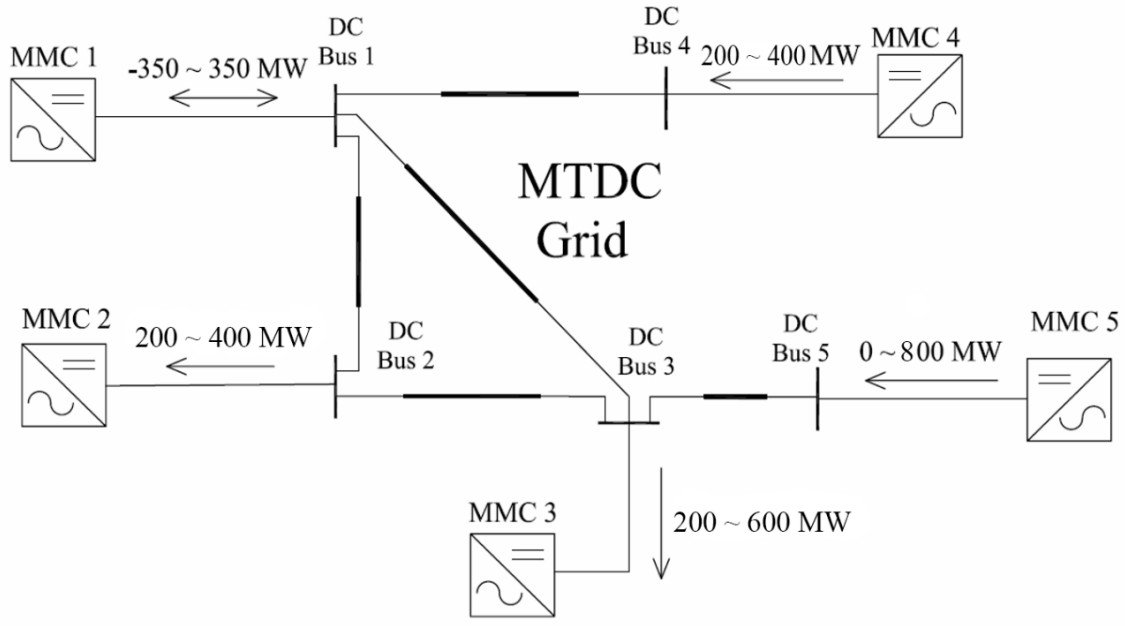

Figure 41 Power constraints at each dc terminal.

The power constraints of each dc terminal are described in Figure 41. The power values described in the diagram are the combination of the two converters at the same terminal, i.e., for each converter, the power constraint will be half of the described value. The dc voltage tolerance on each dc bus is ±10%, i.e., 190 to 210 kV at each positive dc pole and -190 kV to -210 kV at each negative dc pole in the five-terminal HVDC test system.

The design procedures are such:

i. Determine a system reference operating condition. At this operating condition, the wind farms are operated at their standard outputs. In the proposed five-terminal HVDC system, the reference operating condition is described in Table 20.

ii. Determine several steady-state operating conditions. These steady-state conditions are under the system power and voltage constraints.

iii. The droop control will be designed according to these steady state conditions and the reference operating point to meet the system operating requirements.

iv. Hard constraints will be applied to the droop control to ensure the converter is operating within the voltage constraint: ±10%, and power limits as shown in Figure 41.

The MMCs at the same terminal share power evenly, therefore the same terminal MMC must equip the same droop control schemes. It is noticeable that, the converter dc voltage should not be selected as the voltage input measure because the two MMCs at the same terminal will have the same droop control characteristics. The pole to pole voltage is selected as the voltage control measure to map both converters' voltage conditions.

TABLE 20. FIVE TERMINAL SYSTEM REFERENCE OPERATING CONDITION

	Terminal 1	Terminal 2	Terminal 3	Terminal 4	Terminal 5
DC voltage (kV)	±200	±199.71	±199.79	±200.62	±200.94
Power consumed from the dc grid (MW)	151.83*2	148.96*2	198.86*2	-200*2	-300*2

Table 20 describes the system reference operating condition. The positive power value means the terminal is consuming power from the dc grid, and the negative power value means the terminal is providing power to the dc grid.

In a droop control scheme, the voltage level at different dc buses in an MTDC grid directly influences the dc power flow among the terminals. It is worth to notice that unlike in an ac system, where fixed voltage amplitudes (typically around 1.0 p.u.) are preferred, in an MTDC grid, the dc voltage levels cannot be the same through the entire grid. The dc power flow among terminals depends on these voltage differences.

5.3.1 A linear droop control scheme

In order to determine the linear droop control scheme characteristics, a steady state operating condition is determined as shown in Table 21.

At the same dc terminal, the positive and negative pole converter will share the power evenly. Therefore, these two converters should work under the same droop control scheme.

The pole to pole voltage is used to receive terminal voltage conditions from both converters to create feedback controls.

TABLE 21. A STEADY STATE OPERATING CONDITION

	Terminal 1	Terminal 2	Terminal 3	Terminal 4	Terminal 5
DC voltage (kV)	±195	±194.74	±194.93	±195.42	±195.59
Power consumed from the dc grid (MW)	26.24*2	124.69*2	149.74*2	-100*2	-200*2

In this condition, the terminal 1 dc voltage is set to ±195 kV, and the two wind farm terminals are providing 200 MW and 400 MW to the dc grid, respectively. The rest of the system parameters are calculated under the steady state condition in the PSCAD platform.

Therefore, the terminal 2 and terminal 3 droop characteristics are be solved by using the data as shown in Table 22.

TABLE 22. LINEAR DROOP CONTROL CHARACTER POINTS

		Pole to Pole Voltage (kV)	Single MMC Power (MW)
Terminal 1	Reference	400	151.83
	Steady State	390.1	26.25
Terminal 2	Reference	399.42	148.96
	Steady State	389.48	124.69
Terminal 3	Reference	399.58	198.86
	Steady State	389.86	149.74

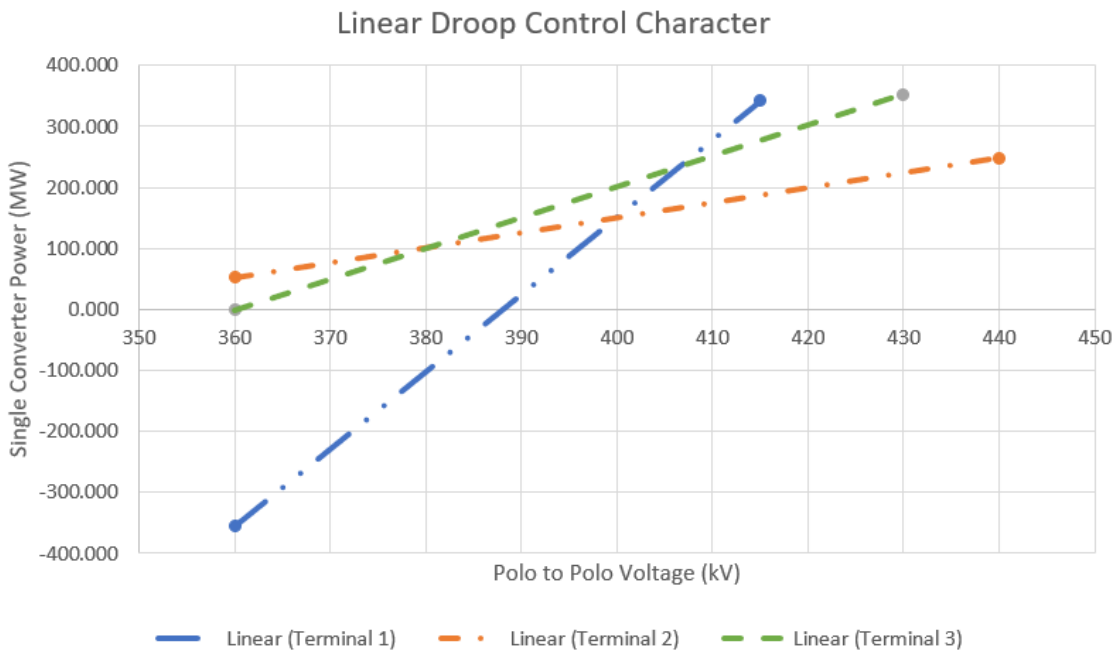

Figure 42 Linear droop control character lines.

Figure 42 depicts the linear droop control character lines derived from the Table 22, and the equation 65 shows the linear droop control equations.

$$\begin{cases} P_1 - 151.83 = 12.685\ (V_1 - 400) \\ P_2 - 148.96 = 2.441\ (V_2 - 399.42) \\ P_3 - 198.86 = 5.054\ (V_3 - 399.58) \end{cases} \tag{65}$$

where the voltage limits are from 360 kV to 440 kV, and the power constraints are illustrated in Figure 41.

5.3.2 A quadratic droop control scheme

In order to illustrate the method as described in Section 5.1, a quadratic relation between the power and voltage are determined.

The improved design method is proposed as follow:

$$P_i - P_i^* = \alpha_i (V_i - V_i^*)^2 + \beta_i (V_i - V_i^*) + \gamma_i \tag{66}$$

where the coefficient α_i is symbol function to fulfill the feedback control.

$$\alpha_i = |\alpha_i| * sgn(V_i - V_i^*) \tag{67}$$

The proposed nonlinear droop control employs the same reference operating condition as described in Table 20 and steady-state condition as depicted in Table 21. An additional set of parameters are designed in this case to calculate the α_i. The character points of the nonlinear droop control, which employs quadratic scheme, are depicted in the Table 23.

At the same dc terminal, the positive and negative pole converter will share the power evenly. Therefore, these two converters should work under the same droop control scheme.

The pole to pole voltage is used to receive terminal voltage conditions from both converters to create feedback controls.

TABLE 23. QUADRATIC DROOP CONTROL CHARACTER POINTS

		Pole to Pole Voltage (kV)	Single MMC Power (MW)	Pole to Pole Voltage (kV)	Single MMC Power (MW)
		V<V*		V>=V*	
Terminal 1	Reference	400	151.83	400.00	151.83
	Steady State	390.1	26.25	409.66	276.18
	Designed Character	396	135	403.76	167.43
Terminal 2	Reference	399.42	148.96	399.42	148.96
	Steady State	389.48	124.69	409.17	174.75
	Designed Character	396	145	402.65	154.44
Terminal 3	Reference	399.58	198.86	399.58	198.86
	Steady State	389.86	149.74	409.79	250.01
	Designed Character	396	190	396.00	209.75

By solving parameters in the three working conditions, the droop control characteristic equations are described in equation (68), (69), and (70).

$$V_1 = \begin{cases} -\sqrt{\frac{P_1 - 151.83}{-1.3117}} + 400, \ when\ P_1 < 151.83 \\ \sqrt{\frac{P_1 - 151.83}{1.3117}} + 400, \ when\ P_1 \geq 151.83 \end{cases} \quad (68)$$

$$P_2 = \begin{cases} -0.2543 * V_2^2 + 203.03V_2 - 40375, \ when\ V_2 < 399.42 \\ 0.2543 * V_2^2 - 203.17V_2 + 40730, \ when\ V_2 \geq 399.42 \end{cases} \quad (69)$$

$$P_3 = \begin{cases} -0.5017 * V_3^2 + 401.07V_3 - 79963, \ when\ V_3 < 399.58 \\ 0.5017 * V_3^2 - 401.26V_3 + 80438, \ when\ V_3 \geq 399.58 \end{cases} \quad (70)$$

where the voltage limits are from 360 kV to 440 kV, and the power constraints are illustrated in Figure 41.

5.3.3 A hybrid linear-nonlinear droop control scheme

It is possible to combine the linear droop control strategy with the nonlinear droop control strategy to fulfill the specific control requirements. A hybrid linear-nonlinear droop control strategy is proposed. In the five-terminal HVDC system, the droop control is applied to the converters connecting the ac grids, i.e., terminals 1, 2, and 3.

The linear droop control is applied to the terminal 1, and the quadratic droop control is applied to terminals 2 and 3.

At the same dc terminal, the positive and negative pole converter will share the power evenly. Therefore, these two converters should work under the same droop control scheme.

The pole to pole voltage is used to receive terminal voltage conditions from both converters to create feedback controls.

TABLE 24. HYBRID LINEAR-NONLINEAR DROOP CONTROL CHARACTER POINTS

		Pole to Pole Voltage (kV)	Single MMC Power (MW)
Terminal 1	Reference	400	151.83
	Steady State	390.1	26.25

		Pole to Pole Voltage (kV)	Single MMC Power (MW)	Pole to Pole Voltage (kV)	Single MMC Power (MW)
		V<V*		V>=V*	
Terminal 2	Reference	399.42	148.96	399.42	148.96
	Steady State	389.48	124.69	409.17	174.75
	Designed Character	396	145	402.65	154.44
Terminal 3	Reference	399.58	198.86	399.58	198.86
	Steady State	389.86	149.74	409.79	250.01
	Designed Character	396	190	396	209.75

According to the Table 24, the droop control character is determined and depicted in equation (71), (72) and (73).

$$V_1 = 0.0783 * P_1 + 388.03 \tag{71}$$

$$P_2 = \begin{cases} -0.2543 * V_2^2 + 203.03V_2 - 40375, \ when\ V_2 < 399.42 \\ 0.2543 * V_2^2 - 203.17V_2 + 40730, \ when\ V_2 \geq 399.42 \end{cases} \tag{72}$$

$$P_3 = \begin{cases} -0.5017 * V_3^2 + 401.07V_3 - 79963, \ when\ V_3 < 399.58 \\ 0.5017 * V_3^2 - 401.26V_3 + 80438, \ when\ V_3 \geq 399.58 \end{cases} \tag{73}$$

where the voltage limits are from 360 kV to 440 kV, and the power constraints are illustrated in Figure 41.

5.4 Simulation Studies

Simulations have been performed in the PSCAD/EMTDC platform. A steady-state operation test and a wind farm outage operation test are proposed to illustrate the developed droop control method. Both tests are conducted on the five-terminal HVDC system as described in section 5.3.

The linear droop control (described in 5.3.1), the quadratic droop control (described in 5.3.2) and the hybrid linear-nonlinear droop control (described in 5.3.3) strategies are examined.

5.4.1 Reference operating condition test

In the reference operating condition test, all the three control schemes apply to the system works at the reference operating condition as described in Table 20, i.e., terminal 4 and 5 are producing 200 MW and 300 MW constant power to the dc grid.

It is noticeable that, in the quadratic droop control scheme, when the system work at the reference operating condition, the voltage in the quadratic droop control scheme is not tightly constrained but will oscillate within a small margin.

Figure 43, Figure 44 and Figure 45 illustrate terminal 1, 2 and 3 pole to pole voltages the system, applied the linear droop control, the quadratic droop control and the hybrid droop control, respectively. The system works in the reference operating condition.

Figure 46, Figure 47, and Figure 48 illustrate terminals 1, 2 and 3 power received from the dc grid when the system, applied the linear droop control, the quadratic droop control and the hybrid droop control, respectively, works at the reference operating condition.

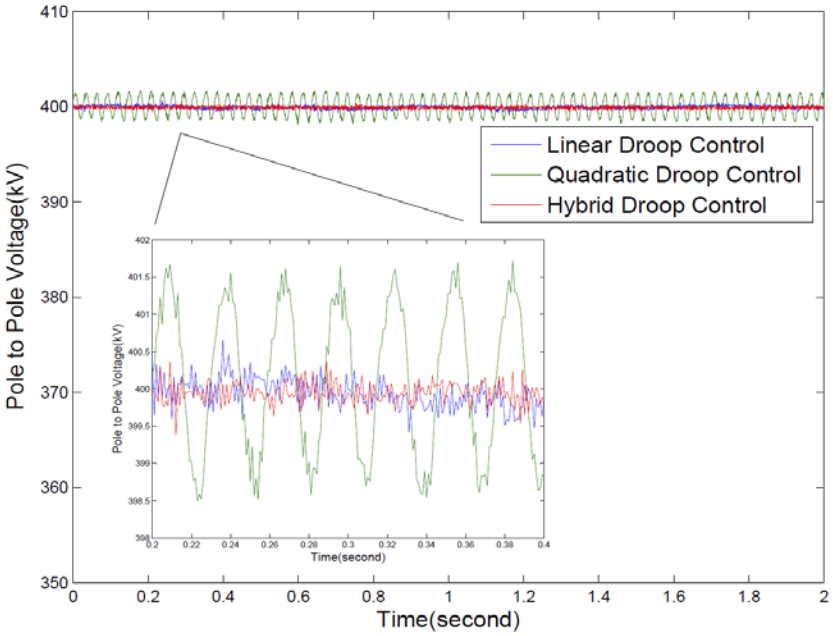

Figure 43 Reference operating condition: pole to pole voltage at terminal 1.

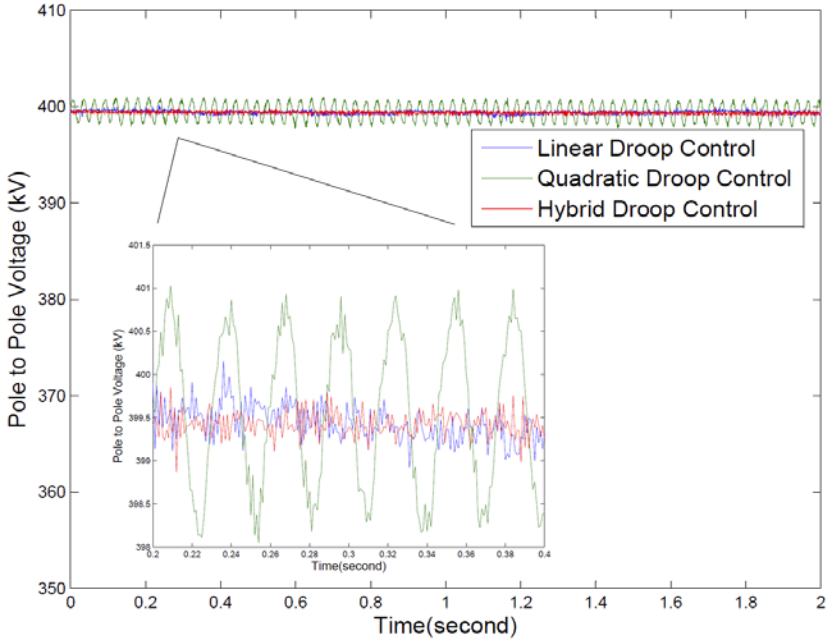

Figure 44 Reference operating condition: pole to pole voltage at terminal 2.

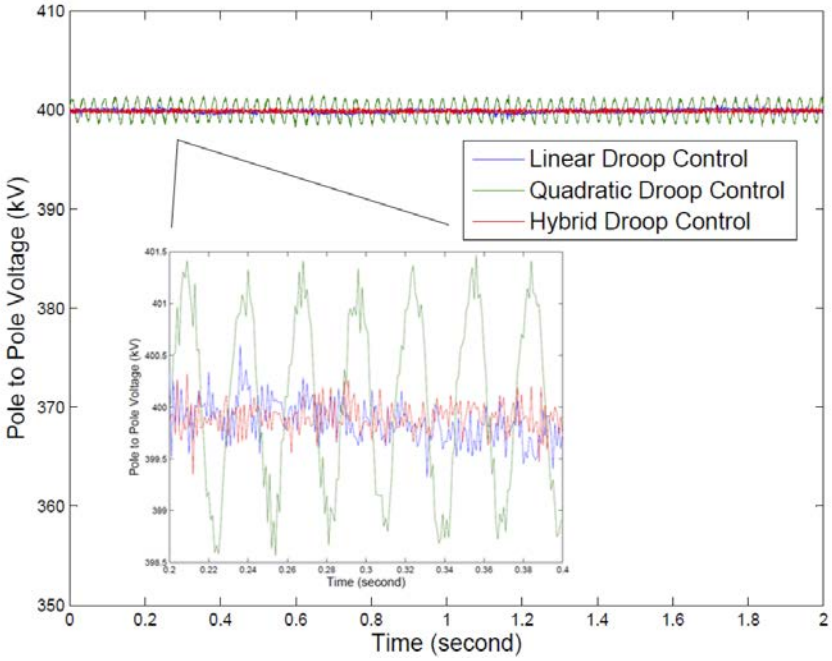

Figure 45 Reference operating condition: pole to pole voltage at terminal 3.

Figure 43, Figure 44 and Figure 45 depict the pole to pole voltages at terminals 1, 2 and 3. According to the simulation results, the terminal voltages of the system with quadratic droop control schemes oscillate within a small margin due to the control scheme. The voltages of the system with linear droop control and the system with hybrid droop control vibrates within 2 kV (0.5%).

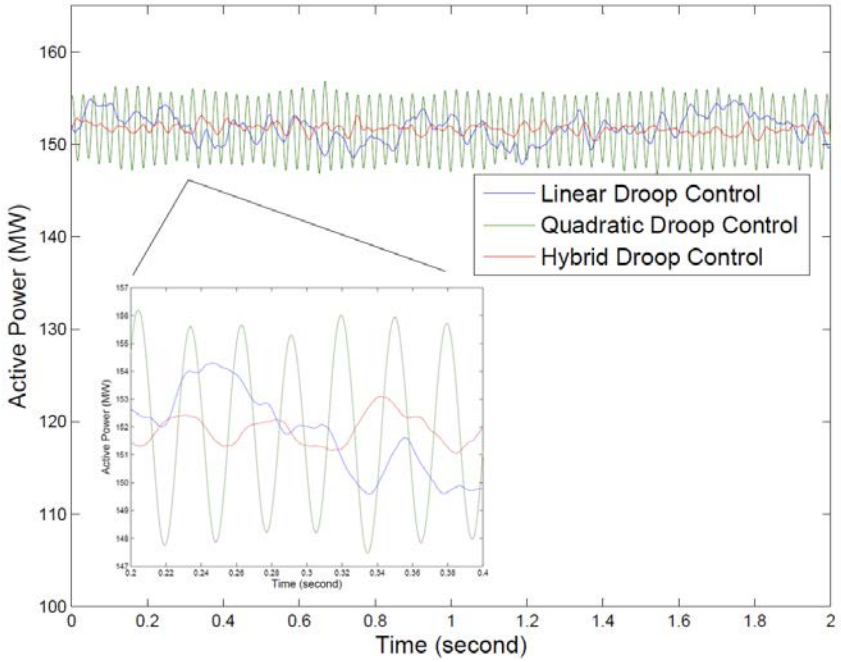

Figure 46 Reference operating condition: active power consumption at terminal 1.

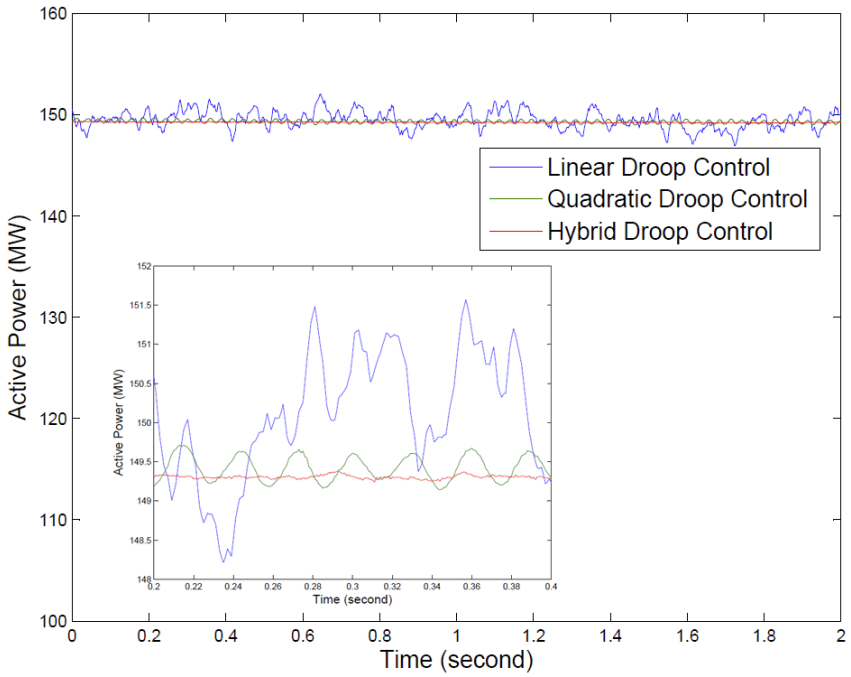

Figure 47 Reference operating condition: active power consumption at terminal 2.

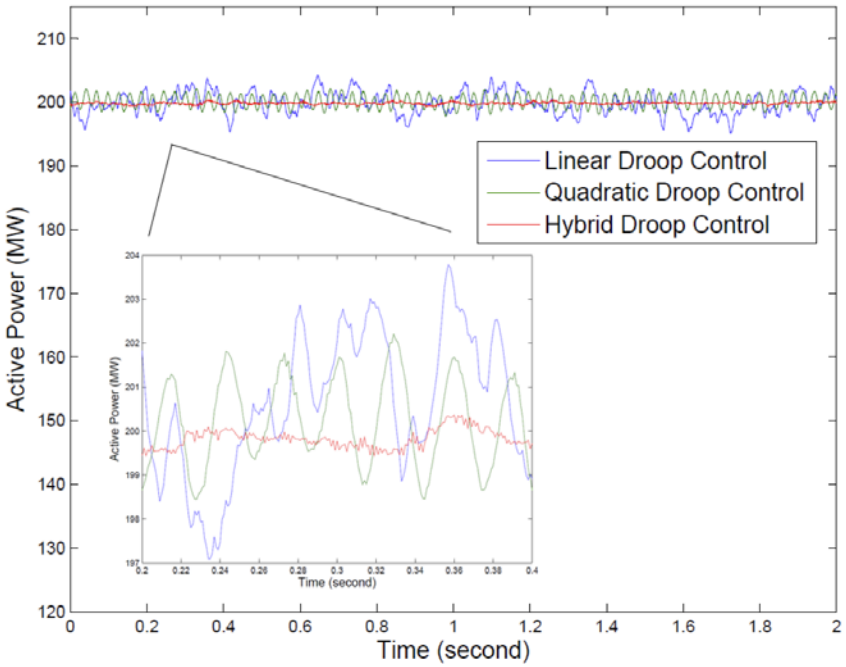

Figure 48 Reference operating condition: active power consumption at terminal 3.

Figure 46, Figure 47, and Figure 48 illustrate terminal 1, 2 and 3 powers received from the dc grid when the system, applied the linear droop control, the quadratic droop control and the hybrid droop control, respectively, works at the reference operating condition. According to the simulation results, the most stable control scheme is the hybrid droop control scheme. The linear droop control has the largest vibration.

As shown in the diagrams, rather than controlling the voltage and power to be a fixed value, all the three droop control schemes regulate the voltage and power within a certain margin.

5.4.2 Wind farm outage operation test

In the wind farm outage operation test, the system will operate independently with the three droop control schemes. Terminal 4 produces 100 MW power constantly, and terminal 5 initially supports 400 MW power to the dc grid and outage at 0.5 s. The power output of these two terminals is shown in Figure 49.

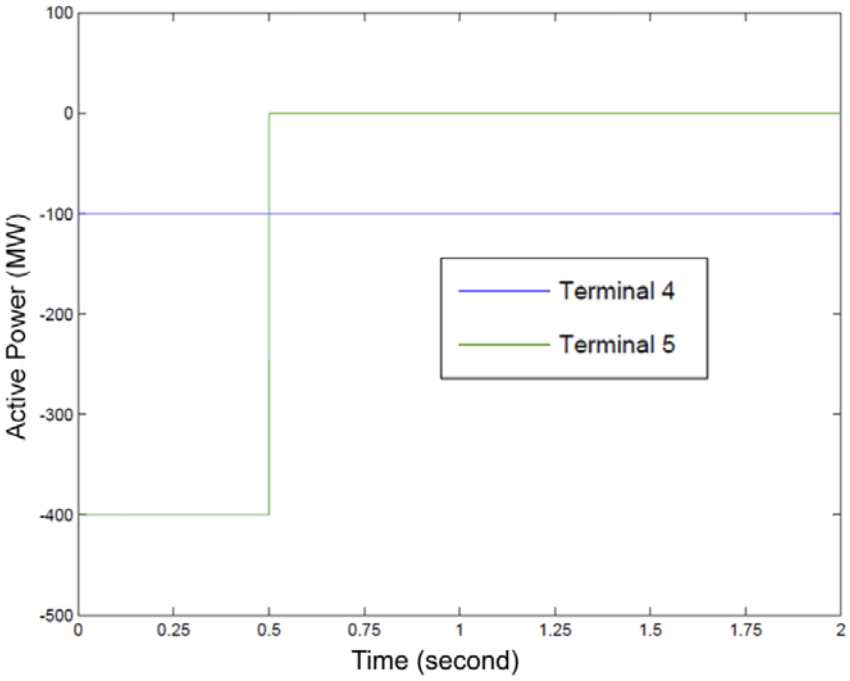

Figure 49 Wind farm outage operation: active power consumption at wind farm terminals: terminal 4 and terminal 5.

The power responses and voltage responses of the to the wind farm outage condition are shown in Figure 50 and Figure 51 when the linear droop control is employed.

The power responses and voltage responses of the to the wind farm outage condition are shown in Figure 52 and Figure 53 when the quadratic droop control is employed.

The power responses and voltage responses of the to the wind farm outage condition are shown in Figure 54 and Figure 55 when the hybrid droop control is employed.

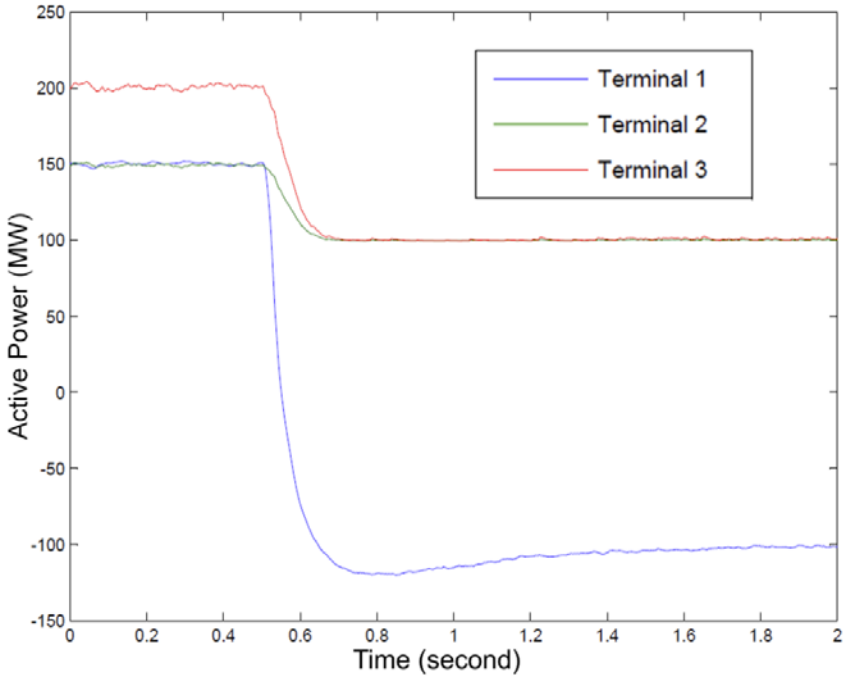

Figure 50 Active power consumption at terminals 1, 2 and 3 at wind farm outage condition: linear droop control.

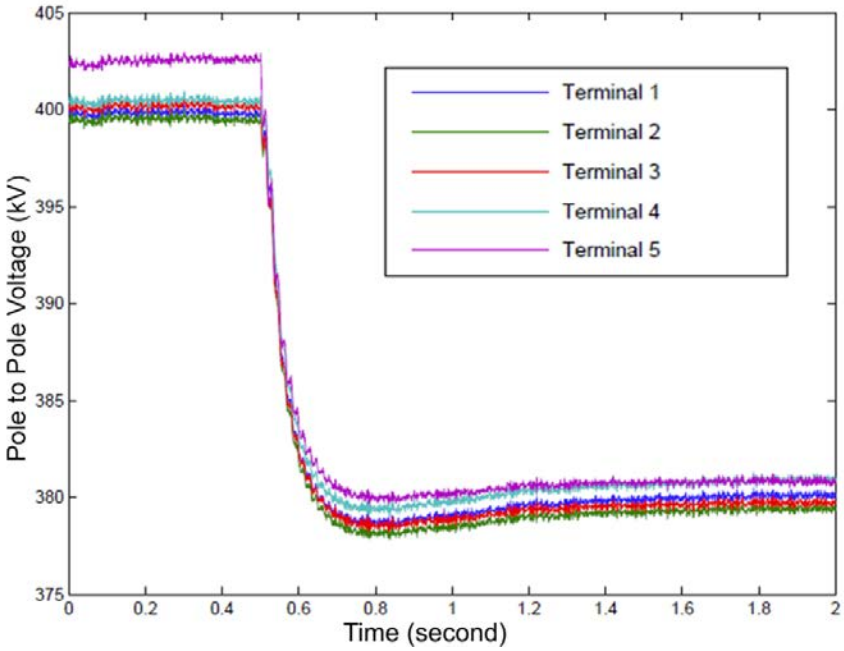

Figure 51 Pole to pole voltage at each terminal at wind farm outage condition: linear droop control.

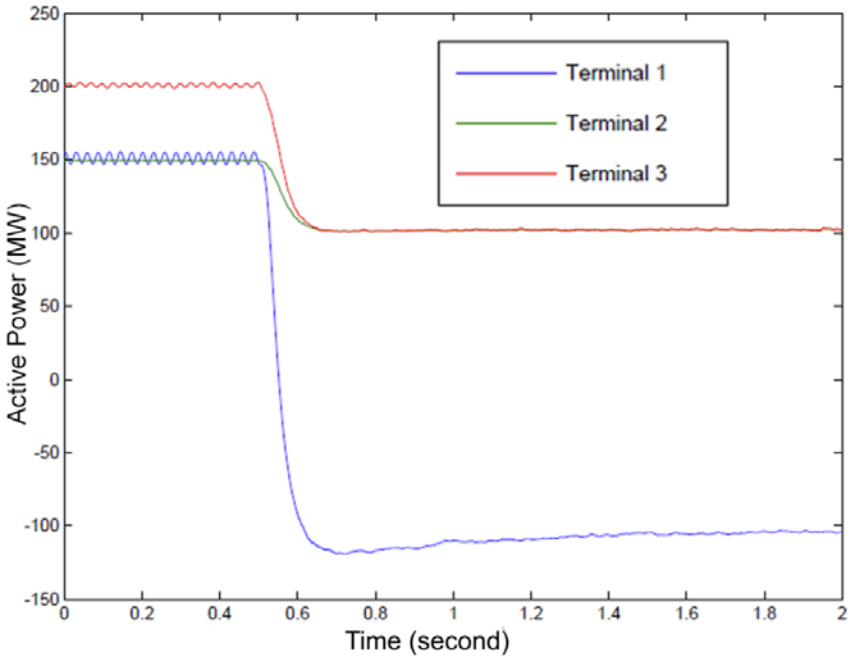

Figure 52 Active power consumption at terminal 1, 2 and 3 at wind farm outage condition: quadratic droop control.

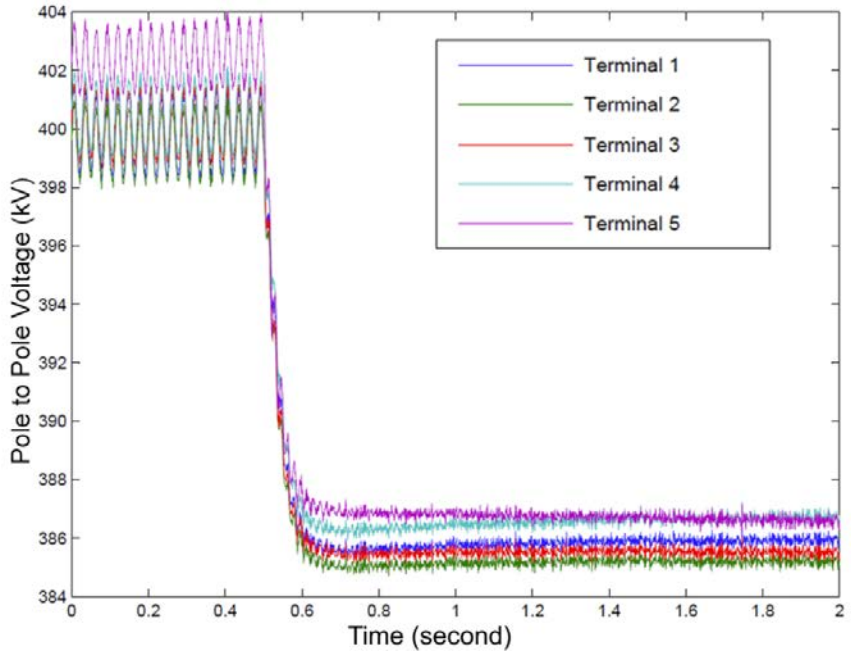

Figure 53 Pole to pole voltage at each terminal at wind farm outage condition: quadratic droop control.

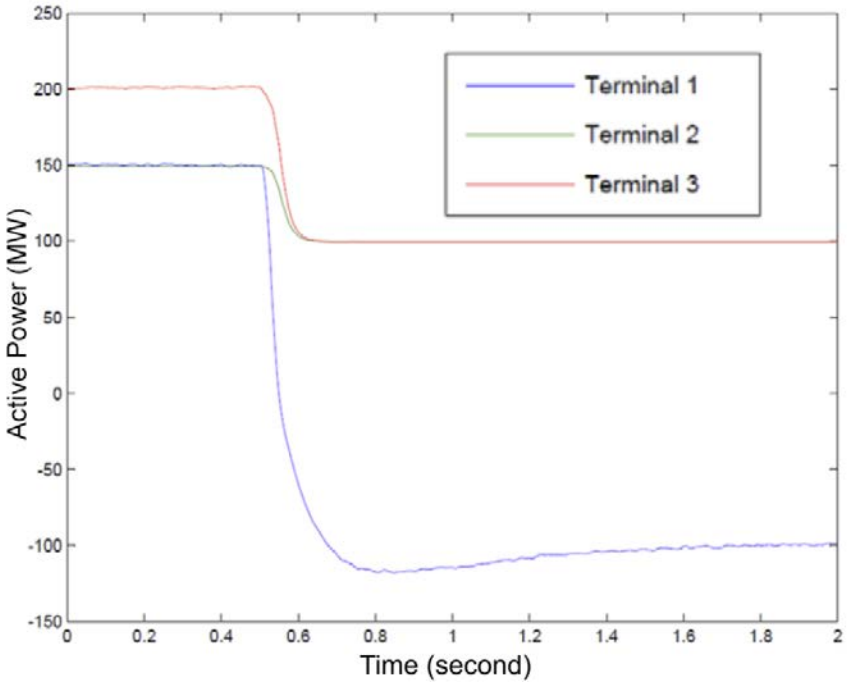

Figure 54 Active power consumption at terminals 1, 2 and 3 at wind farm outage condition: hybrid droop control.

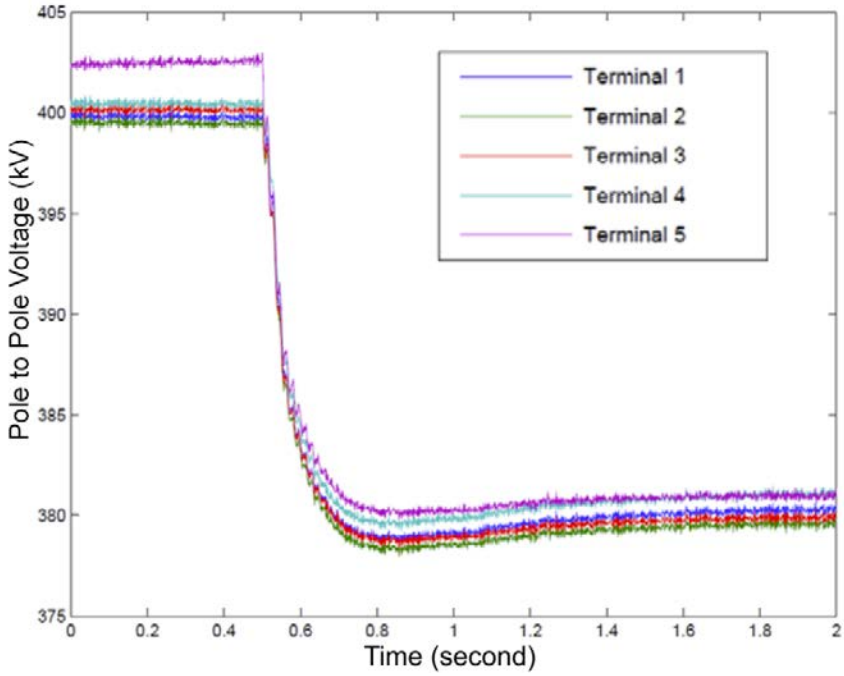

Figure 55 Pole to pole voltage at each terminal at wind farm outage condition: hybrid droop control.

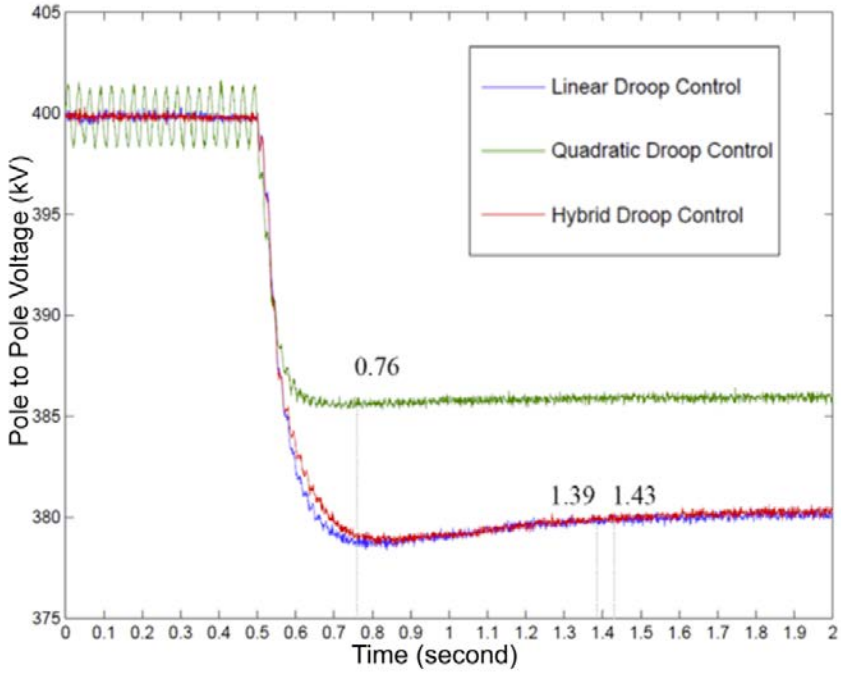

Figure 56 Comparison of the pole to pole voltage at terminal 1 among three scenarios at wind farm outage condition.

Figure 56 shows the comparison of the dc voltages at terminal 1 for the system with the three droop control schemes. The contingency starts at 0.5 s. In the scenario with linear, quadratic and hybrid droop control, the dc voltage recovers at 1.39 s, 0.76 s and 1.43 s.

The dc voltage transient time durations of the linear, quadratic and hybrid droop control are 0.69 s, 0.37 s and 0.71 s, respectively.

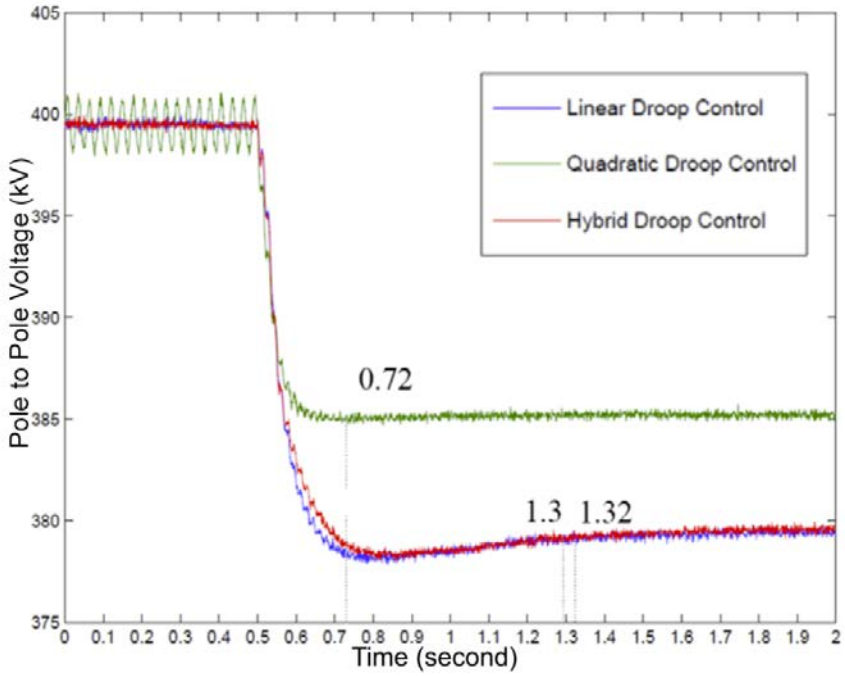

Figure 57 Comparison of the pole to pole voltage at terminal 2 among three scenarios at wind farm outage condition.

Figure 57 shows the comparison of the dc voltages at terminal 1 for the system with the three droop control schemes. The contingency starts at 0.5 s. In the scenario with linear, quadratic and hybrid droop control, the dc voltage recovers at 1.3 s, 0.72 s and 1.32 s.

The dc voltage transient time durations of the linear, quadratic and hybrid droop control are 0.8 s, 0.2 s and 0.82 s, respectively.

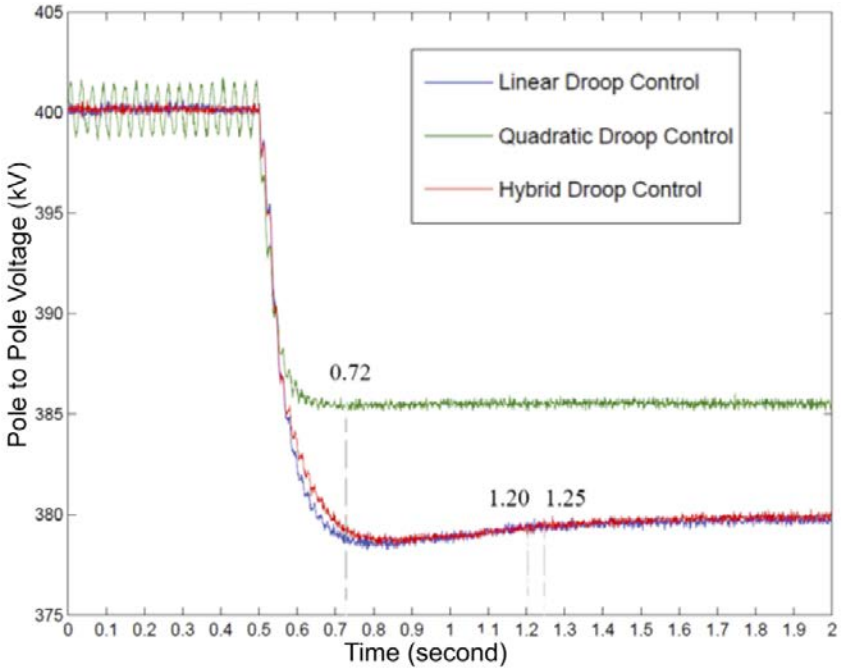

Figure 58 Comparison of the pole to pole voltage at terminal 3 among three scenarios at wind farm outage condition.

Figure 58 shows the comparison of the dc voltages at terminal 1 for the system with the three droop control schemes. The contingency starts at 0.5 s. In the system with linear, quadratic and hybrid droop control, the dc voltage recovers at 1.2 s, 0.72 s and 1.25 s.

The dc voltage transient time durations of the linear, quadratic and hybrid droop control are 0.7 s, 0.22 s and 0.75 s, respectively.

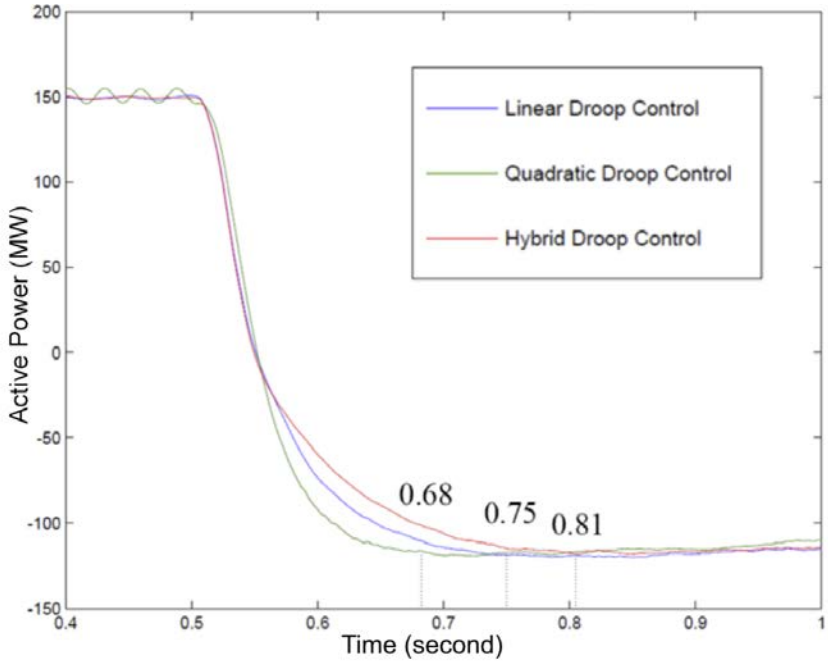

Figure 59 Comparison of the active power at terminal 1 among three scenarios at wind farm outage condition.

Figure 59 shows the comparison of the dc powers at terminal 1 among the three scenarios. The contingency starts at 0.5 s. In the system with linear, quadratic and hybrid droop control, the dc voltage recovers at 0.75 s, 0.68 s and 0.81 s.

The dc voltage transient time durations of the linear, quadratic and hybrid droop control are 0.25 s, 0.18 s and 0.31 s, respectively.

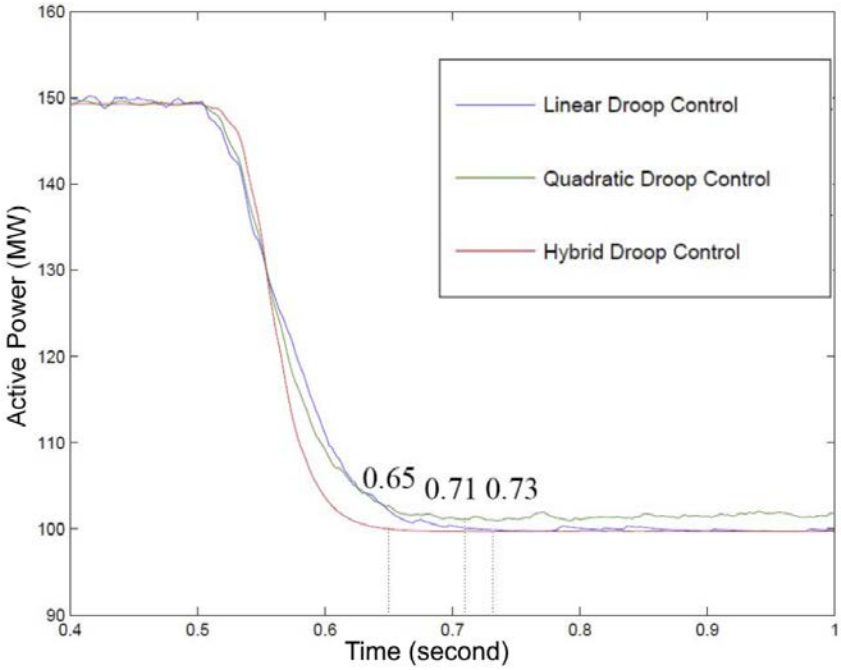

Figure 60 Comparison of the active power at terminal 2 among three scenarios at wind farm outage condition.

Figure 60 shows the comparison of the dc powers at terminal 1 among the three scenarios. The contingency starts at 0.5 s. In the system with linear, quadratic and hybrid droop control, the dc voltage recovers at 0.73 s, 0.71 s and 0.65 s.

The dc voltage transient time durations of the linear, quadratic and hybrid droop control are 0.23 s, 0.21 s and 0.15 s, respectively.

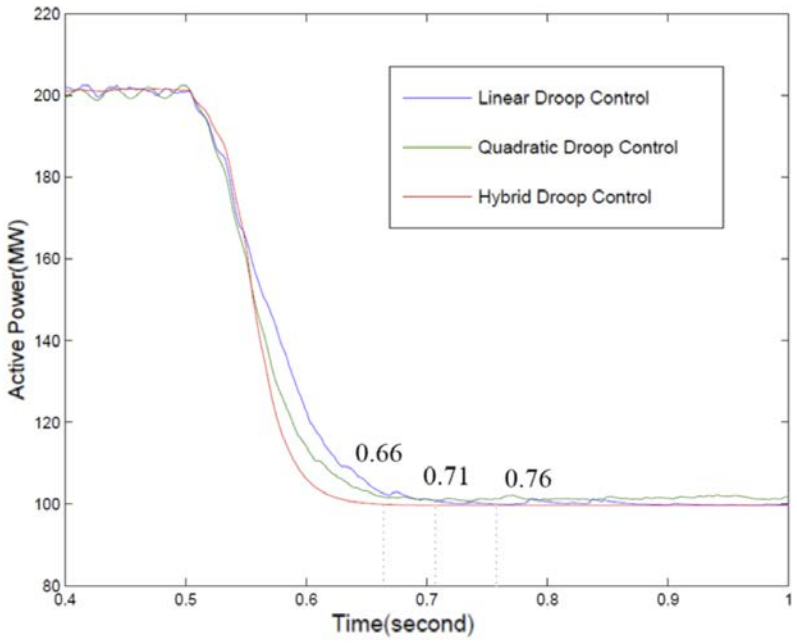

Figure 61 Comparison of the active power at terminal 3 among three scenarios at wind farm outage condition.

Figure 61 shows the comparison of the dc powers at terminal 3 among the three scenarios. The contingency starts at 0.5 s. In the system with linear, quadratic and hybrid droop control, the dc voltage recovers at 0.76 s, 0.71 s and 0.66 s.

The dc voltage transient time durations of the linear, quadratic and hybrid droop control are 0.26 s, 0.21 s and 0.16 s, respectively.

TABLE 25. DC VOLTAGE TRANSIENT DURATION IN DIFFERENT DROOP CONTROL SCHEMES

DC Voltage Transient Duration (second)	Droop Control Schemes		
	Linear	Quadratic	Hybrid
Terminal 1	0.69	0.37	0.71
Terminal 2	0.80	0.20	0.82
Terminal 3	0.70	0.22	0.75
Average	0.73	0.26	0.76

Table 25 illustrates the dc voltage transient duration in the all three scenarios. As shown in the table, the quadratic droop control scheme has the shortest transient duration. The linear and hybrid droop control schemes have longer and similar transient duration.

The quadratic droop control regulates the voltage with a larger margin at the reference operating condition and regulates the voltage with a smaller margin at the wind farm outage condition. The more mismatch power produced, the faster voltage regulation will be made by the quadratic droop control. The operation voltage margin at the mismatch condition is smaller than the reference operating condition in the quadratic droop control.

The conclusion can be drawn that the terminal voltages in the quadratic droop control scheme have the fastest dynamic responses. Compared to the linear droop control scheme, the average voltage transient duration for the quadratic droop control scheme receded by 64.4%.

TABLE 26. ACTIVE POWER TRANSIENT DURATION IN DIFFERENT DROOP CONTROL SCHEMES

Active Power Transient Duration (second)	Droop Control Strategy		
	Linear	Quadratic	Hybrid
Terminal 1	0.25	0.18	0.31
Terminal 2	0.23	0.21	0.15
Terminal 3	0.26	0.21	0.16
Average	0.25	0.20	0.21

Table 26 illustrates the active power transient duration in the all three scenarios. As shown in the table, the average active power transient durations among the three scenarios are similar. The quadratic droop control scheme has a slightly shorter duration than the other two.

However, it is noticeable that, in the hybrid linear-nonlinear droop control scheme, linear droop controlled terminal 1 has a much longer power transient duration than the quadratic droop controlled terminal 2 and terminal 3. In the hybrid controlled scheme, at the quadratic droop controlled terminal 2 and terminal 3, the active power transient time is smaller than the time in linear and quadratic control.

As shown in Figure 59, Figure 60, and Figure 61, in the hybrid droop control scheme, the non-linear droop controlled terminal power is more stable than the linear droop controlled terminal.

The conclusion can be drawn that the average active power transient duration among

the three scenarios are similar. In this hybrid droop control scheme, the nonlinear droop controlled buses respond faster than the linear droop control bus and have a better dynamic performance.

According to the simulation results in this chapter, several conclusions can be made:

1) The quadratic droop control scheme has the fastest dc voltage dynamic response among the three droop control schemes. Compared to the linear droop control scheme, the average voltage transient time duration for the quadratic droop control scheme reduced by 64.4%.
2) The average active power transient time duration among the three droop control schemes are similar. In the proposed hybrid droop control scheme, the nonlinear droop controlled buses respond faster than the linear droop control bus and have a better dynamic performance.
3) Different droop control schemes will result in different system dynamic responses. It is possible to design the droop control scheme according to the specific system operation requirements.

CHAPTER 6

CONTRIBUTIONS AND FUTURE WORKS

The dissertation proposes two control strategies for the HVDC system.

1. Power oscillation control strategy for the embedded HVDC system.

The power oscillation control strategy includes two control schemes:

1) A novel power oscillation control scheme for the embedded HVDC system using the frequencies at the converter terminals to improve the system dynamic performance and damp ac power oscillations.
2) A coordinate power oscillation control scheme considering the signal transmission latency is proposed to reduce the influence from the signal communication delay between terminals.

The control schemes have been verified in a long-distance paralleled AC-HVDC transmission test system in the PSCAD/EMTDC platform.

2. Nonlinear voltage droop control strategy for the MTDC system.

Three droop control schemes are designed according to the proposed nonlinear voltage droop control design procedures.

1) A linear droop control scheme.
2) A quadratic droop control scheme for a fast dc voltage regulation.
3) A hybrid linear-nonlinear droop control scheme to reduce power regulation time at specific dc terminals.

All the three control schemes are tested in a hybrid AC-MTDC system in the PSCAD/EMTDC platform. The hybrid AC-MTDC test system, which is designed and

proposed in this article, consists of two ac grid, two wind farms and a five-terminal HVDC system connecting them.

It is a world that the power grids are being urged to increase the capacity of their existing infrastructure efficiently, especially when renewable energy resources start to play a significant role in power generations. The HVDC system has been helping with this goal for decades.

For the future work, it is important to further develop the droop control scheme for the MTDC system, according to the system operation and dynamic requirements. It is desirable to coordinate the nonlinear droop control with the converters' dc fault current blocking functions. It is also possible to combine the proposed nonlinear voltage droop control strategy with considering the ac system conditions to improve the overall system dynamic performance.

REFERENCES

[1] R. Rudervall, J. Charpentier and R. Sharma, "High Voltage Direct Current (HVDC)Transmission Systems," *Energy Week,* pp. 1-17, 7-8 March 2000.

[2] M. Guarnieri, "The Alternating Evolution of DC Power Transmission [Historical]," *IEEE Industrial Electronics Magazine,* vol. 7, no. 3, pp. 60-63, 2013.

[3] J. Paulinder, Operation and control of HVDC links embedded in AC system, Goteborg: Thesis for the degree of licentiate of engineering, Chalmers University of Technology, 2003.

[4] G. Asplund, K. Eriksson and K. Svensson, "HVDC Light – DC transmission based on voltage sourced converters," *ABB Review,* pp. 4-9, 1 1998.

[5] N. Flourentzou, V. G. Agelidis and G. D. Demetriades, "VSC-Based HVDC Power Transmission Systems: An Overview," *IEEE Transactions on Power Electronics,* vol. 24, no. 3, pp. 592-602, 2009.

[6] J. Arrillaga, Y. H. Liu, N. R. Watson and N. J. Murray, Self-Commutating Converters for High Power Applications, John Wiley and Sons, 2009.

[7] L. Zhang, Y. Zou, J. Yu, J. Qin, V. Vittal, G. Karady, D. Shi and Z. Wang, "Modeling, Control, and Protection of Modular Multilevel Converter-based Multi-terminal HVDC Systems: A Review," *CSEE Journal of Power and Energy Systems.*

[8] "List of HVDC projects," [Online]. Available: https://en.wikipedia.org/wiki/List_of_HVDC_projects. [Accessed 15 10 2017].

[9] P. Kundur, Power system stability and control, N. J. Balu and M. G. Lauby, Eds., New York: McGraw-Hill, 1994.

[10] "1204-1997 - IEEE Guide for Planning DC Links Terminating at AC Locations Having Low Short-Circuit Capacities," in *Tech. Rep.*, 1997, pp. 1 - 216.

[11] C. V. Thio, J. B. Davies and K. L. Kent, "Commutation failures in HVDC transmission systems," *IEEE Transactions on Power Delivery* , vol. 11, no. 2, pp. 946 - 957, 1996.

[12] "Quebec - New England: The first large scale multiterminal HVDC transmission in the world to be upgraded.," [Online]. Available: http://new.abb.com/systems/hvdc/references/quebec-new-england.

[13] V. Billon, J. Taisne, V. Arcidiacono and F. Mazzoldi, "The Corsican tapping: from design to commissioning tests of the third terminal of the Sardinia-Corsica-Italy HVDC," *IEEE Trans. Power Del.*, vol. 4, no. 1, pp. 794-799, 1989.

[14] K. R. P. Rodriguez, "Multi-terminal DC grids: challenges and prospects," *Journal of Modern Power Systems and Clean Energy*, vol. 5, no. 4, pp. 515-523, 2017.

[15] J. Yu and G. Karady, "VSC-HVDC dynamic performance enhancement by embedding power oscillation control," in *North American Power Symposium (NAPS)*, Champaign, IL, 2012.

[16] J. Yu, L. Gu and G. Karady, "Applications of embedded HVDC in power system transmission," in *Power Engineering and Automation Conference (PEAM), IEEE*, Wuhan, 2012.

[17] J. Yu, Influence of Embedded HVDC Transmission on AC Network Performance, Tempe, AZ: ARIZONA STATE UNIVERSITY, 2013.

[18] J. Arrillaga, Y. Liu and N. Watson., Flexible power transmission : the HVDC options, Hoboken, NJ: John Wiley, 2007.

[19] J. Rodriguez, S. Bernet, P. K. Steimer and I. E. Lizama, "A Survey on Neutral-Point-Clamped Inverters," *IEEE Transactions on Industrial Electronics*, vol. 57, no. 7, pp. 2219 - 2230, 2009.

[20] Martinez-Velasco, Simulation of Transients for VSC-HVDC Transmission Systems Based on Modular Multilevel Converters, Wiley-IEEE Press, 2014.

[21] L. Zhang, J. Qin, D. Shi and Z. Wang, "Efficient modeling of hybrid MMCs for HVDC systems," in *2017 IEEE Energy Conversion Congress and Exposition (ECCE)*, Cincinnati, OH, USA, 2017.

[22] S. Debnath, J. Qin, B. Bahrani, M. Saeedifard and P. Barbosa, "Operation, control, and applications of the module multilevel converter: A review," *IEEE Trans. Power Electron.*, vol. 30, no. 1, pp. 37-53, 2015.

[23] A. Nami, J. Liang, F. Dijkhuizen and G. Demetriades, "Modular multilevel converters for HVDC applications: Review on converter cells and functionalities," *IEEE Trans. Power Electron.*, vol. 30, no. 1, pp. 18-36, 2015.

[24] J. Qin, M. Saeedifard, A. Rockhill and R. Zhou, "Hybrid design of modular multilevel converters for HVDC systems based on various submodule circuits," *IEEE Trans. Power Del.*, vol. 30, no. 1, pp. 385-394, 2015.

[25] K. P. Padiyar, HVDC Power Transmission Systems, New Academic Science, 2011.

[26] S. P. Azad , R. Iravani and J. E. Tate, "Dynamic Stability Enhancement of a DC-Segmented AC Power System Via HVDC Operating-Point Adjustment," *IEEE Transactions on Power Delivery*, vol. 30, no. 2, pp. 657-665, 2015.

[27] H. Wang and M. A. Redfern, "Enhancing AC networks with HVDC interconnections," in *Electricity Distribution (CICED), China International Conference on*, Nanjing, 2010.

[28] U. Åström, V. F. Lescale, D. Menzies and M. Weimin, "The Xiangjiaba-Shanghai 800 kV UHVDC project, status and special aspects," in *Power System Technology (POWERCON), International Conference on*, Hangzhou, 2010.

[29] "Inga-Kolwezi, One of the world's longest electric power transmissions is the 1,700 km link that transmits power from Inga Falls on the Congo River to the copper mining district of Katanga in the Democratic Republic of Congo (DRC).," ABB, 2014. [Online]. Available: http://new.abb.com/systems/hvdc/references/inga-kolwezi.

[30] "HVDC References," ABB, 2016. [Online]. Available: http://new.abb.com/systems/hvdc/references.

[31] M. Barnes and A. Beddard, "Voltage Source Converter HVDC Links – The State of the Art and Issues Going Forward," *Energy Procedia*, vol. 24, pp. 108-122, 2012.

[32] A. M. Vural, "Contribution of high voltage direct current transmission systems to inter-area oscillation damping: A review," *Renewable and Sustainable Energy Reviews*, vol. 57, p. 892–915, 2016.

[33] L. Liu and C. Liu, "VSCs-HVDC may improve the Electrical Grid Architecture in future world," *Renewable and Sustainable Energy Reviews*, vol. 62, p. 1162–1170, 2016.

[34] S. Henry, O. Despouys and G. Karady, "Influence of embedded HVDC transmission on system security and AC network performance," CIGRE, 2013.

[35] B. Eliasson, Damping of power oscillations in large power systems, Lund, Sweden : Dept. of Automatic Control, Lund Institute of Technology, 1990.

[36] B. Pal and B. Chaudhuri, Robust Control in Power Systems, Springer US, 2005.

[37] K. R. Padiyar, Analysis of subsynchronous resonance in power systems, Boston:

Kluwer Academic Publishers, 1999.

[38] N. Yang, Q. Liu and J. McCalley, "TCSC controller design for damping interarea oscillations," *IEEE Trans Power Sys*, vol. 13, no. 4, pp. 1304-1310, 1998.

[39] D. Laila, A. Messina and B. Pal, "A refined hilbert–huang transform with applications to interarea oscillation monitoring," *IEEE Trans Power Syst*, vol. 24, no. 2, pp. 610 - 620, 2009.

[40] A. Messina, Inter-area oscillations in power systems, US : Springer, 2009.

[41] J. Turunen, M. Larsson, P. Korba, J. Jyrinsalo and L. Haarla, "Experiences and future plans in monitoring the inter-area power oscillation damping," in *Proceeding of the 2008 IEEE Power and energy society general meeting-conversion and delivery of electrical energy in the 21st century*, 2008.

[42] J. He, C. Lu, X. Wu, P. Li and J. Wu, "Design and experiment of wide area HVDC supplementary damping controller considering time delay in China southern power grid," *IET Gener Transm Distrib,* vol. 3, no. 1, pp. 17-25, 2009.

[43] K. Rouzbehi, A. Miranian, J. I. Candela, A. Luna and P. Rodriguez, "A Generalized Voltage Droop Strategy for Control of Multiterminal DC Drids," *IEEE Transations on Industry Applications*, vol. 51, no. 1, pp. 607-618, 2015.

[44] T. M. Haileselassie and K. Uhlen, "Impact of DC line voltage drops on power flow of MTDC using droop control," *IEEE Transactions on Power Systems,* vol. 27, no. 3, pp. 1441-1449, 2012.

[45] Z. Wang, K. Li, J. Ren, L. Sun, J. Zhao, Y. Liang, W. Lee, Z. Ding and Y. Sun, "A Coordination Control Strategy of Voltage-Source-Converter-Based MTDC for Offshore Wind Farms," *IEEE Trans. Ind. Appl.,* vol. 51, no. 4, pp. 2743-2752, 2015.

[46] R. Pinto, P. Bauer, S. Rodrigues, E. Wiggelinkhuizen, J. Pierik and B. Ferreira, "A novel distributed direct-voltage control strategy for grid integration of offshore wind energy systems through MTDC network," *IEEE Trans. Ind. Electron.,* vol. 60, no. 6, pp. 2429-2411, 2013.

[47] N. Chaudhuri and B. Chaudhuri, "Adaptive droop control for Effective Power Sharing in Multi-Terminal DC (MTDC) Grids," *IEEE Transactions on Power Systems,* vol. 28, no. 1, pp. 21-29, 2013.

[48] N. Chaudhuri, B. Chaudhuri, R. Majumde and A. Yazdani, Multiterminal direct-current grids: Modeling, analysis, and control., John Wiley & Sons, 2014.

[49] F. Thams, R. Eriksson and M. Molinas, "Interaction of droop control structures and its inherent effect on the power transfer limits in multiterminal VSC-HVDC," *IEEE Trans. Power Del.*, vol. 32, no. 1, pp. 182 - 192, 2017.

[50] T. Magg, H. Mutschler, S. Nyberg, J. Wasborg, H. Thunehed and B. Sandberg, "Caprivi link HVDC interconnector: site selection, geophysical investigations, interference impacts and design of the earth electrodes," in *CIGRE 21 rue d'Artois F-75008*, Paris, 2010.

[51] T. Shimato, T. Hashimoto and M. Sampei, "The Kii Channel HVDC link in Japan," in *CIGRE 21 rue d.Artois F-75008*, Paris, 2002.

[52] H. Nakao, M. Hirose, T. Sakai, N. Kawamura, H. Miyata, M. Kadowaki, T. Oomori and A. Watanabe, "The 1,400-MW Kii-Channel HVDC System," *Hitachi Review,* vol. 50, no. 3, 2001.

[53] "Electricity sector in Japan," Wikipedia, 2012. [Online]. Available: https://en.wikipedia.org/wiki/Electricity_sector_in_Japan.

[54] T. Calverley, A. Gavrilovic, F. Last and C. Mott, "The Kingsnorth-Beddington-Willesden DC Link," in *CIGRÉ session, paper 43-04*, Paris, 1968.

[55] T. Rauhala, F. Fingrid Oyj, J. Jyrinsalo and H. Kuisti, "Enhancing the transmission capability using FACTS: The Finnish experience," in *AC and DC Power Transmission. ACDC. 9th IET International Conference on*, London, 2010.

[56] M. Xiao-ming, Z. Yao, G. Lin and W. Xiao-chen, "Coordinated control of interarea oscillation in the China Southern power grid," *IEEE Transactions on Power Systems*, vol. 21 , no. 2, pp. 845 - 852, 2006.

[57] H. Rao, "Architecture of Nan'ao multi-terminal VSC-HVDC system and its multi-functional control," *CSEE Journal of Power and Energy Systems,* vol. 1, no. 1, pp. 9-18, 2015.

[58] G. Tang, Z. He, H. Pang, X. Huang and X. p. Zhang, "Basic topology and key devices of the five-terminal dc grid," *CSEE Journal of Power and Energy Systems*, vol. 1, no. 2, pp. 22-35, 2015.

[59] H. Xianlai, D. Yunlong and L. Zhiguo, "Strategy of AC-isolated island detecting and control mode switching over in Zhoushan Project," in *13th IET International Conference on AC and DC Power Transmission*, Manchester, UK, 2017.

[60] D. Ernst, D. Ruiz-Vega, M. Pavella, P. M. Hirsch and D. Sobajic, "A unified approach to transient stability contingency filtering, ranking and assessment," *IEEE*

Transactions on Power Systems, vol. 16, no. 3, pp. 435 - 443, 2001.

[61] S. Li, T. A. Haskew and L. Xu, "Control of HVDC Light System Using Conventional and Direct Current Vector Control Approaches," *IEEE Transactions on Power Electronics* , vol. 25, no. 12, pp. 3106-3118, 2010.

[62] J. Yu, M. Xiao and G. Karady, "Dynamic performance of embedded HVDC with frequency control strategy," in *Power & Energy Society General Meeting, IEEE,* Denver, CO, 2015.

[63] B. Chaudhuri and B. Pal, "Robust damping of multiple swing modes employing global stabilizing signals with a TCSC," *IEEE Trans Power Syst,* vol. 19, p. 499 – 506, 2004.

[64] B. Chaudhuri, R. Majumder and B. Pal, "Wide-area measurement based stabilizing control of power system considering signal transmission delay," *IEEE Trans Power Syst,* vol. 19 , p. 1971–1979, 2004.

[65] D. Dotta, A. Silva and I. Decker, "Wide-area measurements-based two-level control design considering signal transmission delay," *IEEE Trans Power Syst,* vol. 24, p. 208 – 216, 2009.

[66] X. Mao, Y. Zhang, L. Guan, X. Wu and N. Zhang, "Improving power system dynamic performance using wide-area high-voltage direct current damping control," *IET Gener Transm Distrib,* vol. 2, pp. 245 - 251, 2008.

[67] G. Rogers, Power System Oscillations, Boston: Kluwer Academic, 2000.

[68] R. Preece, J. Milanovic, A. Almutairi and O. Marjanovic, "Damping of inter-area oscillations in mixed AC/DC networks using WAMS based supplementary controller," *IEEE Trans Power Syst,* vol. 28 , no. 2, p. 1160–1169, 2013.

[69] S. Kerahroudi, R. Rabbani, L. Fan, G. Taylor, A. M. and M. Bradley, "Power system stability enhancement of the future GB transmission system using HVDC link," in *Proceeding of the 49th International universities power engineering conference,* 2016.

[70] R. Preece, M. Almutairi, O. Marjanovic and V. Milanovic, "Damping of inter-area oscillations using WAMS based supplementary controller installed at VSC based HVDC line," *Proceeding of the IEEE Trondheim PowerTech,* p. 1–8, 2011.

[71] K. Poon and K. Lee, "Analysis of transient stability swings in large interconnected power systems by Fourier transformation," *IEEE Trans Power Syst,* vol. 3, no. 4, p.

1573–1581, 1988.

[72] J. F. Hauer, "Application of prony analysis to the determination of modal content and equivalent models for measured power system response," *IEEE Trans Power Syst,* vol. 6, no. 3, p. 1062–1068, 1991.

[73] H. Peng and C. Nair, "Comparative assessment of Kalman Filter and Prony Methods for power system oscillation monitoring," in *IEEE Power & Energy Society General Meeting*, Calgary, AB, 2009.

[74] S. Ray and G. Venayagamoorthy, "Real-time implementation of a measurement-based adaptive wide-area control system considering communication delays," *IET Gener Transm Distrib,* vol. 2, pp. 62-70, 2008.

[75] J. Xiao, X. Xie, Y. Han and J. Wu, "Dynamic tracking of low frequency oscillations with improved prony method in wide-area measurement system.," in *Proceeding of the 2004 IEEE Power engineering society general meeting*, Denver, CO, 2004.

[76] X. Xie, J. Xiao, C. Lu and Y. Han, "Wide-area stability control for damping interarea oscillations of interconnected power systems," *IEE Gener Transm Distrib*, vol. 153, no. 5, pp. 507-514, 2006.

[77] J. Ma, T. Wang, Z. Wang and J. Thorp, "Adaptive damping control of inter-area oscillations based on federated kalman filter using wide area signals," *IEEE Trans Power Syst,* vol. 28, no. 2, pp. 1627-1635, 2013.

[78] C. Lu, X. Wu, J. Wu, P. Li, Y. Han and L. Li, "Implementations and experiences of wide-area HVDC damping control in China southern power grid.," in *Proceeding of the IEEE Power and energy society general meeting*, San Diego, CA, 2012.

[79] D. Trudnowski, J.Johnson and J. Hauer, "Making prony analysis more accurate using multiple signals," *IEEE Trans Power Syst,* vol. 14, no. 1, pp. 226-231, 1999.

[80] M. Bakhshi, R. Noroozian and G. Gharehpetian, "Anti-islanding scheme for synchronous DG units based on tufts–kumaresan signal estimation method," *IEEE Trans Power Deliver,* vol. 28, no. 4, pp. 2185-2193, 2013.

[81] L. M. and L. D. S., "Monitoring of inter-area oscillations under ambient conditions using subspace identification.," in *Proceeding of the IEEE Power and energy society general meeting*, Calgary, AB, 2009.

[82] R. Eriksson and L. Soder, "Wide-Area Measurement System-Based Subspace Identification for Obtaining Linear Models to Centrally Coordinate Controllable

Devices," *IEEE Transactions on Power Delivery,* vol. 26, no. 2, pp. 988 - 997, 2011.

[83] P. Zhang, D. Y. Yang, K. Chan and G. W. Cai, "Adaptive widearea damping control scheme with stochastic subspace identification and signal time delay compensation," *IET Gener Transm Distrib,* vol. 6, no. 9, pp. 844-852, 2012.

[84] Y. Pipelzadeh, B. Chaudhuri and T. C. Green, "Control Coordination Within a VSC HVDC Link for Power Oscillation Damping: A Robust Decentralized Approach Using Homotopy," *IEEE Transactions on Control Systems Technology,* vol. 21, no. 4, pp. 1270 - 1279, July 2013 .

[85] W. Hu, G. Liu and D. Rees, "Networked predictive control over the Internet using round-trip delay measurement.," *IEEE Transactions on Instrumentation and Measurement ,* vol. 57, no. 10, pp. 2231 -2241, Oct. 2008.

APPENDIX A

SYSTEM POWER FLOW DATA

```
0    100.0
                                        100.0
       1  'BD       AR1'    230.00  2          0.000          0.000       1        1  1.03000
43.0363
       2  'BD       AR1'    230.00  2          0.000          0.000       1        1  1.01000
32.2011
       3  'BD       AR2'    230.00  3          0.000          0.000       2        2  1.03000
0.0000
       4  'BD       AR2'    230.00  2          0.000          0.000       2        2  1.01000      -
9.7774
       5 'B         L'    230.00 1          0.000       223.500     1       1 0.98598       23.2790
       6 'B         L'    230.00 1          0.000       258.000     2       2 0.98660      -17.9830
 0
       5  BL  1      1        1     1241.000       100.000          0.000          0.000          0.000
0.000
       6  BL  1      2        2     1699.000       100.000          0.000          0.000          0.000
0.000
 0
      1 1     790.00       77.59      500.00    -150.00 1.03000         0    100.00
      2 1     790.00      277.09      500.00    -150.00 1.01000         0    100.00
      3 1     713.80       71.46      500.00    -150.00 1.03000         0    100.00
      4 1     740.00      243.37      500.00    -150.00 1.01000         0    100.00
 0
      1           2 1       0.00250      0.02500      0.00000          0.00          0.00          0.00
0.00000       0.00      0.00000      0.00000      0.00000      0.00000 1
      2           5 1       0.00100      0.01000      0.00000          0.00          0.00          0.00
0.00000       0.00      0.00000      0.00000      0.00000      0.00000 1
      5           6 1       0.02200      0.22000      0.00000          0.00          0.00          0.00
0.00000       0.00      0.00000      0.00000      0.00000      0.00000 1
      3           4 1       0.00250      0.02500      0.00000          0.00          0.00          0.00
0.00000       0.00      0.00000      0.00000      0.00000      0.00000 1
      4           6 1       0.00100      0.01000      0.00000          0.00          0.00          0.00
0.00000       0.00      0.00000      0.00000      0.00000      0.00000 1
 0
    1        1      600.000          3.000    'AREA1     '
    2        3     -600.000          3.000    'AREA2     '
```

APPENDIX B

SYSTEM DYNAMIC DATA

```
DESC
DGEN
      1       1    100    100
      0       0     30       0       0       0       0       0       0       0       0       0
    0.00250       1.80000       1.70000       0.00000         .30000         .30000         0.0000
0.0000
    8.00000       0.40000       .00000       .00000
    6.50000       5.00000       .00000         900.         1.00       .00000
      0       1       1       1
  200.00000           .01000         1.00000       10.00000           .00000           0.0000
0.00000       .00000
    5.00000           -5.0000             .00000             .00000           0.00000
0.0000       .00000       .00000
      .01000       .00000       .00000       .00000       .00000       .00000       .00000       .0
0000
      .00000       .00000           0.0           0.0
      2       1    100    100
      0       0     30       0       0       0       0       0       0       0       0       0
    0.00250       1.80000       1.70000       0.00000         .30000         .30000         0.0000
0.0000
    8.00000       0.40000       .00000       .00000
    6.50000       5.00000       .00000         900.         1.00       .00000
      0       1       1       1
  200.00000           .01000         1.00000       10.00000           .00000           0.0000
0.00000       .00000
    5.00000           -5.0000             .00000             .00000           0.00000
0.0000       .00000       .00000
      .01000       .00000       .00000       .00000       .00000       .00000       .00000       .0
0000
      .00000       .00000           0.0           0.0
      3       1    100    100
      0       0     30       0       0       0       0       0       0       0       0       0
    0.00250       1.80000       1.70000       0.00000         .30000         .30000         0.0000
0.0000
    8.00000       0.40000       .00000       .00000
    6.50000       5.00000       .00000         900.         1.00       .00000
      0       1       1       1
  200.00000           .01000         1.00000       10.00000           .00000           0.0000
0.00000       .00000
    5.00000           -5.0000             .00000             .00000           0.00000
0.0000       .00000       .00000
      .01000       .00000       .00000       .00000       .00000       .00000       .00000       .0
0000
      .00000       .00000           0.0           0.0
      4       1    100    100
```

```
      0       0     30       0       0       0       0       0       0       0       0       0
    0.00250      1.80000      1.70000      0.00000       .30000       .30000       0.0000
0.0000
    8.00000     0.40000      .00000      .00000
    6.50000     5.00000      .00000        900.        1.00      .00000
     0       1       1       1
 200.00000           .01000          1.00000       10.00000           .00000           0.0000
0.00000       .00000
    5.00000           -5.0000               .00000               .00000           0.00000
0.0000       .00000       .00000
      .01000       .00000       .00000       .00000       .00000       .00000       .00000       .0
0000
      .00000       .00000           0.0           0.0
EDATA
 NLBS
      5       0       0       0       0       0       0       0
      6       0       0       0       0       0       0       0
EDATA
   END
```